The Abundances of Ultraheavy Elements in the Cosmic Radiation

Thesis by
Brian John Newport

In Partial Fulfillment of the Requirements
for the Degree of
Doctor of Philosophy

California Institute of Technology
Pasadena, California

1986

(Submitted May 21, 1986)

ACKNOWLEDGEMENTS

This thesis builds directly on six years of work by the data analysis team for the Heavy Nuclei Experiment. The success of this experiment in turn rests on a decade of design and development involving many others.

First, I would like to thank my advisor, Edward Stone. Ed's attention to detail, his persistence, and his command of the subject provide a formidable model for a young scientist. It has been a privilege to work with him.

Tom Garrard designed the preliminary data analysis programs and managed the production of the data library. Tom's assistance with problems both scientific and mundane is much appreciated, as is his easygoing manner.

Mary Kertzman cheerfully provided the propagation calculations used in Chapters 3 and 4, often at short notice. Mary also generously let me use her preliminary fragmentation cross section results.

I will miss the intellectual energy brought by the other HNE collaborators, past and present. At Washington University in St. Louis are Marty Israel, Bob Binns, Joe Klarmann, Dave Grossman, Mike Jones, and Marty Olevitch; at the University of Minnesota are Jake Waddington, Bob Fickle, Dale Fixsen, and Nancy Brewster; and at Caltech, my former officemate Keith Krombel. Other useful advice and assistance was given by Bill Althouse, Alan Cummings, Dick Mewaldt, and Tom Prince, all of Caltech.

Physics today relies heavily on computers, and the work described in this thesis is no exception. Nancy Collins helped me locate and resolve many obscure problems in my programs, while Brownlee Gauld wrote many of the preliminary data analysis programs, and also the data acquisition software used in the Bevalac calibrations. Other useful software and programming assistance was provided by Shelley Mjolsness and Ruth Heide, and many of my tape jobs were run by Randy Burrell and Len Thomas.

Always cheerful and eager to help, Deeby Kadrie and Sandy Lester provided secretarial assistance from time to time.

Life in graduate school is more pleasant if one's officemates are friendly and helpful. Worthy of note here are Eric Aslakson, Eric Christian, Mark Finger, Chris Starr, and Tim Zukowski. Similarly, housemates make a big difference: Ted Russell, Mark Cohen, Miles Gehm, and Ranajit Sahu. What a great bunch!

Since coming to the United States in 1980, I have been influenced by many people and made many friends. Those I wish to mention here are Ravi Chandar, Jim and Cora Findley, Matt Johnson, Prakash Kasiraj, Beth Kelnhofer, Lisa Kircher, Karen Knotts, Robi Mulford, Karen Patterson, Margaret Rankin, Dick Renneker, Jerri Russell, Roy Smith, Serena Soltes, and Larry Sverdrup. With some of you I've climbed mountains and travelled, with others I've eaten and drank, danced, or just talked. Thank you all.

During my stay at Caltech, I have received Special Tuition Awards from the Institute, and have been supported by Graduate Research Assistantships, as well as a Graduate Teaching Assistantship in my first year. Data analysis for the Heavy Nuclei Experiment is supported at Caltech by NASA grants NAG8-502 and NGR05-002-160, and previously by NASA contract NAS8-27978. NASA is funded by the United States taxpayers, who have collectively chosen to support space science, and who have indirectly provided the funds which enabled me to obtain a graduate degree in this country. I am very grateful.

Brian Newport
Pasadena, California
May 1986

ABSTRACT

Analysis of the data from the Heavy Nuclei Experiment on the HEAO-3 spacecraft has yielded the cosmic ray abundances of odd-even element pairs with atomic number, Z, in the range $33 \leq Z \leq 60$, and the abundances of broad element groups in the range $62 \leq Z \leq 83$, relative to iron. These data show that the cosmic ray source composition in this charge range is quite similar to that of the solar system, provided an allowance is made for a source fractionation based on first ionization potential. The observations are inconsistent with a source composition which is dominated by either r-process or s-process material, whether or not an allowance is made for first ionization potential. Although the observations do not exclude a source containing the same mixture of r- and s-process material as in the solar system, the data are best fit by a source having an r- to s-process ratio of $1.22^{+0.25}_{-0.21}$, relative to the solar system. The abundances of secondary elements are consistent with the leaky box model of galactic propagation, implying a pathlength distribution similar to that which explains the abundances of nuclei with $Z<29$.

The energy spectra of the even elements in the range $38 \leq Z \leq 60$ are found to have a deficiency of particles in the range ~1.5 to 3 GeV/amu, compared to iron. This deficiency may result from ionization energy loss in the interstellar medium, and is not predicted by propagation models which ignore such losses. In addition, the energy spectra of secondary elements are found to be different to those of the primary elements. Such effects are consistent with observations of lighter nuclei, and are in qualitative agreement with galactic propagation models using a rigidity dependent escape length. The energy spectra of secondaries arising from the platinum group are found to be much steeper than those of lower Z. This effect may result from energy dependent fragmentation cross sections.

TABLE OF CONTENTS

Chapter 1

Introduction

1.1. Cosmic Rays

By measuring the discharge rates of electroscopes carried aloft in balloons, Hess (1912) first demonstrated the presence of an extraterrestrial source of ionizing radiation. This radiation is now known to consist almost entirely of charged particles whose sources lie beyond the solar system, and hence the name: cosmic rays. These particles have been observed with kinetic energies from $\sim 10^7$eV to $\sim 10^{20}$ eV, and are comprised of 98% protons and heavier atomic nuclei, with the remainder being electrons and positrons. The nuclear component is stripped of atomic electrons at all but the lowest energies, and at 1 GeV/amu consists of roughly 87% hydrogen, 12% helium, and 1% heavier nuclei (Simpson, 1983).

Cosmic rays appear to be a pervasive feature of the Galaxy, and in the interstellar medium have an energy density similar to that of starlight ($\sim$1 eV cm^{-3}). From measurements of the abundance of the radioactive isotope ^{10}Be, their mean lifetime is inferred to be $\sim$10 million years (Wiedenbeck and Greiner, 1980).

Cosmic rays provide one of the few direct samples of material from beyond the solar system, and thus their composition provides an important clue to the chemical composition of the Galaxy as a whole. This thesis reports a new measurement of the abundances of cosmic ray elements with atomic number, Z, greater than 33. For historical reasons, nuclei heavier than helium are classified in groups: nuclei with $Z > 30$ are referred to as "ultraheavy", while those with $21 \leq Z \leq 30$ are "very heavy", those with $10 \leq Z \leq 20$ are "heavy", those with $6 \leq Z \leq 9$ are "medium", and those with $3 \leq Z \leq 5$ are "light". Ultraheavy cosmic rays were first observed in a study of particle tracks in meteorites (Fleischer et al., 1967).

1.2. A Model of Cosmic Ray Origin and Propagation

The results of this thesis will be discussed in the context of a standard model of cosmic ray origin, acceleration, and propagation. This model represents an explanation of the observed abundances and energy spectra of the nuclei up to and including iron, and is in reasonable agreement with those data. It has been developed over a considerable period of time by a number of investigators, and has gradually evolved as new data became available.

The first step in this model is nucleosynthesis, in which nuclear reactions within astrophysical objects synthesize heavy nuclei from precursor material. Later, the synthesized material is injected into an astrophysical particle accelerator. Injection may occur by the expulsion of material from objects such as novae or flare stars, or it may occur directly from the interstellar medium. It may also involve the ionization of neutral atoms, which in turn may result in a fractionation of the less easily ionized elements.

Following acceleration to relativistic velocities, the particles diffuse in the galactic magnetic field, occasionally colliding with atoms in the interstellar medium. These high energy interactions result in the fragmentation of the original nuclei (primaries) to form lighter nuclei (secondaries), and thus change their relative abundances. The combination of diffusion and fragmentation is referred to as galactic propagation.

Following propagation in the interstellar medium, and their passage into the heliosphere, the cosmic rays diffuse in the interplanetary medium. The diffusion of particles with rigidities $\lesssim 4$ GV into the inner solar system is strongly dependent on the solar wind speed and the density of magnetic irregularities in the interplanetary medium, which in turn depend on the degree of recent solar activity; hence the term "solar modulation". At higher rigidities, the flux of cosmic rays at earth is unaffected by the interplanetary medium.

The final part of the journey involves propagation in the Earth's magnetosphere and through any residual atmosphere above the detector. The geomagnetic field shields large areas of the upper atmosphere from lower

energy particles (e.g. Fermi, 1940). Particles with rigidities below a particular cutoff value are unable to completely penetrate the magnetosphere and are thus not observed. This geomagnetic cutoff depends on the magnetic latitude of the detector, the arrival direction of the particle in question, and the height of the detector above the surface, and has a maximum value of ~60 GV near the equator, for positive particles arriving from the east. The removal of low energy particles by the geomagnetic cutoff greatly modifies the observed rigidity spectrum.

Alternatives to this standard model do exist. For example, some workers believe that there is evidence for reacceleration of the cosmic rays after they have been propagating for some time. This idea naturally extends to continuous acceleration, in which the acceleration of particles occurs everywhere in the interstellar medium. At present the experimental data are insufficient to distinguish between the standard model and these alternatives.

Those parts of the standard model leading up to a particle's arrival in the outer heliosphere (i.e., nucleosynthesis, injection, acceleration, and galactic propagation) will now be described in more detail.

1.2.1. **Nucleosynthesis of Ultraheavy Elements**

The most popular theories of cosmology predict that the early universe contained almost no nuclei heavier than helium. However, the modern universe contains substantial quantities of heavy elements: on earth and other planets, in the sun, and in other stars and galaxies. The nucleosynthesis required for this chemical evolution is believed to have occurred within stars, and the theory was systematized in the historic work of Burbidge, Burbidge, Fowler and Hoyle (1957). The understanding of the processes responsible for nucleosynthesis is a major goal of cosmic ray studies.

The fusion of light nuclei to make heavier ones is a generally exothermic process up to ^{56}Fe, provided that the reactants have sufficient kinetic energy to overcome the Coulomb barrier. Thus a sufficiently massive star will proceed through the stages of hydrogen, helium, carbon, neon, oxygen, and silicon

burning before forming a core composed mostly of ^{56}Fe, then collapsing and exploding as a Type II supernova (e.g. Clayton, 1968). Less massive stars are unable to develop the extreme temperatures needed to burn the heavier nuclei and do not reach the supernova phase. In a supernova, further nucleosynthesis occurs as the shock wave moves out through the outer layers of the star, and the local interstellar medium is subsequently enriched in the heavy elements contained in the ejected material. Later, new star formation makes this material available for further processing and the chemical composition of the galaxy as a whole evolves towards the heavier elements.

The existence of elements much heavier than iron in the solar system requires the operation of additional nucleosynthesis processes. Burbidge et al. (1957) proposed two extreme neutron capture processes which are able to synthesize most heavy nuclei observed in the solar system. In the "s", or slow neutron capture process, a seed nucleus is allowed to capture neutrons until an unstable species is formed. The time between successive captures is sufficiently large that this nucleus undergoes β decay, raising its charge, Z, before a further neutron capture occurs. The time scale for neutron capture is set by the β decay lifetimes which are mostly less than 100 years. The nuclei made in the s-process lie on a path in the valley of stability on a (Z,N) diagram.

The relative abundances of neighboring s-process nuclei are controlled by their neutron capture cross sections. In the case of an exponential neutron flux distribution,

$$N_A\sigma_A = N_{A-1}\sigma_{A-1} + KN_{A-1}, \qquad (1.1)$$

where K is chosen to fit the observed abundances of pure s-process nuclei in the solar system, N_A is the abundance of the nucleus of mass number A, and σ_A is the neutron capture cross section of that nucleus. Although refinements are needed to precisely explain the solar system abundances, this simple model fits the data in a qualitative way. From (1.1), we see that the nuclei with the smallest capture cross sections will be produced in the greatest abundance by the s-process. These are the "magic" nuclei, for which either the

proton number, Z, or the neutron number, N, have the values 50, 82 or 126. The heaviest nucleus that can be synthesized by the s-process is ^{209}Bi, since the next nucleus on the s-process path, ^{210}Bi, decays by alpha emission with a 5 day half life, and thus breaks the chain.

Not all nuclei observed in the solar system can be synthesized by the s-process, and in particular none of the actinides can be made in this way. At the oppsite extreme is the alternative rapid, or r-process. In this case the seed nuclei are exposed to such a large neutron flux that there is insufficient time for decay back to the valley of β-stability. A given nucleus captures neutrons without decaying until equilibrium is reached between the (n,γ) rate and the inverse (γ,n) rate, at the neutron drip line. Eventually a β decay occurs, increasing Z. During the neutron exposure, the nucleosynthesis path lies far from the valley of stability, and the nuclei decay back towards the valley when the neutron flux falls. It is now recognized that the r-process is an extreme case of a more general n-process, in which the neutron flux is insufficient to reach the (γ,n) equilibrium point, while still well beyond the valley of stability. This relaxes the constraints on the astrophysical site somewhat.

These neutron capture processes require a neutron source. In the s-process, a likely candidate is $^{22}Ne(\alpha,n)^{25}Mg$, among others (Truran and Iben, 1977), and spectroscopic observations have shown that s-process products exist in the outer regions of red giant stars. The site of the r-process is less certain but the extreme conditions necessary require a cataclysmic event, possibly a supernova or black hole-neutron star collision, for example (Schramm 1982 and references therein).

At present it is impossible to calculate the abundances produced by the r-process with precision because the capture cross sections and lifetimes of nuclei with such large neutron excesses have not been measured. Instead, abundances of r-process nuclei are usually estimated by subtracting the results of an s-process calculation from a set of measured abundances, such as the measured composition of the solar system, and assuming that the difference represents the r-process contribution. Figure 1.1 plots the results

of such a decomposition, performed by Fixsen and given in the appendix of Binns et al. (1985). Of particular note are the abundance peaks in the Z = 50-58 region and Z = 76-82 region: the elements $_{56}$Ba and $_{82}$Pb are mainly synthesized in the s-process, while $_{52}$Te, $_{54}$Xe and $_{76}$Os–$_{78}$Pt are mainly synthesized in the r-process. A few rare nuclei can only be synthesized by proton capture and have been excluded from the abundances shown.

It is possible that the particular sets of r and s-process abundances derived for the solar system also describe the results of galactic nucleosynthesis in general, and thus represent a universal set of these abundances. Measurements of the abundances of heavy and ultraheavy elements in the cosmic rays have so far indicated a source composition which is broadly similar to that of the solar system, but with some detailed differences which are not well understood (Binns et al., 1984). A goal of the work described in this thesis is to improve the measurements of the cosmic ray abundances of as many elements as possible so that the nature of galactic nucleosynthesis may be better understood.

1.2.2. Injection

There is considerable evidence that elements with high first ionization potential (FIP) are suppressed in the cosmic rays relative to those with low first ionization potential. This FIP fractionation may be caused by an injection mechanism which requires charged particles rather than neutral atoms. Such a mechanism has been found to operate in the solar corona, where a step function FIP dependence has been found necessary to explain the observed abundances of solar flare particles. In that case the dependence may result from the outward convection ofionized atoms, while neutral atoms fall back to the surface and are therefore depleted in the solar corona, where acceleration takes place. The solar data are well fit by a step near 10.2 eV, the Lyman-α energy (e.g. Breneman and Stone, 1985). Many workers also prefer a step function FIP fractionation for galactic cosmic rays, but with the step at a lower energy. An example of this is the sloping step of Letaw et al. (1984):

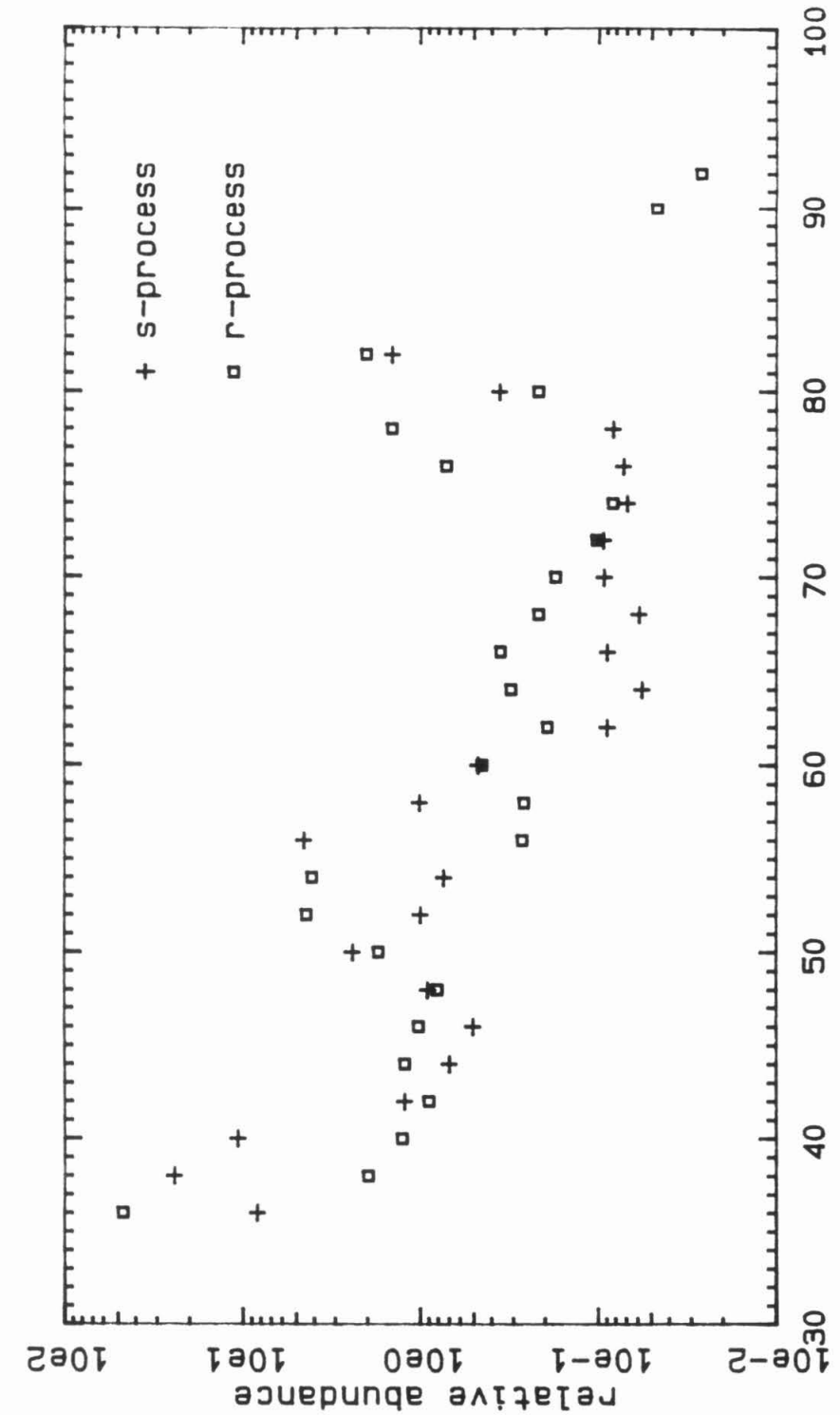

Figure 1.1 The r- and s-process contributions to the solar system even element abundances, normalized so that the abundance of Fe is 1.0×10^6. This decomposition was derived by Fixsen, and given in the appendix of Binns et al., (1985).

$$f(FIP) = \begin{cases} 1.26 & FIP \leq 7.0 \text{ eV} \\ 8.37 \exp(-0.27 \times FIP) & 7.0 < FIP \leq 13.6 \text{ eV} \\ 0.21 & FIP > 13.6 \text{eV} \end{cases} \quad (1.2)$$

1.2.3. A Digression: Energy vs Rigidity

The terms "energy" and "rigidity" will be used somewhat interchangeably in this thesis. The term energy as used here means kinetic energy per atomic mass unit (amu), which is almost the same as kinetic energy per nucleon. Any two particles with the same kinetic energy per amu have identical velocities. The units of energy will generally be MeV/amu or GeV/amu.

Rigidity means magnetic rigidity, and describes the difficulty of deflecting a particle with a magnetic field: two particles with the same rigidities will have the same gyroradii in a given perpendicular magnetic field. Rigidity is defined as $R = pc/Ze$, where p is the particle's momentum, c is the velocity of light, Z the charge state, and e the elementary charge. The measurement of p in GeV/c leads to a value of R in GV.

Kinetic energy per amu is a natural variable in processes which are functions of velocity, such as ionization energy loss, nuclear fragmentation, and Čerenkov radiation. Rigidity is a natural variable in processes governed by magnetic fields, such as the diffusion of particles in the interstellar medium and the acceleration of particles by shock waves in a magnetized plasma.

The conversion between rigidity and kinetic energy per amu, E, is given by

$$E = \left[\left(\frac{Z}{A} eR \right)^2 + m^2c^4 \right]^{1/2} - mc^2 \quad (1.3)$$

where A is the atomic mass of the particle and m is one amu. Z/A varies from 0.46 at ^{56}Fe to 0.39 at ^{208}Pb, implying that a rigidity dependent process will also be charge dependent when operating on ultraheavy nuclei.

1.2.4. Acceleration

In the standard model of cosmic ray origin the acceleration mechanism is assumed to provide particles with the energy (or rigidity) spectrum necessary to explain the observations. The acceleration sites are not specified. In the reacceleration models the accelerators must have a large surface area, in order for sufficient particles to be reaccelerated after diffusion. Obviously an important goal of cosmic ray studies is to determine the nature of the cosmic ray acceleration mechanism, as well as identify the sites where it occurs.

The idea that magnetohydrodynamic shock waves can accelerate charged particles is now well established, and shock acceleration appears to be a common phenomenon in astrophysics. In the solar system, particle acceleration occurs at the bow shocks associated with planetary magnetospheres, in solar flares, and in corotating interaction regions in the interplanetary medium. These accelerators provide modest kinetic energies: from a few keV in planetary magnetospheres, to 1 GeV or more in the largest solar flares. On a much larger scale, shock waves from supernovae and other violent processes are prevalent throughout the galaxy. Particle acceleration by shocks may account for the bulk of the galactic cosmic ray energy density, and produce the observed energy spectrum at all but the highest observed energies. In the theory of shock acceleration a strong shock accelerates particles with an R^{-2} spectrum, where R is the rigidity, while weak shocks result in softer spectra, with a larger spectral index. The spectra of the accelerated particles are later modified by galactic propagation.

1.2.5. Galactic Propagation

The simplest diffusion model which adequately describes the observations of light and medium nuclei is the leaky box model (Cowsik et al., 1967). This is a one dimensional model in which the particles are assumed to be generated at a constant rate everywhere in the galaxy and then to diffuse within the galactic volume. From time to time a given particle encounters the galactic boundary, and is assumed to have a finite chance of escaping at each

encounter. The mean column density of interstellar material traversed before escape is referred to as the escape length, λ_e. In the steady state, the distribution of material encountered by the particles is given by an exponential:

$$f(x) = \frac{1}{\lambda_e}\exp(-x/\lambda_e) \tag{1.4}$$

where x is the pathlength traversed between the cosmic ray source and the detector.

With this pathlength distribution, the probability per unit pathlength of a primary nucleus traversing a distance x without escape or interaction is

$$P(x) = \left[\frac{1}{\lambda_e}+\frac{1}{\lambda_i}\right]\exp\left[-x\left(\frac{1}{\lambda_e}+\frac{1}{\lambda_i}\right)\right] \tag{1.5}$$

where λ_i is the fragmentation mean free path. Some elements, such as Li, Be, and B are thought to be absent in the cosmic ray source. The ratios of the abundances at earth of these purely secondary nuclei to their primaries (mostly C, N, and O) give the value of λ_e, which is found to be in the neighborhood of 7 gcm^{-2} of pure hydrogen at energies of order 1 GeV/amu.

The secondary to primary ratios are found to decrease at higher energies, implying that the escape length is rigidity dependent. Such a decrease is to be expected, since both the diffusion and confinement of cosmic rays in the galaxy are controlled by magnetic fields. The energy spectra of all species are steepened by the rigidity dependent pathlength, compared to the case of rigidity independent confinement. Further energy dependences of primary to secondary ratios may be introduced by energy dependent cross sections, although these are expected to approach a constant value above 3 GeV/amu. The relevant cross sections have mostly not been measured, but must be inferred from semiempirical models.

Below about 2 GeV/amu, the flux of particles at a given energy is significantly reduced by ionization energy loss to the interstellar medium. Since the energy loss per amu is proportional to Z^2/A to first order, the energy spectra of the heavier nuclei are more affected by this process. As an

example, the energy loss of a 2 GeV/amu Fe nucleus in 7 gcm^{-2} of molecular hydrogen is about 400 MeV/amu, while a 2 GeV/amu Pb nucleus loses about 1 GeV/amu in the same amount of material. At higher energies the effect of energy loss is less severe and it is often ignored when comparing propagation calculations with high energy data.

Measurements of secondary to primary ratios below iron indicate that the pathlength distribution is truncated, i.e., that the shortest pathlengths are missing from the pathlength distribution. This is to be expected if the majority of the cosmic ray sources lie in dense regions such as molecular clouds, where all nuclei must traverse a substantial amount of material before escaping into the interstellar medium. However, there is so far no evidence that truncation is necessary to explain the ultraheavy secondary to primary ratios (Klarmann et al., 1983, 1985).

Chapter 2

The Heavy Nuclei Experiment

2.1. The Instrument

The Heavy Nuclei Experiment was a large cosmic ray detector on HEAO-3, the third High Energy Astronomy Observatory spacecraft. Since this experiment has been described by Binns et al. (1981), and by Krombel (1983), the discussion here will concentrate on those features not previously discussed.

Charge-sensitive detectors generally have a response of the form

$$S = kbZ^2f(\beta), \tag{2.1}$$

to first order, where S is the detector output, k is a constant, b is the particle's pathlength in the detector, Z is the particle charge and β its velocity divided by the speed of light. The pathlength dependence is easily removed by using hodoscopes to determine the particle trajectory, and in principle we can eliminate the velocity dependence by using two detectors having different $f(\beta)$, allowing us to solve for Z if k is known. The Heavy Nuclei Experiment uses the the dE/dx-Čerenkov technique where one set of detectors measures ionization energy loss (more correctly energy deposit) and the other observes the Čerenkov radiation in a suitable medium. A particle traversing the detector may have a significant chance of undergoing a charge-changing nuclear interaction, making it desirable to incorporate some redundancy in the charge measurement. In the Heavy Nuclei Experiment a plastic Čerenkov detector was preceded and followed by gas-filled ionization modules, together with four layers of multi-wire ionization hodoscopes, as shown in Figure 2.1.

The rectangular shape of the instrument was chosen to maximize the geometry factor within the constraints imposed by the spacecraft geometry. This in turn imposed a constraint on the ion chamber windows: to support ~1 atmosphere pressure over a large area while using the smallest possible thickness of material, the windows were made from aluminum honeycomb with

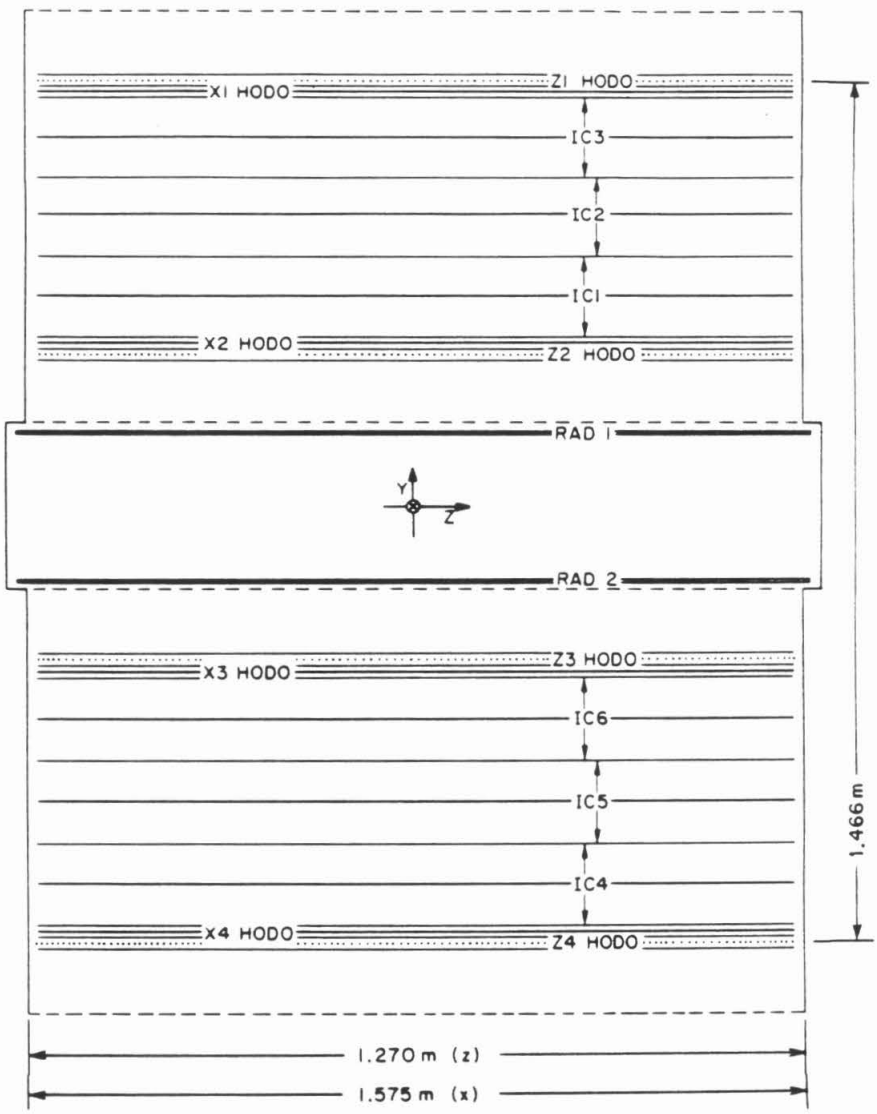

Figure 2.1 A schematic view of the Heavy Nuclei Experiment, showing the four hodoscopes, six ion chambers, two Čerenkov radiators, and the four honeycomb windows.

aluminum face sheets glued to each side. The honeycomb cells measured 0.125" from flat to flat between the inside faces, and were 3.42" deep, with a wall thickness of 0.001325", with double walls in one direction. Particles arriving at normal incidence and passing through the center of a honeycomb cell traversed about 0.6 g cm^{-2} of material in each of the four ion chamber windows. Particles arriving at some other angle, ϑ, traversed an amount of material t secϑ, where t is generally between 0.6 and 1.6 g cm^{-2} and depends on the precise trajectory. This feature complicated the analysis of the calibration described in Section 2.3.

Ion chambers used in balloon experiments generally use a thin material such as aluminized mylar for the electrodes to minimize the amount of material. However, concerns about the reliability of the electrical connections led instead to the use of screenwire. The material used was a woven sheet made from 0.010" diameter aluminum wire with a 0.0625" center to center spacing. The use of screenwire electrodes had important consequences for the ion chamber resolution, which will be discussed further in Section 2.2 .

The energy loss of a charged particle per unit pathlength is approximated by the Bethe formula (e.g. Ahlen, 1980):

$$\frac{dE}{dx} = k_I \frac{Z^2}{\beta^2}\left[\ln\frac{2mc^2\beta^2\gamma^2}{I_{adj}} - \beta^2 - S\right] \qquad (2.2)$$

where m is the electron mass, c is the velocity of light, I_{adj} is a logarithmic mean ionization potential of the medium β is the particle velocity divided by the speed of light, $\gamma = (1-\beta^2)^{-1/2}$ and S corrects for atomic shell effects when the particle velocity is comparable to the atomic electron velocity (Barkas and Berger, 1964). (2.2) has the same form as (2.1) and is strictly proportional to Z^2. If we consider the energy lost by the incident particle in a thin slice of the detector, roughly half occurs in "close" collisions, producing energetic secondary electrons ("knockons"), which can then diffuse out of the slice. The cross-section for the scattering of a free electron by a massive spinless point nucleus of charge Z is given in the first Born approximation by

$$\left.\frac{d\sigma}{dT}\right|_{FB} = \frac{2\pi e^4}{mc^2}\frac{Z^2}{\beta^2}\frac{1}{T^2}\left[1 - \beta^2\frac{T}{T_{max}}\right] \quad cm^2\ MeV^{-1} \tag{2.3}$$

where T is the knockon energy and the kinematic maximum energy transfer is $T_{max} = 2mc^2\beta^2\gamma^2$ if the nucleus mass $M \gg m$. For sufficiently low primary energies the detector is thick compared to the maximum knockon range and the outward diffusion from our thin slice is balanced by inward diffusion from other points on the trajectory, resulting in a state of "equilibrium", where local energy deposit is equal to local energy loss. At higher primary energies the detector thickness becomes less than the maximum knockon range, causing the total energy deposit (and the resulting ionization) to be less than the energy loss. In the Heavy Nuclei Experiment this nonequilibrium effect becomes important for primary energies $\gtrsim 1$ GeV/amu and will be discussed later.

In the theory of ion chambers the charge collected at the electrodes is given by

$$I = \frac{e}{w}\int_0^b \left.\frac{dE}{dx}(x)\right|_{deposit}\left[1 - \frac{V(x)}{V_0}\right]dx \tag{2.4}$$

where x is the distance along the trajectory, V(x) is the electric potential, V_0 is the total potential between the electrodes, e is the electron charge, and w is the mean energy deposit required to make an electron-ion pair. For plane parallel electrodes and a constant rate of energy deposit (2.4) simplifies to

$$I = \frac{eb}{2w}\left.\frac{dE}{dx}\right|_{deposit} \tag{2.5}$$

The measured value of w for protons, alpha particles, and electrons varies, but is ~26 eV/ion pair in pure argon, and ~29 eV/ion pair in pure methane (Sharpe, 1964). The Heavy Nuclei Experiment used P-10 gas, a mixture of 90% argon and 10% methane, with ~0.5% helium added for leak detection. For heavy particles at very low energies the value of w rises because the particle loses energy to Coulomb scattering of the atomic nuclei, in addition to the atomic excitation processes which lead to ionization, however at the energies

of interest here, w is expected to be almost constant (Ahlen, 1980).

The Čerenkov light produced by a charged particle is given to first order by

$$L = k_C Z^2 \left(1 - \frac{1}{\beta^2 n^2} \right) \tag{2.6}$$

for $\beta > 1/n$, where n is the effective refractive index of the medium. In our case the medium is Pilot 425, which is plexiglass with a waveshifter incorporated to optimize the photomultiplier tube response, and a quenching material to minimize scintillation of this waveshifter. The total thickness of the Čerenkov radiators is 1.165 gcm^{-2}.

Figure 2.2 shows the relationship of the ionization and Čerenkov signals for the even charge elements near iron, using a model developed by Krombel (1980, 1981), with parameters chosen by Garrard (1982) to fit the signals from $_{26}$Fe nuclei observed in flight with energies between 0.3 and 0.8 GeV/amu. In this model, the Čerenkov response is given by the sum of three terms:

(1) Čerenkov radiation of the primary nucleus, equation (2.6) with n = 1.528. This value is higher than the values of 1.44 to 1.49 often quoted, however Ahlen et al. (1976) obtained a value of 1.518 in a fit to $_{10}$Ne data. This value represents an integral over the frequencies of the emitted photons, weighted by the spectral response of the medium and the phototubes. Since the actual refractive index is frequency dependent, different results are possible. The value n = 1.528 corresponds to a Čerenkov threshold energy of 300 MeV/amu. Because of ionization energy losses in the detector, particles at the Čerenkov threshold have energies at the top of the detector which range from ~350 MeV/amu for a $_{26}$Fe nucleus at normal incidence to ~570 MeV/amu for a $_{92}$U nucleus at 60°.

(2) Čerenkov radiation of the energetic knockon electrons, assumed to be produced according to the first Born cross section, Equation (2.3), with the light output calculated in the manner described by Lezniak (1976).

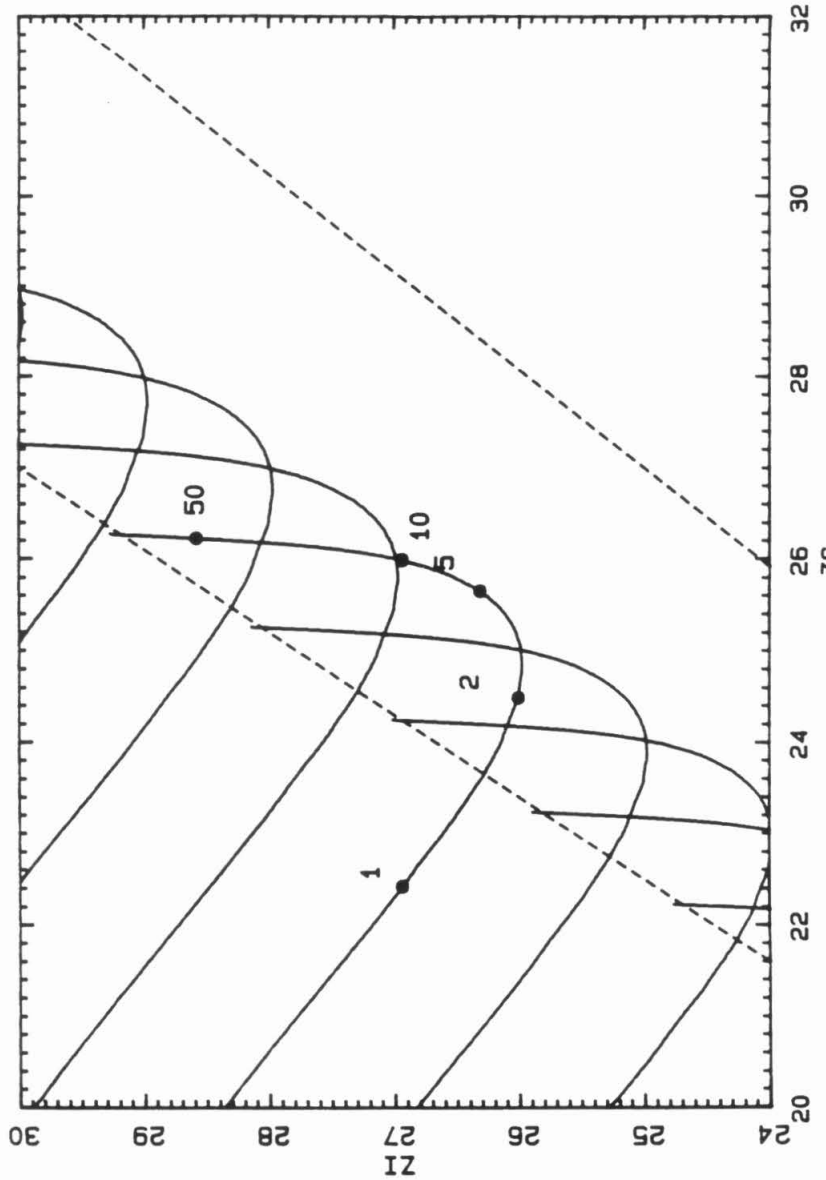

Figure 2.2 Loci of Z_I vs Z_C for elements in the vicinity of iron, calculated using the model described in the text. The iron curve has several points labeled with the corresponding kinetic energy in GeV/amu. The left hand dashed line is at $Z_C/Z_I = 0.90$; the right hand is at $Z_C/Z_I = 1.08$; these cuts are used in the data selections to be described in Chapter 3. The actual response is broadened by a resolution in Z_C of ~0.3 charge units, and a resolution in Z_I of ~ 0.4 charge units, at iron.

(3) Scintillation of the radiator material, assumed to be proportional to the ionization energy loss of the primary particle in the radiator. The normalization chosen for this term gives a scintillation contribution of ~3% of the total light output for a $\beta = 1$ particle.

The ion chamber response is assumed to be given by:

(4) The ionization energy loss of the primary nucleus, using the proton tables of Barkas and Berger (1964).

(5) A correction for the energy carried in and out by knockons, using the first Born cross section.

Each term is assumed to scale as Z^2 at any particular energy. The square roots of the signals are plotted to give displacements proportional to the particle charge, and each curve represents a particular element with energy a parameter along the curve. Several points should be noted: first that the ionization signal has a broad minimum around 2.4 GeV/amu, secondly that the Čerenkov signal is nearly constant above about 5 GeV/amu, and thirdly that various corrections, not all proportional to Z^2, must be applied to equations (2.2) and (2.3) to fully describe the response. The ionization scale normalization in Figure 2.2 has been chosen so that the square root of the pathlength-corrected ionization signal, Z_I, is 26 "charge units" for a minimum ionizing $_{26}$Fe nucleus. Likewise the Čerenkov normalization has been chosen to give the square root of the pathlength corrected Čerenkov signal, Z_C, a value of 26 charge units for a $_{26}$Fe nucleus having a kinetic energy of ~10 GeV/amu. Because the response of both detectors is proportional to Z^2 to first order, the square roots of the signals are proportional to the particle charge.

Had the spacecraft been flown in an equatorial orbit, the effect of the earth's magnetic field would have limited the observation to particles with rigidity $\gtrsim$7.6 GV, corresponding to kinetic energy $\gtrsim$ 2.2 GeV/amu, for A/Z = 2.5, where A is the nuclear mass. Because the cosmic ray energy spectrum is still rising below this energy, many more particles can be observed if an inclined orbit is used. For the HEAO-3 orbit inclination of 43.6° and altitude of 496 km, the minimum cutoff rigidity was ~1200 MV, corresponding to 120 MeV/amu,

although of course the average cutoff was much higher than this. An approximate rigidity spectrum of the observed particles will be derived in Section 3.4.

The data obtained by the instrument can be conveniently subdivided into several classes. Firstly, those particles whose trajectories imply a high geomagnetic cutoff rigidity must have a high kinetic energy, so that Z_C alone is a good estimate of the particle charge. The remaining particles can be classified by the ratio Z_C/Z_I. Particles with $Z_C/Z_I \lesssim 0.8$ lie on the low energy branch of the (Z_C, Z_I) curves, while those with $0.8<Z_C/Z_I<0.9$ are somewhat contaminated by extremely energetic particles of a lower charge. Particles with $0.9 \leq Z_C/Z_I \leq 1.08$ lie in the ambiguous "crossover" region where any one of several different elements could have produced the observed signals, when the curves of Figure 2.2 are combined with the finite instrument resolution. In this thesis, the high cutoff particles have been combined with the ambiguous group to maximize the total number. The ambiguous class contains more than half of the particles observed by the Heavy Nuclei Experiment.

Because accelerator beams of relativistic heavy nuclei heavier than iron were unavailable, the Heavy Nuclei Experiment was launched without calibration. The lack of a calibration does not pose a significant problem for data analysis if the abundant $_{26}$Fe peak can be identified and if the charge resolution and numbers of particles are sufficient to see individual elements and hence define the charge scale. Because even-charged elements are generally more abundant than odd elements these requirements are satisfied for $Z \leq 42$, for example see Binns et al. (1983a), which also shows that the assumption of Z^2 scaling is an excellent approximation in this charge range, at least for the high rigidity and low energy data sets. With fewer particles and a less favourable even-odd ratio above Z=42, there is no immediate proof that Z^2 scaling still holds, however the situation improves again in the Z = 50-58 region where even charge peaks are discernable in the Čerenkov signals of high energy particles (Krombel, 1983, and Binns et al., 1983b). Above the $Z \simeq 50$ region the statistics decline again and with the resolution continuing to deteriorate, previous work to determine abundances in the platinum-lead region was only able to discern the general abundance minimum in the low 70s, the $_{76}$Os$-_{77}$Ir$-_{78}$Pt

peak, the $_{82}$Pb peak and the "actinide gap" (Binns et al., 1985). Because a charge difference of one represents a change of only 2.5% in the signals at Z=80, it is necessary to understand the corrections to equations (2.2), (2.3), and (2.6), and also to understand the charge dependence of the instrument resolution.

2.2. Non-Z^2 Effects

A more complete form of equation (2.2) is given by Ahlen (1980 and 1982) and summarized by Waddington et al. (1983, 1985):

$$\frac{dE}{dx} = \frac{4\pi N Z_m e^4}{mc^2}\frac{Z_{eff}^2}{\beta^2}\left[\ln\left(\frac{2mc^2\beta^2\gamma^2}{I_{adj}}\right) - \beta^2 - S - D + M - B + R_B\right] J \qquad (2.7)$$

where dE/dx is in MeV cm^{-1} and N is the number density of absorber atoms having mean atomic number Z_m. Z_{eff} is the effective charge of the projectile caused by electron pickup and is given by Pierce and Blann (1968) as

$$Z_{eff} = Z\left[1 - \exp(-130\beta Z^{-2/3})\right] \qquad (2.8)$$

$S = C(\beta, I_{adj})/Z_m$ is the atomic shell effect of Barkas and Berger (1964). For an argon medium, this correction is of ~0.03% at 400 MeV/amu and smaller at higher velocities.

$D = \delta(Z_m, \beta, I_{adj})/2$ is the relativistic density effect correction, which becomes important at a few GeV/amu in solids and at tens of GeV/amu in gases near atmospheric pressure.

$M = G(Z_{eff}, \beta, I_{adj})/2$ is the correction for Mott scattering of the atomic electrons by the distributed charge on the projectile. This term accounts for the extra production of knockon electrons, beyond that predicted by the First Born cross section of (2.3).

$B = f(Z_{eff}\alpha/\beta)$ is the Bloch (1933) correction for electron binding in close collisions, evaluated in a non-relativistic way.

$R_B = C(Z_{eff}, \beta, \vartheta, \lambda)$ is the relativistic Bloch correction, which has been derived in the third Born approximation by Ahlen (1982). ϑ and λ are

parameters of the theory and must be chosen.

$J = F(\beta, Z_m)$ is the low-velocity correction of Jackson and McCarthy (1972) and deviates from unity only at energies lower than used here.

Evidence in favor of the use of all terms in Equation (2.7) has been provided by Ahlen and Tarlé (1983) for $_{92}U$ nuclei in a copper medium, and most recently by Waddington et al. (1985) for $_{54}Xe$, $_{67}Ho$, $_{79}Au$, and $_{92}U$ in emulsion.

Because knockon electrons deposit energy away from the primary trajectory, it is important to understand how their propagation and energy loss affects the instrument response, noting that the Mott cross section for their production rises substantially faster than the Z^2 scaling of Equation (2.3). In the case of the ionization measurement there are two knockon effects: first the nonequlibrium effect mentioned in section 2.1, in which knockons created by a high-energy particle will leak out of the chamber with an insufficient replacement from above; and secondly from the screenwire electrodes. There are 11 such screens in each ion-chamber module and although the mean areal density of each screen is only 0.0213 gcm^{-2}, the local density fluctuates from almost zero to 0.070 gcm^{-2} at the wire crossings and is 0.035 gcm^{-2} at the thickest point of the wire elsewhere.

Consider an incident particle which passes through a hole in a particular screen. The cloud of associated knockons diffuses out to a radial extent greater than the 0.16 cm grid size of the screen and thus suffers a more or less uniform attenuation as it passes through a screen layer. Now if instead the primary particle had passed through a wire a large amount of material would have been traversed and the following chamber would receive relatively more knockons than in the case where the particle traversed a hole. Thus the measured ionization will depend on the precise trajectory in a way which cannot be determined from the data, providing a limit to the ion chamber resolution additional to that given by ionization statistics.

The response of a real Čerenkov detector is also more complex than suggested by equation (2.6). Firstly there may be higher order terms in the Čerenkov process. From quantum electrodynamics we might expect higher

even powers of Z in (2.6), however Salamon et al. (1980) have found no evidence for either a Z^3 or Z^4 term for $Z \leq 26$. A second contribution to the Čerenkov light output is from the energetic knockon electrons accompanying the primary particle. For a 10 GeV/amu $_{26}$Fe nucleus, this contribution is calculated to be equal to 11.4% of the signal from the nucleus itself, in the Z^2 model described in Section 2.1. In the non-Z^2 model described in Appendix A, this contribution rises to 13.5%, because the knockon production cross section rises faster than Z^2. The third contribution to the light output comes from the scintillation of the detector medium. One might expect the scintillation to be proportional to the ionization energy deposit in the Čerenkov detector, however saturation at high levels may reduce the total light for the heaviest and slowest nuclei.

2.3. The First Bevalac Calibration

When high energy beams of nuclei heavier than iron became available at the Bevalac accelerator at Lawrence Berkeley Laboratory in late 1982, we were able to calibrate a model of the instrument consisting of the following:

(1) The ion chamber development unit ("DVU"), which was identical to the two ion chamber modules flown, i.e., consisting of three dual-gap ionization chambers, two complete planes of hodoscope wires, and two honeycomb windows. This module also contained the necessary high voltage power supplies, and the three ion chamber preamplifier units, together with their pulse height calibration capacitors. A rectangular hole of ~3 by 4 inches was cut in the honeycomb windows on each side of the DVU, leaving the inner solid face sheets intact. These holes were made to compare the response to particles which passed through the honeycomb with those which did not.

(2) A Čerenkov detector made from a spare flight radiator cut in two and mounted in a light collection box of the same depth as the flight unit but of only half the area. The box was viewed by eight photomultiplier tubes of the same type as those used in flight. A minor difference was that the

Čerenkov box was made from stainless steel rather than aluminum alloy.

(3) The second ion chamber module was replaced with two dual-gap laboratory ion chambers ("balloon chambers"), with aluminized mylar electrodes, a total gap width of 10cm each, and filled with P-10 gas.

Figure 2.3 shows the general experimental setup, which included a multiwire proportional chamber ("mwpc") to provide a system trigger and give the particle positions. Because of space limitations, the beam was steered onto the instrument with the spectrometer magnet located immediately upstream of the B40 experimental area at the Bevalac.

The instrument response was studied with beams of $^{55}_{25}$Mn at 1713 MeV/amu and $^{197}_{79}$Au at 1009 MeV/amu. Lower energy beams were obtained by placing Ta, Cu, and Pb absorbers in the beam path immediately upstream from the detector. The Ta absorbers were placed in the beam with a remote controlled "plate dropper" built at the University of Minnesota, thus reducing the number of entries into the target area, while the Cu and Pb absorbers were only required for the Mn beam. The use of absorbers in this way provides no protection against lower Z fragments from nuclear interactions inside the absorbers: the use of high Z absorbers is required to maximize the dE/dx to fragmentation cross section ratio. The particle energies at various points along the trajectory were calculated using Equation (2.7) and a detailed model of the composition and structure of each piece of material encountered.

Figure 2.4 is a histogram of the mean pulse height in the three DVU ion chambers for the highest energy Mn beam, calculated to have a mean energy of 1685 MeV/amu at the midplane of the DVU. The pulse heights in Figure 2.4 have been corrected by multiplying by the cosine of the angle of incidence, 10.3° in this case. The calculated value of dE/dx in P-10 leads to a value of w of (33±3) eV/ion pair, somewhat higher than the value of 26.6 eV obtained by Binns et al. (1981), who based their result on the pulse heights observed for minimium ionizing Fe nuclei observed in flight, as well as Z^2 scaling from the proton dE/dx tables of Barkas and Berger (1964). The uncertainty in the value of w arises because the absolute value of the calibration capacitors

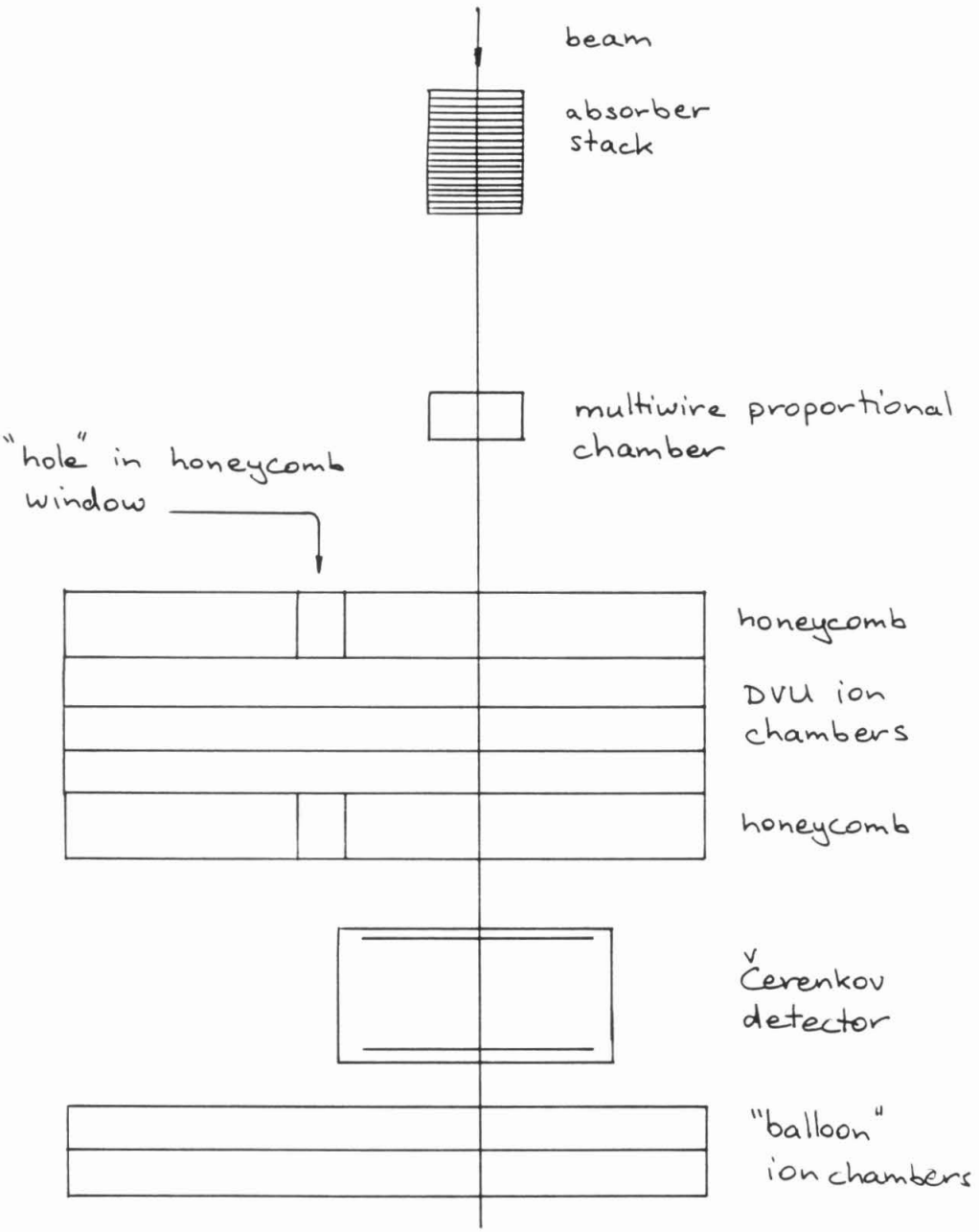

Figure 2.3 A schematic drawing of the instrument calibrated at the Bevalac in 1982, showing the tantalum absorber stack, the multiwire proportional chamber, the DVU ion camber module, the Čerenkov detector and the "balloon" ion chambers. Not to scale.

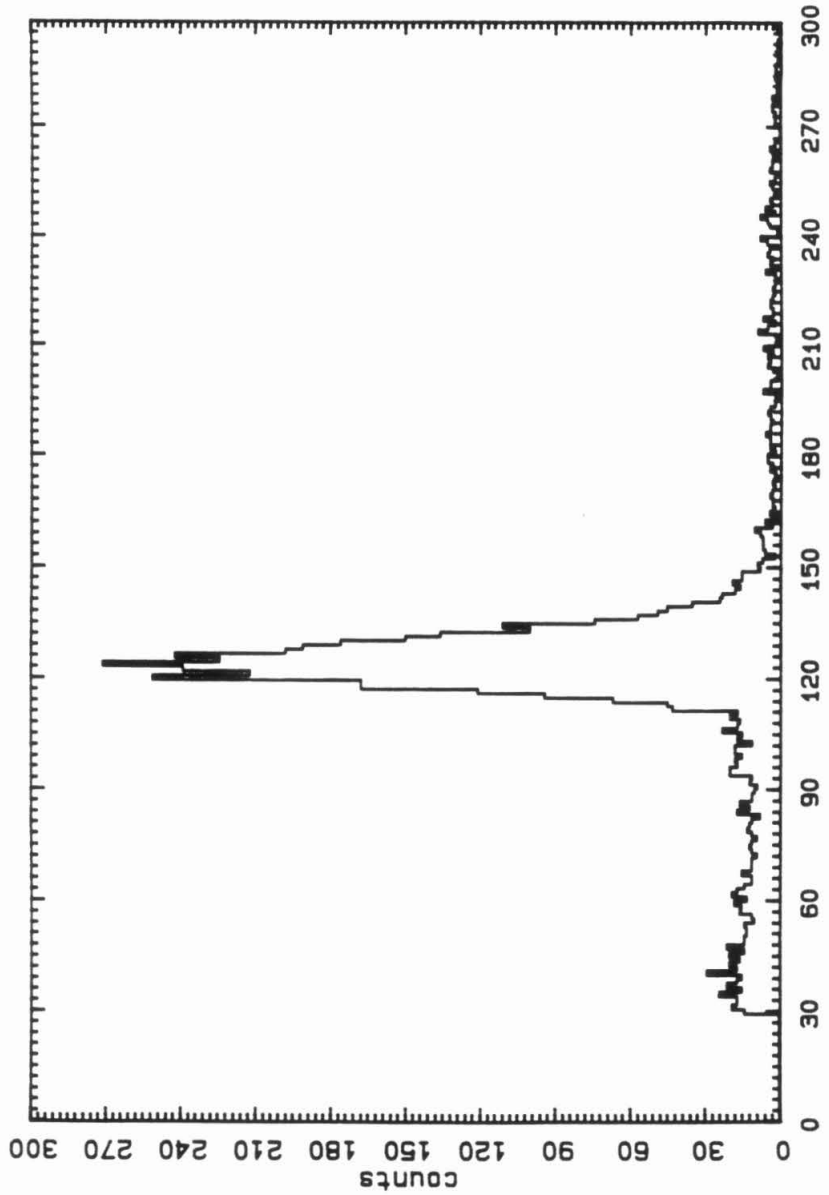

Figure 2.4 A histogram of the mean pulse height observed in the three DVU ion chambers, for a $_{25}$Mn beam of kinetic energy 1685 MeV/amu at the DVU midplane. The angle of incidence, ϑ, is 10.3°, and the pulse heights have been multiplied by $\cos\vartheta$.

(nominally 8 pF) is unknown, although their ratios have been measured by Jones (1983) and have been found to vary by ~10% from unity.

The most striking feature of Figure 2.4 is the relatively poor resolution, with a full width at half maximum (FWHM) of 12.1% of the signal, corresponding to about 1.5 charge units. The full widths at half maximum of the individual chambers are 16.6%, 15.2%, and 14.1%. One third of the quadrature sum of these values is 8.9%, which is 0.73 times the FWHM observed for the mean signal, implying a substantial correlation between the three pulse heights.

Figure 2.5 shows the mean signal in the DVU ion chambers for $_{79}$Au nuclei, at an angle of incidence of 10.3° and calculated midplane energy of 922 MeV/amu. This peak has a FWHM of 14.3%, corresponding to 5.6 charge units, and the individual chambers had widths of 17.4%, 15.8%, and 16.7%. One third of the quadrature sum of these is 9.6%, 0.67 times the observed FWHM, implying a greater correlation than with Mn. The percentage resolution of the Au signal is slightly higher than for Mn, showing that ionization statistics are unimportant here: for the 11.6 times larger signal of Figure 2.5 compared to Figure 2.4, the percentage resolution would have been a factor 3.4 smaller if ionization statistics dominated the resolution function.

Table 2.1 summarizes the FWHM data for the maximum energy Mn and Au beams at 10.3° and 59.2° angles of incidence, and compares the quadrature mean (i.e., one third of the quadrature sum) of the individual chambers with the observed width of the mean pulse height distributions. This table shows that the high angle runs have better resolution, by a factor roughly equal to the square root of the ratios of the cosines of the angles of incidence. Table 2.1 also shows the widths of the pulse height distributions obtained for beams which passed through the holes cut in the honeycomb windows. Owing to a preamplifier failure, there were no recorded pulse heights from chamber 1 during the Mn hole run. In all cases, the width of the mean pulse height distribution is greater than would be expected if the individual signals were statistically independent. The ratio of the observed width to that expected for independent chambers varies from 1.36 to 1.68, for the three-chamber

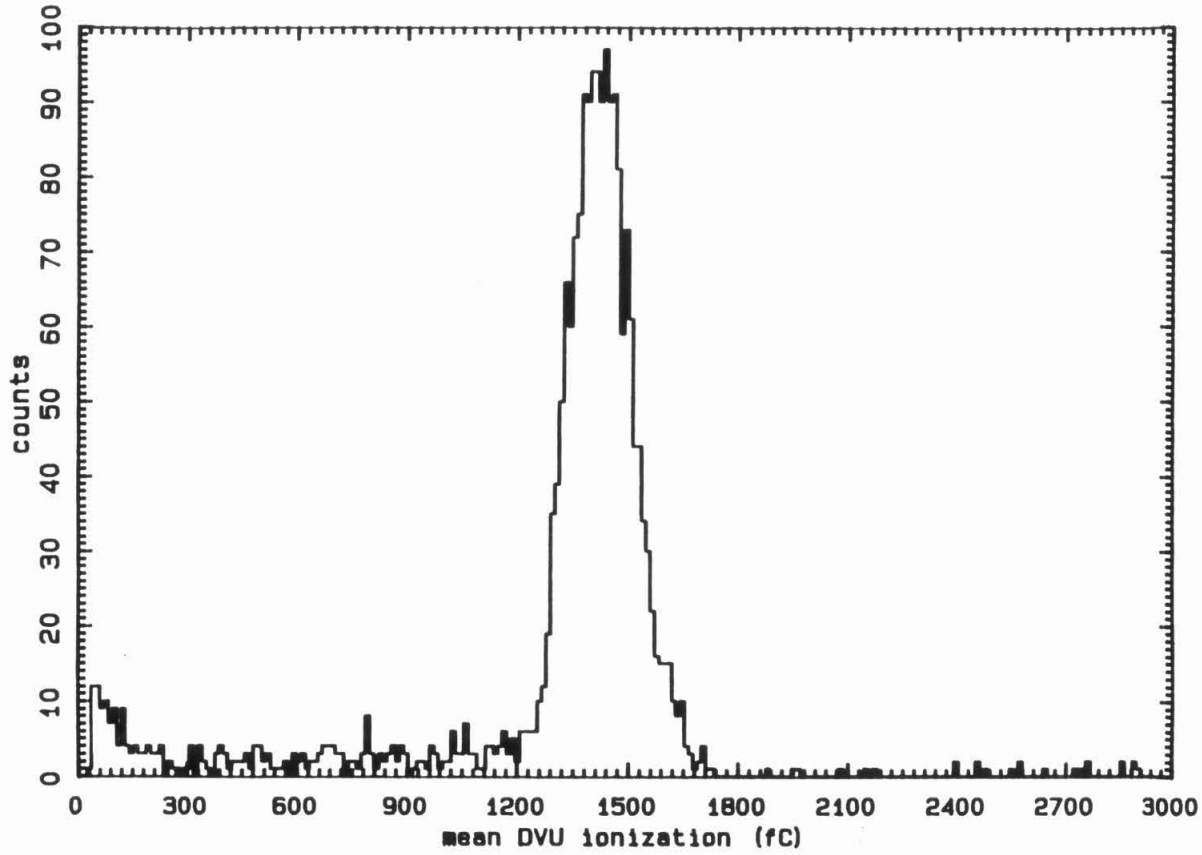

Figure 2.5 The mean pulse height in the three DVU ion chambers, for $_{79}$Au nuclei with midplane energy 922 MeV/amu, at 10.3° incidence angle.

Table 2.1

Beam	ϑ	DVU chamber			quadrature	FWHM of
		1	2	3	mean	summed signals
$_{25}$Mn	10.3°	16.6	15.2	14.1	8.9	12.1
	59.2°	11.4	10.0	12.7	6.6	9.6
	0°,hole	——	12.9	14.2	9.6	11.7
$_{79}$Au	10.3°	17.4	15.8	16.7	9.6	14.3
	59.2°	10.8	12.0	15.2	7.4	10.5
	0°,hole	13.5	12.2	15.2	7.9	13.3

Table 2.1 Full widths at half maximum of DVU pulse height distributions, expressed as a percentage of the signal at the distribution peak.

examples in Table 2.1.

One possible explanation for correlated pulse heights might be that the particles encounter variable amounts of material in the honeycomb windows, leading to energy straggling or other effects, however reference to Table 2.1 shows that removal of the honeycomb window had only a slight effect on the resolution compared to the 10.3° data. The 10.3° angle of incidence was chosen, rather than normal incidence, because the path length in the honeycomb is the same for 96% of the particles at this angle. A much larger variation would have been encountered at 0°, partly because of imperfections in the honeycomb.

In addition to the variable amount of material introduced by the honeycomb, the particles encounter further variations in the screenwire electrodes. For the 1685 MeV/amu Mn beam, the energy loss incurred in traversing a single wire diameter is 1.25 MeV/amu, causing an increase in dE/dx in the

following gas layer of 0.0037%; for the 922 MeV/amu Au beam, these figures are 4.0 MeV/amu and 0.083% respectively. Hence the poor DVU ion chamber resolution is not caused by energy straggling introduced by the screen wires.

The remaining explanation for the poor resolution is the screenwire-knockon effect described in Section 2.2, which can be tested using the data from the balloon ion chambers, with their homogeneous electrodes. Figure 2.6 shows the distribution of the mean pulse height in the two balloon ion chambers, for the high energy Mn beam at 10.3°. The mean particle energy midway between the two chambers was calculated to be 1634 MeV/amu for this run, and the calculated value of dE/dx gives a value of w of (31±2) eV/ion pair. The FWHM of the pulse height distribution is 8.0% of the signal, a factor 1.5 better than the DVU. The individual chambers have widths of 9.4% and 9.7%, yielding a quadrature mean of 6.8%, which is 0.85 times the FWHM of the mean signal. The fact that the balloon chambers did not use screenwire electrodes appears to account for their better resolution, however they are not completely devoid of screenwire: the entire balloon chamber module was enclosed in an electrostatic screen made from screenwire, which would have contributed a variable knockon component to the signals. This may be the cause of the correlation observed. Most of the variable knockon component from the DVU upstream would have been eliminated by the 2.7 gcm^{-2} of material between the interior of the DVU and the balloon chambers, since the maximum knockon energy for this beam is 6.8 MeV.

Figure 2.7 shows the distribution of balloon chamber pulse heights for the highest energy Au beam, again at 10.3°. The mean energy at the balloon chamber midplane was calculated to be 825 MeV/amu for this run. The FWHM of this peak is 6.6%, better than that for the Mn case, although still not as good as if ionization statistics dominated. The individual widths were 6.9% and 9.0%, with a quadrature mean of 5.7%, 0.86 times that observed. The intrinsic resolution of the balloon chambers is in fact significantly better than that implied by Figure 2.7: Figure 2.8 shows a histogram of the mean balloon chamber pulse height for the high energy Au beam at an angle of incidence of 169.7°, i.e., with the particles entering the balloon chambers first. The

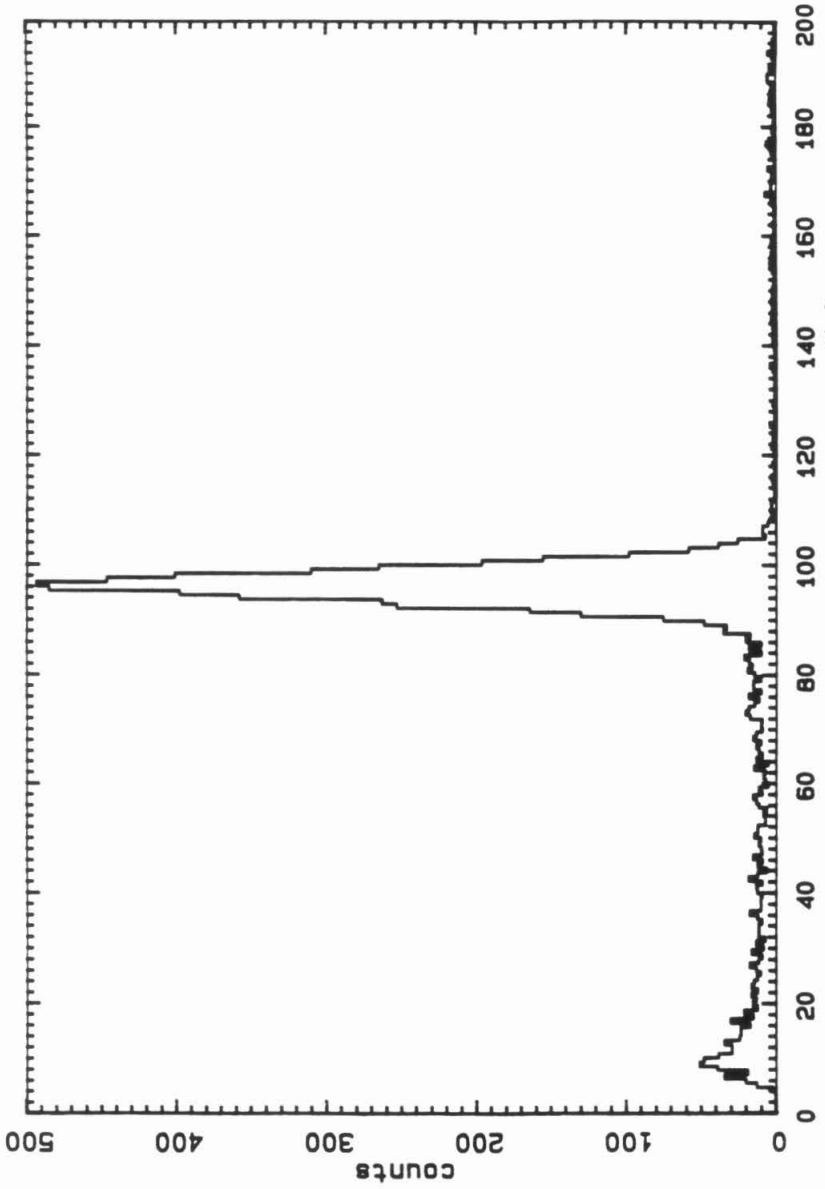

Figure 2.6 The observed mean of the two ballon chamber pulse heights, for $_{25}$Mn nuclei with a midplane energy of 1634 MeV/amu.

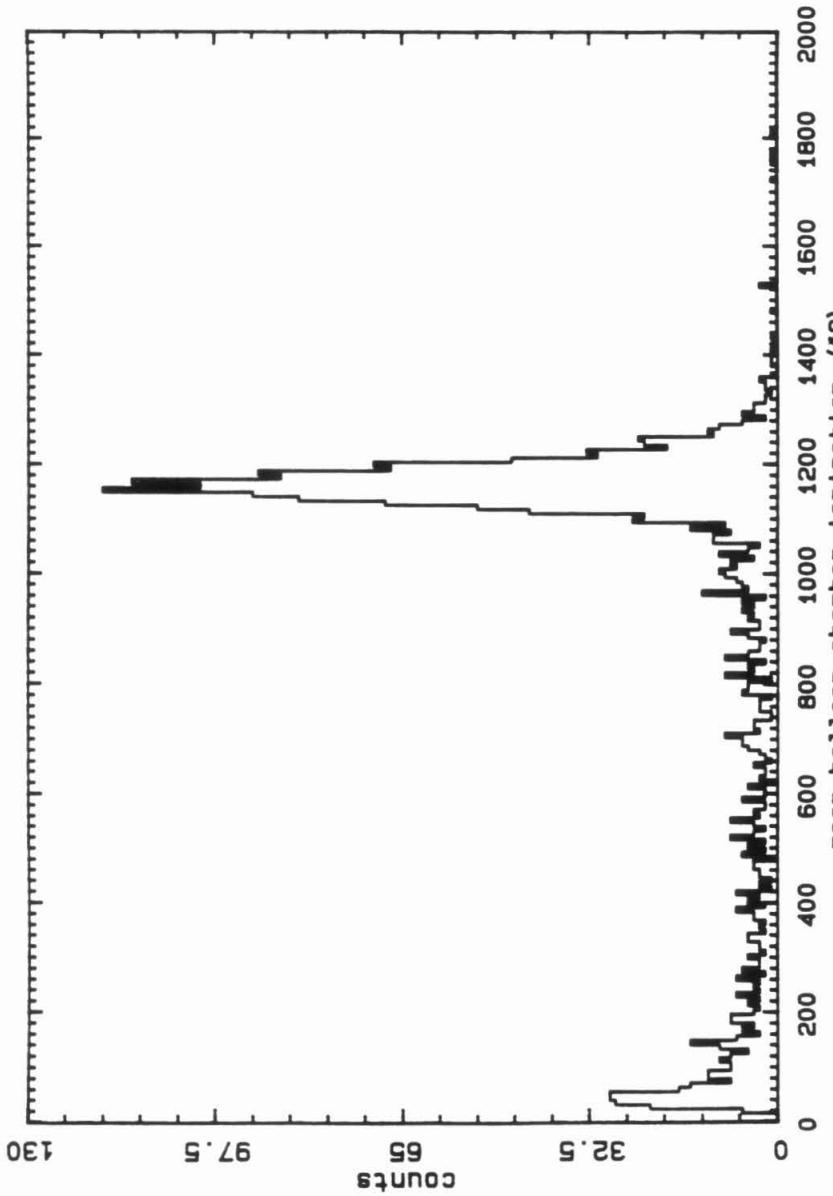

Figure 2.7 Mean balloon chamber pulse heights for $_{79}$Au nuclei at 10.3°. The mid-plane energy is calculated to be 825 MeV/amu.

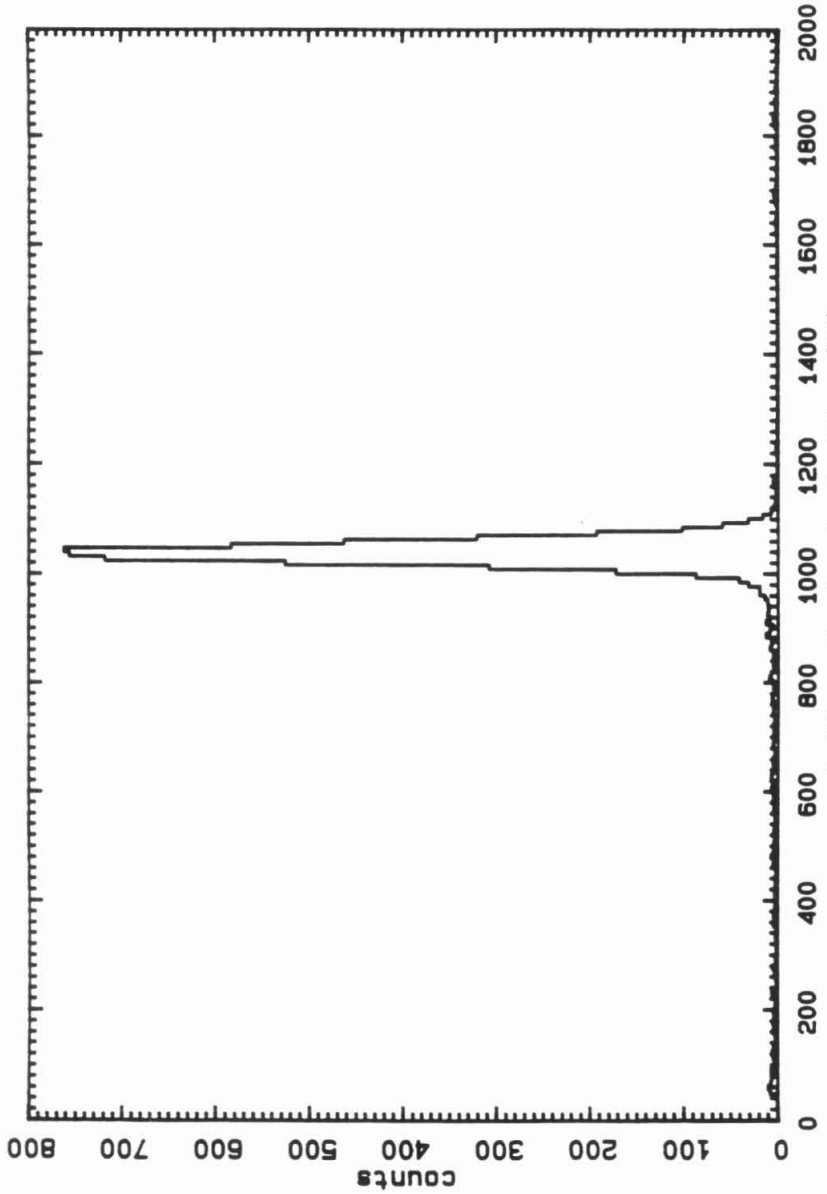

Figure 2.8 Mean balloon chamber pulse heights for $_{79}$Au nuclei at 169.7°, i.e. entering the these chambers first. The resolution is appreciably better than the 10.3° case illustrated in the previous figure.

midplane beam energy in the chambers is calculated to be 960 MeV/amu, and the peak is much narrower, with a FWHM of 4.4% of the mean signal. The individual chambers have widths of 6.3% and 5.3%, giving a quadrature mean of 4.1%, implying only a small correlation between the chambers. There was no corresponding run at this angle for the Mn beam, owing to beam time constraints. Table 2.2 summarizes these balloon chamber results, as well as those obtained from the hole runs. It is apparent that the honeycomb has little effect on the balloon ion chamber resolution for the Mn beams, but may account for some of the degradation in the case of Au.

Table 2.2

Beam	ϑ	chamber		FWHM of sum
		1	2	
$_{25}$Mn	10.3°	9.4	9.7	8.0
	0°,hole	9.1	9.9	7.5
$_{79}$Au	10.3°	6.9	9.0	6.6
	0°,hole	6.5	6.4	5.0
	169.7°	6.3	5.3	4.4

Table 2.2 Full widths at half maximum of the balloon chamber pulse height distributions, expressed as a percentage of the mean signal.

Several conclusions may be drawn from the preceding results:

(1) The use of screenwire electrodes in the flight ion chambers introduced a serious degradation of the resolution, compared to that achievable with homogeneous materials.

(2) The presence of the DVU with its eleven layers of screenwire and two honeycomb windows was sufficient to degrade the resolution of the balloon chambers downstream. Because of the intervening (and homogeneous) Čerenkov counter, this effect is probably not caused by screenwire-induced fluctuations in the knockon cloud. A more likely explanation is that the energy straggling of the beam caused by thickness variations in the screenwires and honeycomb is greater than simple estimates would predict.

(3) Although angle dependent, the resolution of the flight ion chambers is well approximated as a fixed fraction of the pulse height, independent of Z.

Figure 2.9 shows the observed mean DVU pulse heights for the Mn and Au beams as a function of energy at the midplane. These data are for an angle of incidence of 10.3°, and have been scaled by $1/Z^2$. The solid curve represents the value of dE/dx for $_{25}$Mn nuclei in P-10 gas, normalized to the highest energy Mn point. The lower energy Mn data fit this curve well, showing that the calculated energy loss of the Mn nuclei in the absorbers and detector is probably not seriously in error. The dashed curve represents dE/dx for $_{79}$Au, and shows a large positive non-Z^2 effect in the relativistic rise region and a small negative non-Z^2 effect at low energies. The observed ionization at the highest energy Au point is (6±2)% higher than that predicted by Z^2 scaling, as well as being higher by the same amount from the value predicted by the dE/dx calculation. This non-Z^2 effect is equivalent to 2.4±0.6 charge units, and cannot be caused by a gross error in the calculation of the Au energies since the total energy loss from the beam exit window to the midplane of the DVU is only 87 MeV/amu, for the highest energy Au point. Even a 20% error in the energy loss would be insufficient to move the Au data over to the Mn curve.

Because of the uncertainties in the amount of material traversed, it was not possible to reliably determine the size of the non-Z^2 effects, if any, in the balloon ion chambers. Had there been a manganese run with the beam entering the balloon chambers first, such a measurement would have been

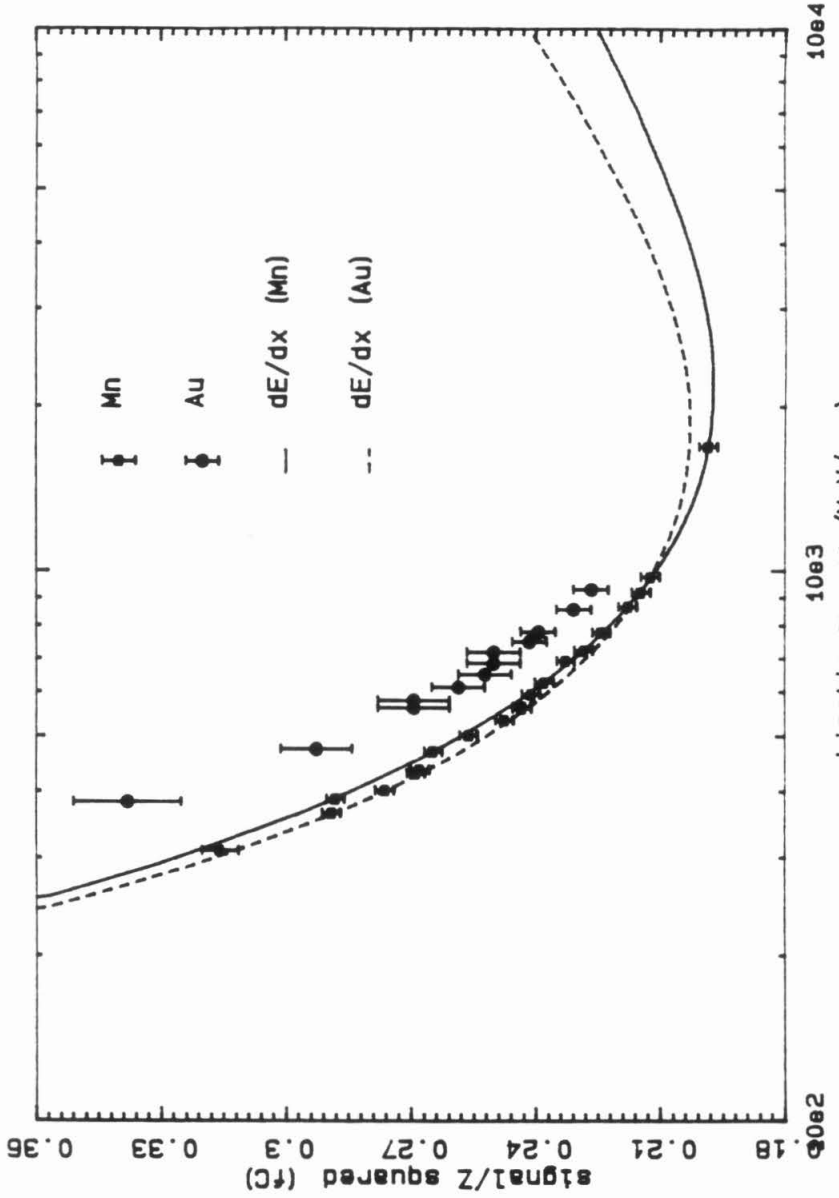

Figure 2.9 DVU pulse heights as a function of the calculated midplane energy, at 10.3°. Because of a preamplifier failure the signals from Chambers 2 and 3 only have been used. The curves show the calculated values of dE/dx in P-10 gas.

posssible.

The results on the DVU are less useful than was hoped: from Figure 2.9 it is unclear whether the non-Z^2 effect persists at higher energies, where most of the flight data lie. It should be noted that the response in the relativistic rise region is expected to be less than indicated by dE/dx, owing to the knockon nonequilibrium effect described in Section 2.1. At the Bevalac there was sufficient material, both within the front window and upstream, for there to be no evidence of the nonequlibrium at energies up to ~1700 MeV/amu.

Resolution problems caused by inhomogeneity were not confined to the ion chambers: because of its extreme velocity sensitivity at energies below 1 GeV/amu, the results from the Čerenkov detector were inadequate to enable a conclusion about the existence of non-Z^2 effects at higher energies. There were few well resolved Čerenkov peaks owing to the velocity spread at the detector, and in addition, small changes in the assumed thickness of the various detector elements have a significant effect in the calculation of the Au beam energies.

2.4. The Second Bevalac Calibration

When more time became available at the Bevalac, we returned with a new detector designed to study the physics of ion chambers and Čerenkov detectors without the complications experienced in the first calibration. Figure 2.10 is a schematic drawing of the new instrument and the experimental setup. Six dual gap ion chambers were built at Washington University, with an electrode spacing similar to that of the Heavy Nuclei Experiment. These chambers used windows and electrodes made from aluminized mylar of thickness ~0.8mgcm^{-2} to minimize the amount of material and reduce areal nonuniformities. The Čerenkov detector, built at the University of Minnesota, used a piece of Pilot 425 from the same batch as the flight radiator. The 1984 calibration used beams of $_{26}$Fe, $_{36}$Kr, $_{54}$Xe, $_{67}$Ho, $_{79}$Au, and $_{92}$U at maximum energies ranging from 1686 MeV/amu for Fe to 889 MeV/amu for U.

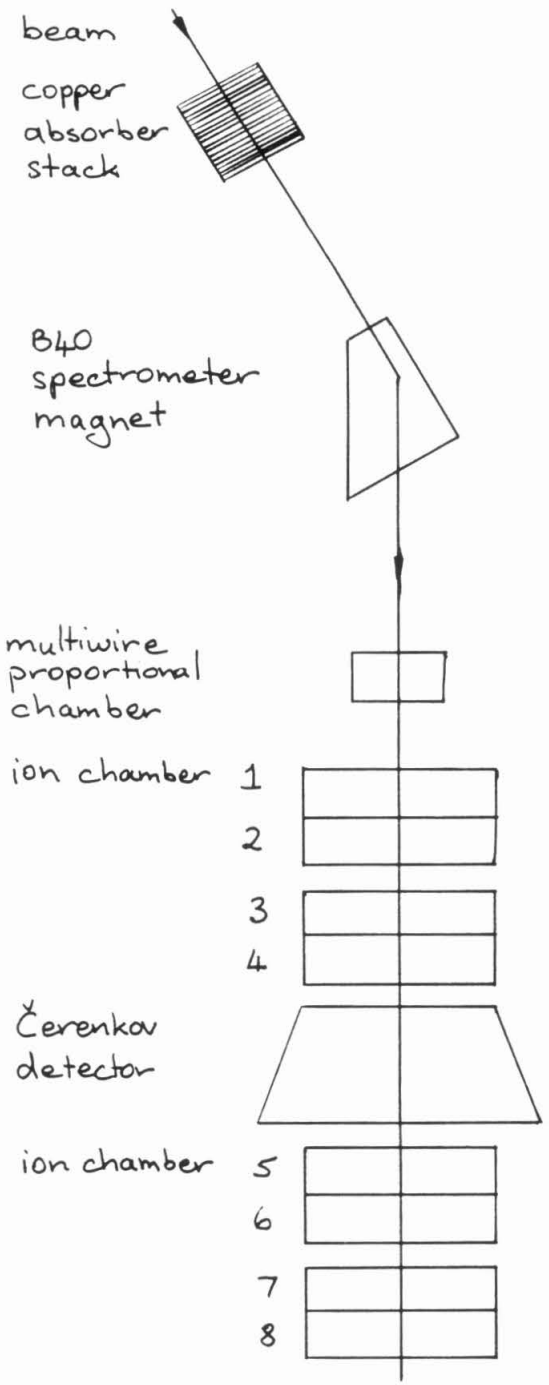

Figure 2.10 A schematic view of the 1984 calibration setup, showing the upstream Cu absorbers, the spectrometer magnet, the multiwire proportional counter, the six ion chambers, and the Čerenkov detector. Not to scale.

Lower beam energies were obtained by placing copper absorbers in the beam line, upstream from the spectrometer magnet, rather than downstream as in the first calibration. This procedure had two advantages. Firstly, the degraded beam energies were much better determined since we could determine the energy directly by observing the magnet current required to place the beam spot on our instrument, thus avoiding most of the uncertainties involved in calculating the energy in each detector element. Secondly, any fragmentation products having rigidities different to the primary beam were effectively removed, thus contributing to the beam purity. Although fragments initially have almost identical velocities as the parent nuclei, they can have different rigidities both by having a different A/Z and by slowing less rapidly in the following material, because the value of Z^2/A is lower.

The disadvantage of upstream absorbers is that the amount of energy loss in the absorber must be well known in advance to determine the magnet current required for a particular absorber thickness. In practice, we determined the nominal energy steps beforehand, together with the predicted magnet settings. The amounts of copper required for these nominal energies were calculated using Equation (2.6) and the (just) measured primary beam energy. Using small energy steps, we were able to adjust the nominal magnet settings to keep the beam spot centered on the multiwire proportional chamber. This procedure broke down slightly for the lowest energy steps with the Au beam, because some nuclei had one or two attached electrons, resulting in mutilple charge states. Electron attachment was quite severe with the U beam, where multiple charge states were always present, requiring some judgment as to which spot, if any, was "correct".

Figure 2.11(a) shows the Čerenkov pulse height distribution for the iron beam, with an energy at the center of the radiator of 1640 MeV/amu. while Figure 2.11(b) shows the pulse height distribution for the uranium beam at 750 MeV/amu (assuming that the principal beam spot had a charge state of 91+). The pulse height in both cases is in arbitrary units, which have been scaled down by Z^2. The full width at half maximum of the iron distribution is 2.4%, implying an rms resolution of 0.13 charge units. The full width at half

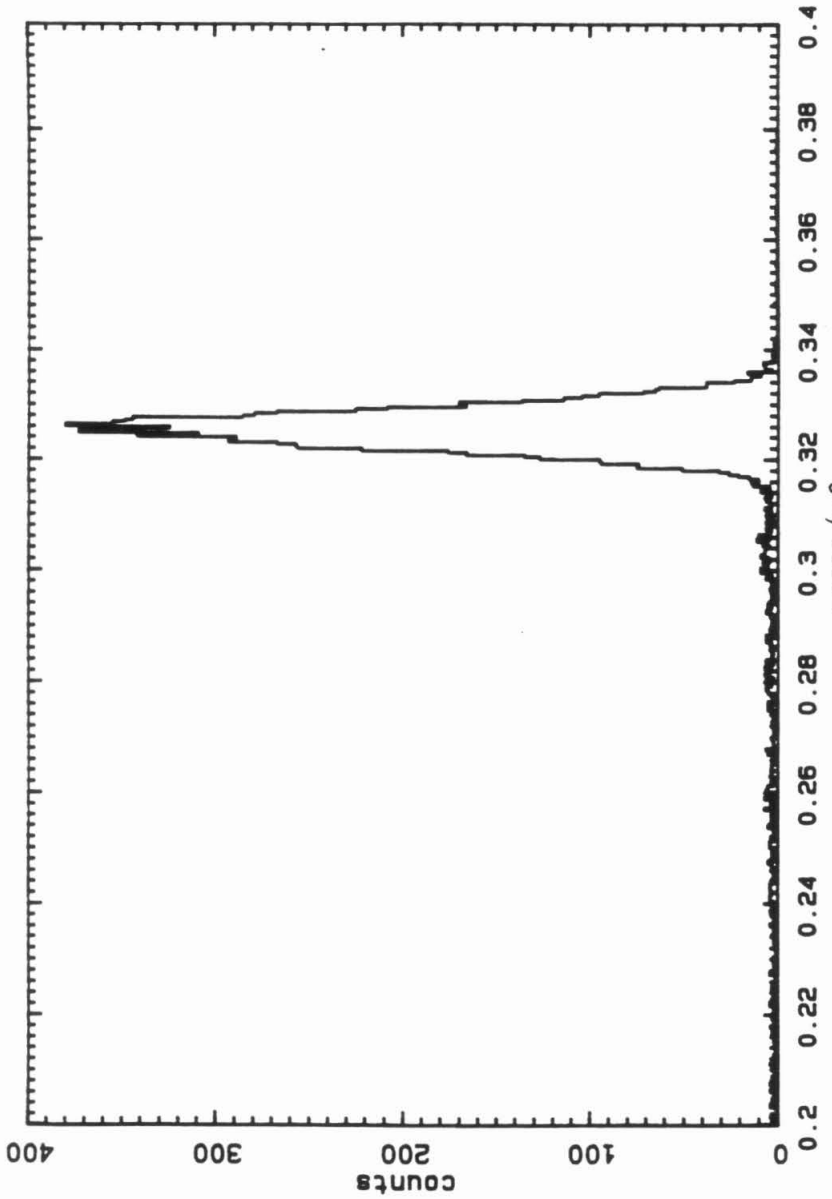

Figure 2.11(a) The Čerenkov light output distribution of $_{26}$Fe nuclei at 1640 MeV/amu, at the 1984 Bevalac calibration. The light output units are arbitrary, and have been scaled down by Z^2.

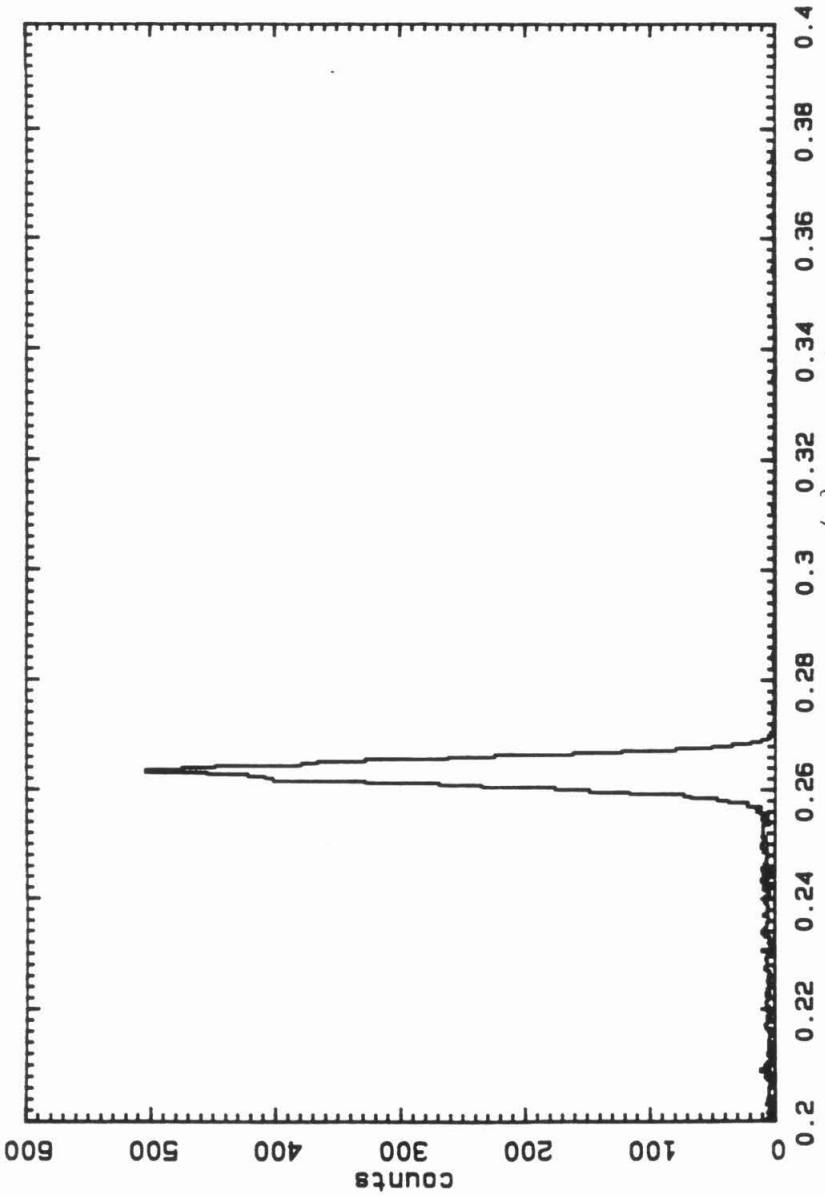

Figure 2.11(b) The Čerenkov light output distribution of $_{92}U$ nuclei at 750 MeV/amu. The units are the same as the previous, and have been scaled by $1/Z^2$.

maximum of the uranium distribution is 2.1%, implying an rms resolution of 0.40 charge units. Although not applicable to the flight data because of the different construction of this detector, these excellent figures enabled measurements of the partial cross sections for charge changing interactions. The fragmentation data is currently being analyzed at the University of Minnesota, and some preliminary results are given in Kertzman et al. (1985).

Figure 2.12 shows the Čerenkov signals of $_{26}$Fe, $_{79}$Au, and $_{92}$U, divided by Z^2 and plotted as a function of $1/\beta^2$. β was calculated at the center of the Čerenkov radiator. In the case of uranium, the results are shown for two assumptions about the charge state within the magnetic spectrometer: either 90+ or 91+. Because of the difficulty of distinguishing between the multiple charge states present, the uranium data must be considered with caution. The straight line in Figure 2.12 represents the result of a linear fit to the Fe data for $1/\beta^2 < 2.3$, and shows that the Čerenkov response is well approximated by a function proportional to Z^2/β^2 in the energy range 0.3 to 1.6 GeV/amu. Furthermore, there is little evidence for a non-Z^2 scaling law, at least between Z=26 and Z=79.

Despite the attempts made to reliably determine the energy of each beam, it was still not possible to determine the Čerenkov response with sufficient accuracy for extrapolation to flight energies. Although each beam showed a $1/\beta^2$ response similar to those given in Figure 2.12, there was a significant amount of scatter present in the pulse heights at the highest energies, and the threshold energy appeared to vary from beam to beam in a random fashion. Attempts to independently measure the beam energy with a time of flight system gave results inconsistent with that measured using the magnet on some runs. For both types of measurement the measured energies were found to depend critically on the precise beam geometry. For example, in the initial Xe runs the beam spot was observed to move when it was defocused, implying that it was not correctly centered in the quadrupole magnets. It is not known whether such effects were present in the earlier runs (Fe, Kr, and Au), since no defocusing test was tried. These problems made it impossible to determine the precise Z dependence of the Čerenkov radiation.

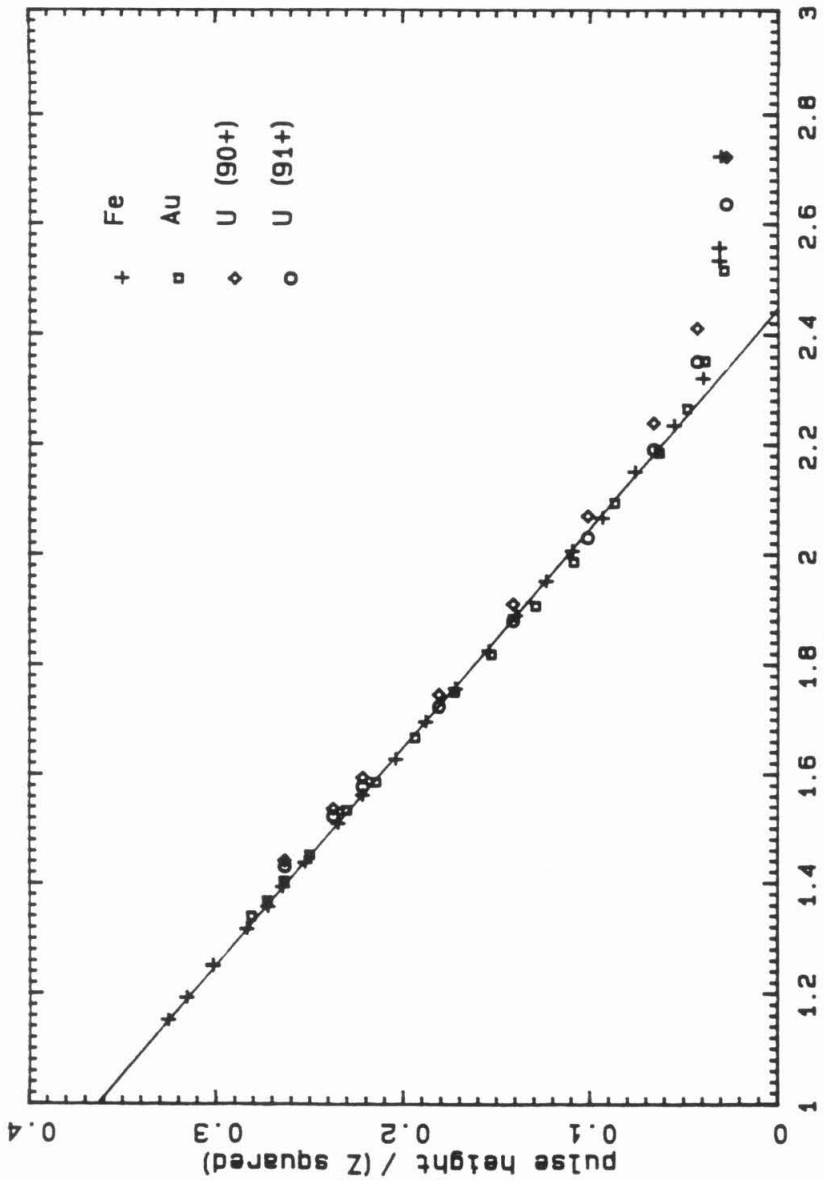

Figure 2.12 The Čerenkov pulse height distribution as a function of $1/\beta^2$, calculated at the center of the radiator, for beams of Fe, Au, and U nuclei. The pulse heights have been scaled by $1/Z^2$. See text for discussion of the uranium data.

Since the ion chamber response with energy is much weaker than the Čerenkov detector, some useful results may be obtained. Figures 2.13(a) and 2.13(b) show histograms of the pulse height in chamber 1 for $_{26}$Fe and $_{79}$Au nuclei with ~1 GeV/amu kinetic energy. The full widths at half maximum of these peaks are 5.7% and 2.6% respectively, compared to the best value of ~5% observed for Au in the balloon ion chambers in the 1982 calibration. The simple model of Epstein et al. (1971) predicts that knockon fluctuations will result in a full width at half maximum of 5.4% of signal, in the limit of a zero thickness lid, for $_{26}$Fe at 1 GeV/amu. The width goes as $1/Z$ in that model, implying an expected fwhm at Au of 1.8%, about 0.7 times the observed value. Since the simple model is based on Z^2 scaling of the knockon production cross section, the discrepancy is not surprising. These widths correspond to rms resolutions of 0.31 and 0.44 charge units at Fe and Au. The much improved resolution in the 1984 calibration appears to be due to the use of homogeneous materials in the beam path.

Figure 2.14 shows the response of chambers 1, 5, and 6 to $_{26}$Fe nuclei as a function of the energy at the midplane of the appropriate chamber, and compares their signals to the calculated dE/dx, arbitrarily normalized at 500 MeV/amu (requiring 27.9 eV per ion pair in the P-10 gas used (90% argon, 10% methane)). It is apparent that the signals fall below that predicted by dE/dx at energies above 700 MeV/amu. This loss of signal is somewhat surprising since at these energies we would expect knockons escaping from the exit window to be in equilibrium with those arriving from above, particularly for chambers 5 and 6 which have ~2 g cm^{-2} of upstream material. However, some of the decrease in observed signal may be due to knockons escaping from the sides of the chambers.

By interpolating to a particular energy we can construct a plot of signal versus Z at that energy. At low energies, the heaviest nuclei have an effective charge, $Z_{eff} = Z[1-\exp(-130\beta Z^{-2/3})]$, due to electron capture (Pierce and Blann, 1968). Figure 2.15 shows the pulse heights, scaled down by Z^2_{eff}, at four energies for Z = 26-79, using ion chambers 1, 5, and 6. The uranium data have not been included because the charge state in the magnetic spectrometer was

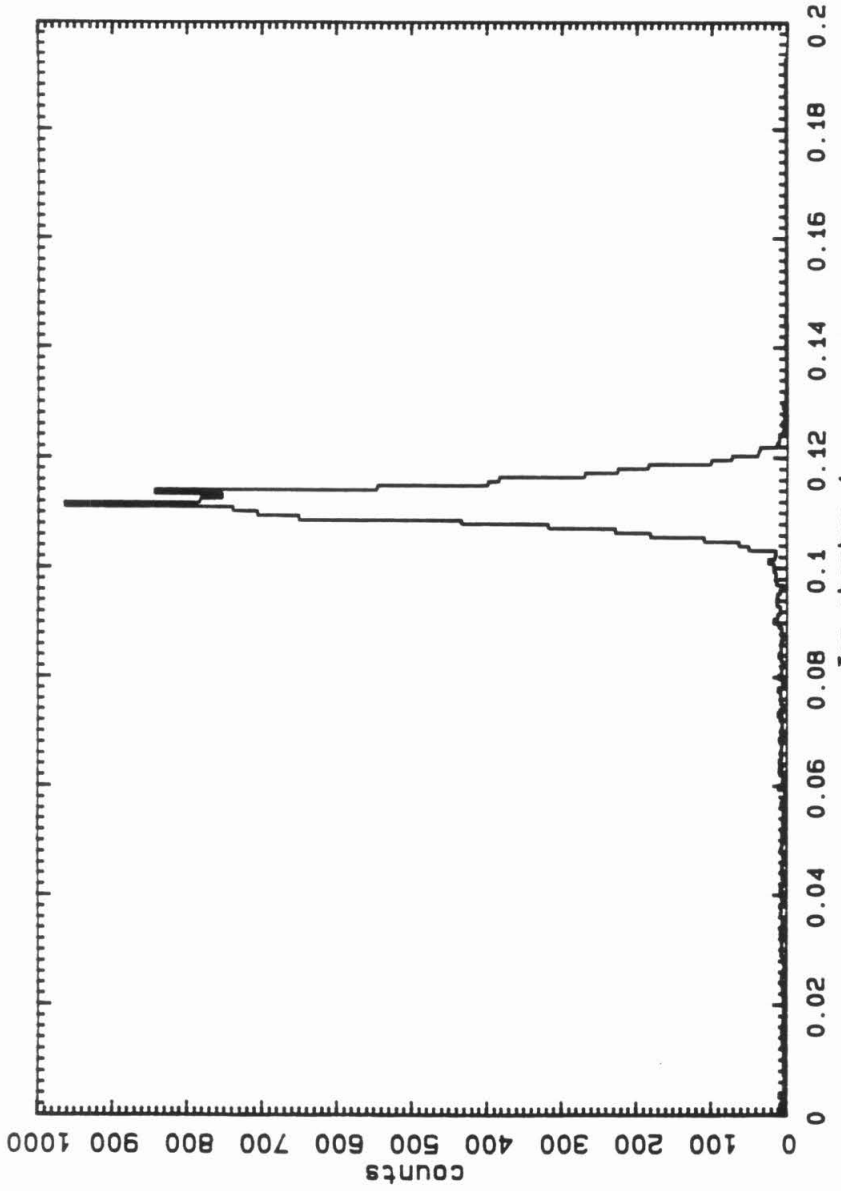

Figure 2.13(a) Pulse heights in ion chamber 1, observed for Fe at 1005 MeV/amu. The pulse height units are in femtocoulombs, and have been scaled by $1/Z^2$.

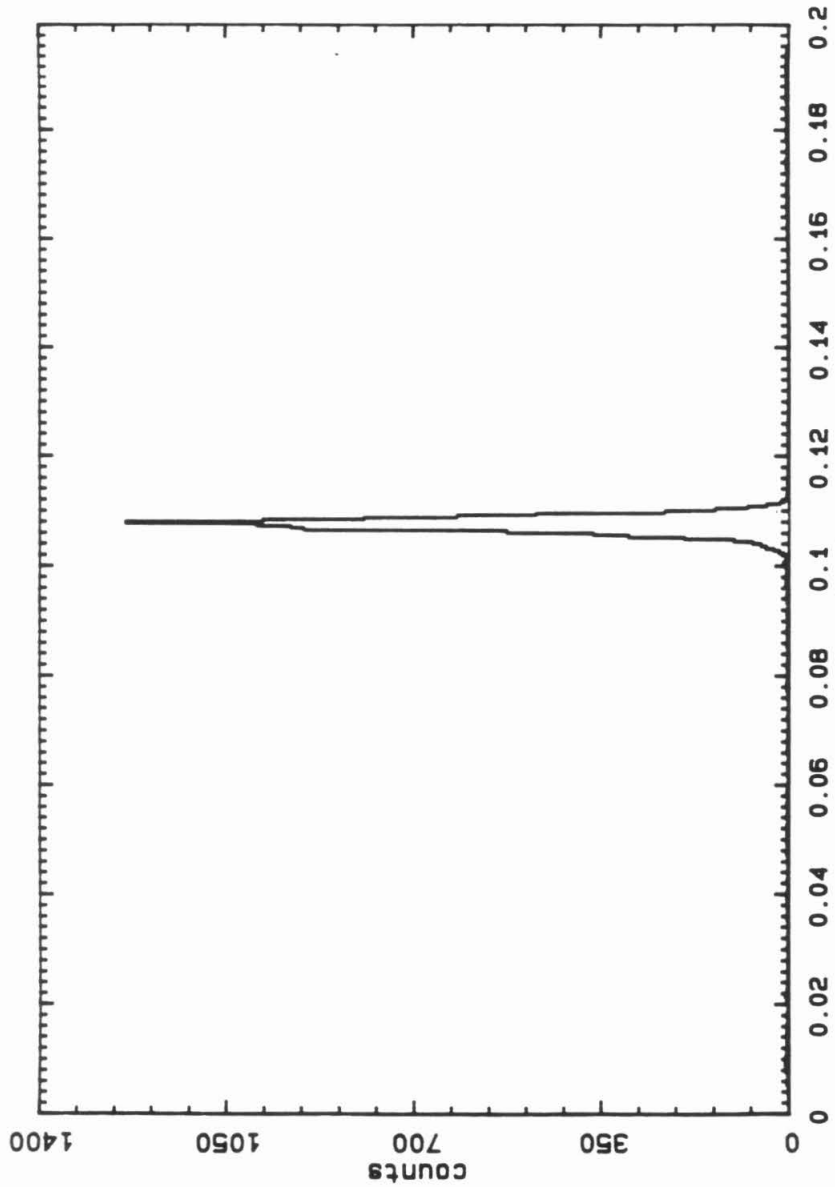

Figure 2.13(b) Pulse heights in ion chamber 1, observed for Au at 1022 MeV/amu. The units are fC/Z^2.

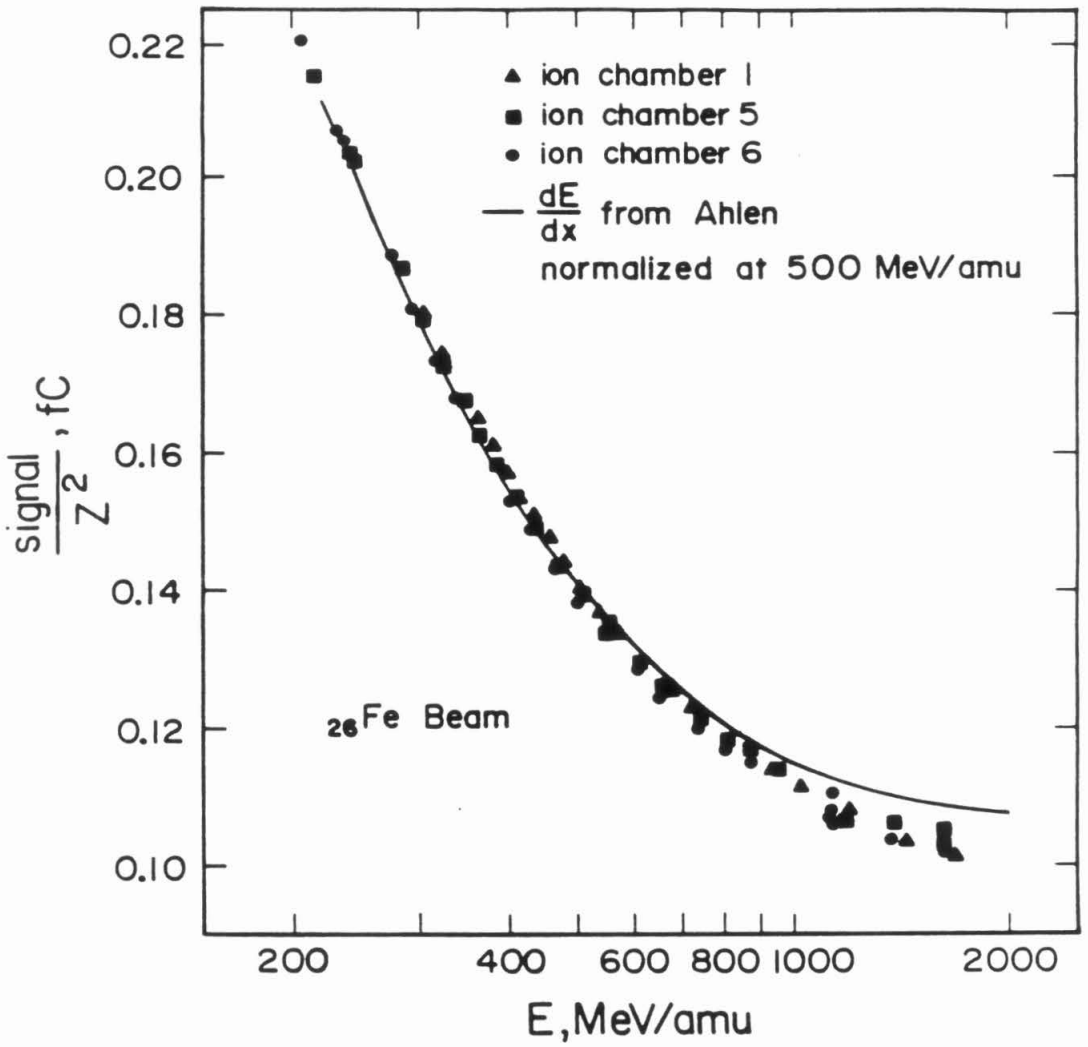

Figure 2.14 Pulse heights in chambers 1,5, and 6 as a function of energy, for Fe nuclei. The curve shows the calculated value of dE/dx, with a normalization corresponding to 27.9 eV/ion pair.

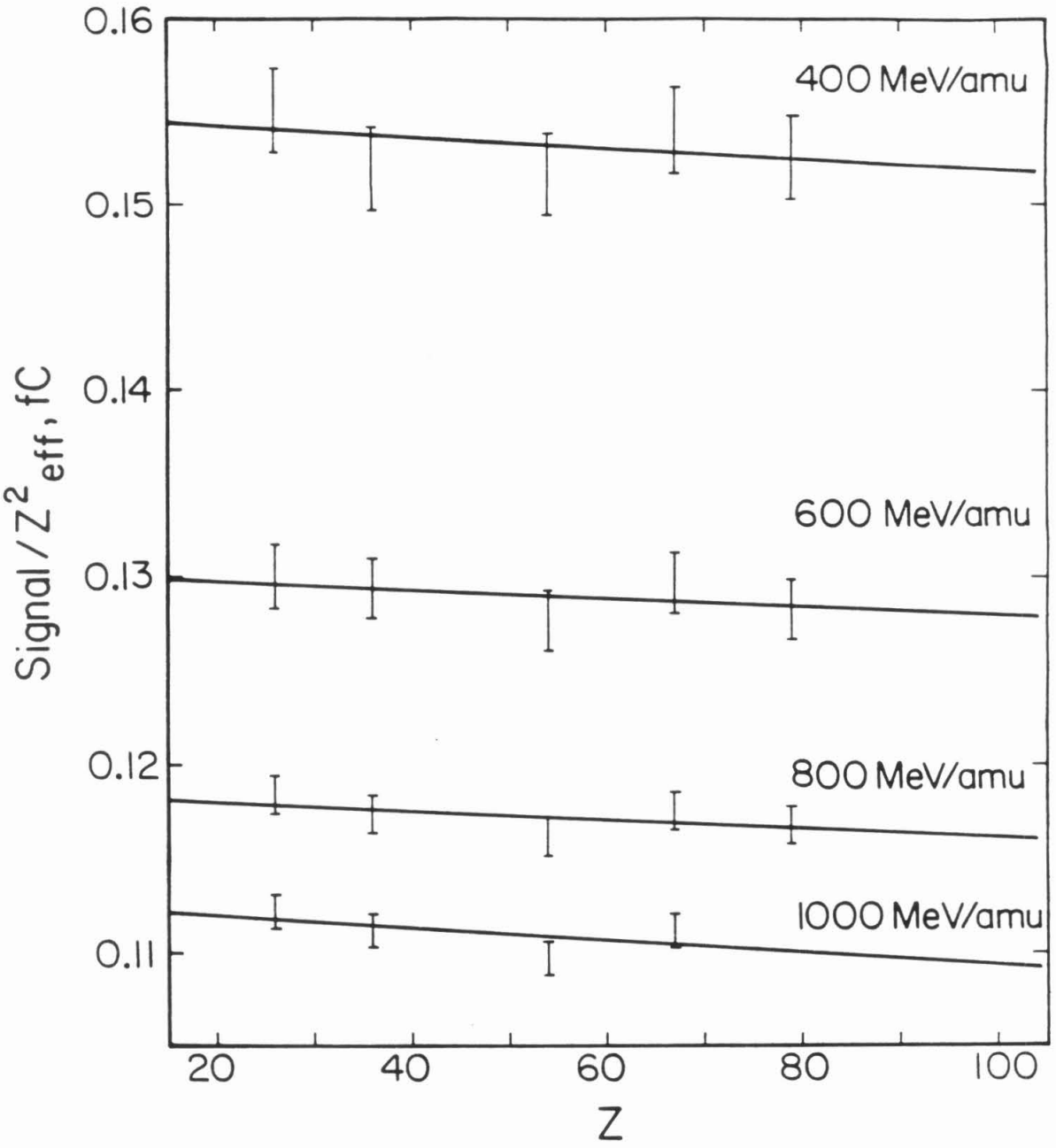

Figure 2.15 Interpolated pulse heights as a function of Z for four energies. The values represent the mean pulse heights in chambers 1, 5, and 6, with the energy calculated at the midplane of each chamber. The pulse heights have all been scaled by $1/Z^2$, and the lines are weighted linear least squares fits to the data.

too uncertain for those beams whose energy had been degraded significantly. The straight lines represent a linear fit to the data, and it is apparent that there is a small negative non-Z^2 effect. The charge of an $_{79}$Au nucleus would be underestimated by 0.7±0.5 charge units at 1 GeV/amu using these chambers, in contrast with the charge overestimate of 2.4±0.6 charge units observed in the calibration of the DVU.

At first sight the result from the 1984 calibration appears to contradict that from the 1982 calibration. Chambers without screenwires appear to show a small negative non-Z^2 effect at energies $\lesssim$ 1 GeV/amu, while those with screenwires show a larger positive effect. The simplest interpretation is that the basic response of ion chambers at these energies is slightly less than that predicted by Z^2 scaling, while the screenwires add a signal which rises faster than Z^2. The latter effect is plausible firstly because the use of screenwires instead of thin homogeneous electrodes results in a larger signal for those particles which hit a wire, and secondly because the cross section for knockon electrons rises more rapidly than Z^2. In any case, the extrapolation of the ion chamber response to higher energies is uncertain, and we must attempt to infer the deviations from Z^2 scaling directly from the flight data itself. Chapter 3 describes the results of this approach, and its application to the determination of cosmic ray elemental abundances. Evidence suggesting that there is little deviation from Z^2 scaling at flight energies will be presented in Sections 3.2.2 and 3.4.7.

Chapter 3

Data Analysis

3.1. Preliminary Analysis

This section describes the reduction of the raw data to a compact and highly refined set which is then used as a starting point for the final analysis. This work was performed at California Institute of Technology.

3.1.1. The Library Generator

The raw data from the HNE were processed with the library generator program LIBGEN, described in Krombel (1983) and Garrard (1979a). This program classified the various types of events (e.g. calibration pulser, internal radioactive source, "real" particle, etc.) and determined the particle trajectories from the hodoscope information. Using these trajectories, cutoff rigidities were calculated using the spacecraft orbit and attitude information, and a model of the geomagnetic field (Garrard, 1979b). Because the instrument did not distinguish between "upward" and "downward" moving particles, the cutoff rigidities were calculated for both directions.

The LIBGEN output is stored on computer tapes, each 2400 feet long and of 1600 bits per inch density. There are some 600 such tapes, one for each day of the mission.

3.1.2. The Gold Data Set

In order to reduce the library to a data set of manageable size, a series of selections was applied (Garrard, 1983):

1) Events occuring during the spacecraft passage through the South Atlantic Anomaly were rejected because they may be heavily contaminated by accidental coincidences with trapped protons.

2) Events with data transmission errors were eliminated.

3) Source and electronic calibration events were removed.

4) Particles were assigned preliminary estimates of Z_I and Z_C. 1/40 of all particles with $Z_I > 19.5$, chosen at random, were tagged as "lucky" and saved to make a normalization set. These particles are mostly iron nuclei.

5) Particles with $Z_I > 30.5$ or $11.0\ Z_I + 6.0\ Z_C > 500$ were defined to be "high Z", and saved. The high Z set includes all particles having $Z \geq 32$, as well as some of lower charge, but none of the iron. Some of these particles are also lucky.

6) A further small class of particles which were neither lucky nor high Z was saved because of an error in a selection algorithm.

Most of the data were eliminated by these charge cuts, since there are so few nuclei with $Z > 30$. In addition to these selections, this part of the analysis obtained improved trajectories for those particles with hodoscope pattern problems, such as extra or missing wires, and corrected Z_C and Z_I for areal nonuniformities (mapping) and time dependent gain variations. The signal from any ion chamber in which the trajectory passed closer than 8 cm to a wall was ignored to reduce any edge effects. A number of useful parameters were calculated, and will be discussed as they are used. The refined data set, known as the Gold set, consists of 2,346,498 events residing on 21 tapes, and has been used for all of the following analysis.

3.2. Final Selections

Further selections were applied to the Gold data set to obtain the final data set. These selections were deliberately kept as loose as possible to maximize the number of particles available for analysis.

3.2.1. Trajectory Cuts

Selected particles were required to have a valid signal in at least one of the three ion chambers on each side of the Čerenkov detector, i.e., one ion chamber in each module. This "two module" requirement allows the signals from the fore and aft modules to be compared later to eliminate events in which a fragmentation interaction occurred within the Čerenkov detector or the interior ion chamber windows, as well as some events in which there was an accidental coincidence with a second particle which traversed a single ion chamber module.

This selection also reduces the number of particles which entered the instrument through a sidewall. These particles may have undergone a large amount of fragmentation, as they traversed a large and variable amount of material in the sidewall, in the electronic packages attached outside, and in the spacecraft body.

The two module requirement eliminated 71.2% of the original particles, leaving 680,564. Since one module completely failed five months before the end of the mission, this selection reduced the exposure time to 454 days. Particles were also required to have a trajectory passing through both Čerenkov radiators. This selection automatically excluded particles which passed through any part of a photomultiplier tube, and eliminated 0.4 % of the remaining particles, leaving 678,182. 10.6 % of the remaining events were neither lucky nor high Z. These events were rejected, leaving 606,311.

3.2.2. Čerenkov - Ion Chamber Agreement Cuts

If both the Čerenkov and ion chamber signals scale purely as Z^2 then the ratio Z_C / Z_I should be a function of energy alone. The distribution of Z_C / Z_I is shown in Figure 3.1 . The main peak corresponds to particles whose ionization signal is near the minimum and whose Čerenkov signal is close to saturation, i.e., particles in the range 2-5 GeV/amu. This range corresponds to the peak of the energy spectrum at the detector and thus the observed particles pile up. The sloping tail region on the low side of the peak is comprised of

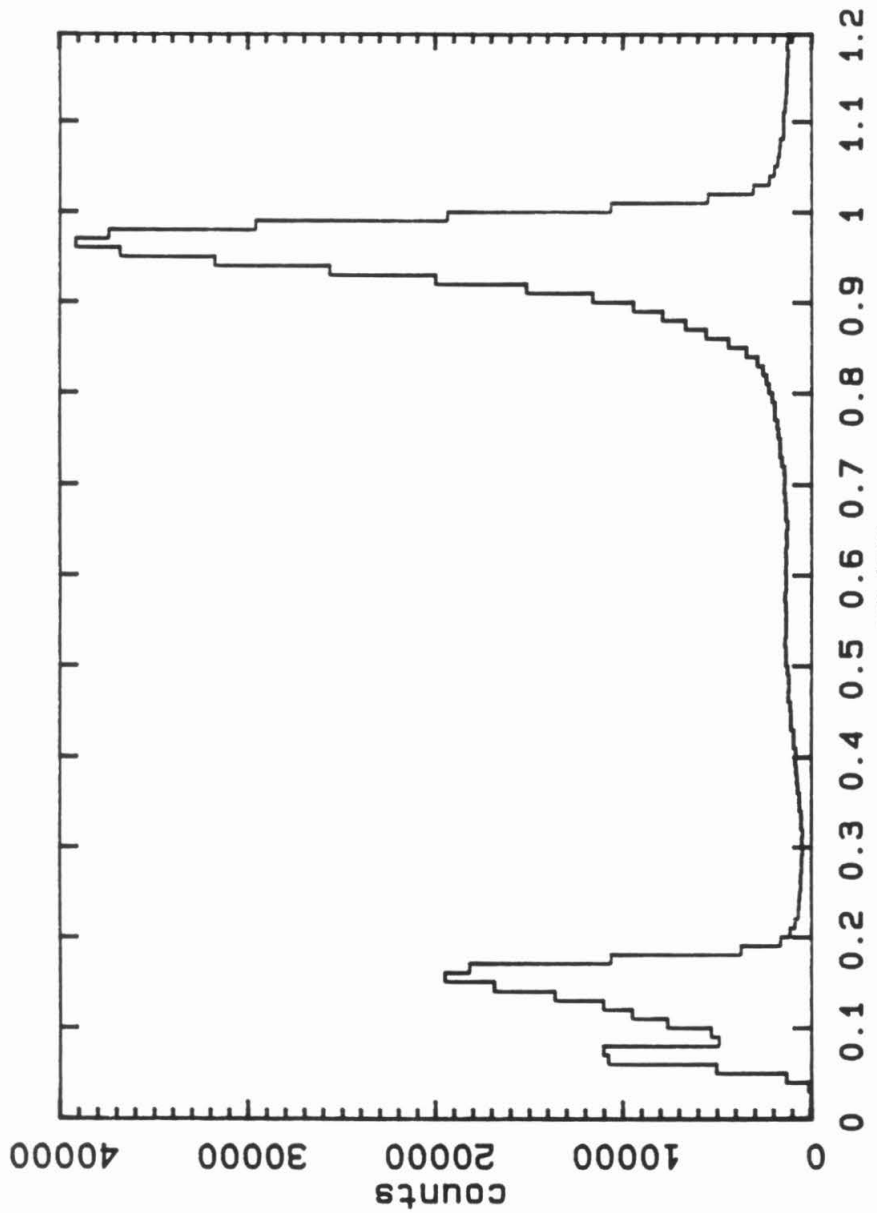

Figure 3.1 The distribution of Z_C/Z_I for particles in the Gold data set. Particles were selected to have Z_C/Z_I between 0.9 and 1.08

particles in the 1.2-2 GeV/amu region, together with those above 5 GeV/amu, where the Čerenkov signal is saturated but the ionization signal is in the relativistic rise region. Below $Z_C/Z_I = 0.83$, there is a wide plateau, corresponding to particles which are above the Čerenkov threshold at ~300 MeV/amu, but below 1.2 GeV/amu.

The peak at $Z_C/Z_I \cong 0.17$ corresponds to the scintillation region, in which the particles are below the Čerenkov threshold. Both Z_C and Z_I have a weak energy dependence in this region, and hence the pileup of particles in the peak. This peak is larger than would be expected from the particle energy spectrum. The reason is that Fe nuclei in the scintillation region have Z_I greater than 30.5, and thus were saved as "high Z", rather than being subjected to the 1/40 "lucky" selection. The lowest peak in the Z_C/Z_I distribution corresponds to noise at the Čerenkov discriminator threshold.

Figure 3.2 shows histograms of Z_C/Z_I in the range 0.90 to 1.08 for various intervals of Z_C. The shapes of the peaks at high Z are quite similar to the shape of the iron peak, and the peak position is independent of Z up to the charge 50-60 region, with only a small shift beyond that. From this we conclude that both Z_C and Z_I scale with Z in a very similar way. In the distribution of Z_C/Z_I shown in Figure 3.1, there is a plateau to the right of the peak. This plateau is caused by particles which have inconsistencies within the individual ion chamber signals, or within the individual Čerenkov signals. Particles having such inconsistencies were removed with cuts to be described later, and the histograms of Figure 3.2 were made after these cuts had been applied.

The iron peak in Figure 3.2 has a full width at half maximum of 6.2% of the peak value. From Table 2.1, the fwhm of a single ion chamber is expected to be ~11% for iron nuclei; adding the signals from two modules and taking the square root yields a fwhm of 3.9% for Z_I. Combining this with the rms resolution of Z_C of 0.338 charge units (to be obtained later in this chapter) implies that the fwhm of Z_C/Z_I for a monoenergetic beam will be 4.9%. From this we conclude that the Z_C/Z_I peak is significantly broadened by the instrument resolution. As a result of this broadening, the distributions of Figure 3.2 are

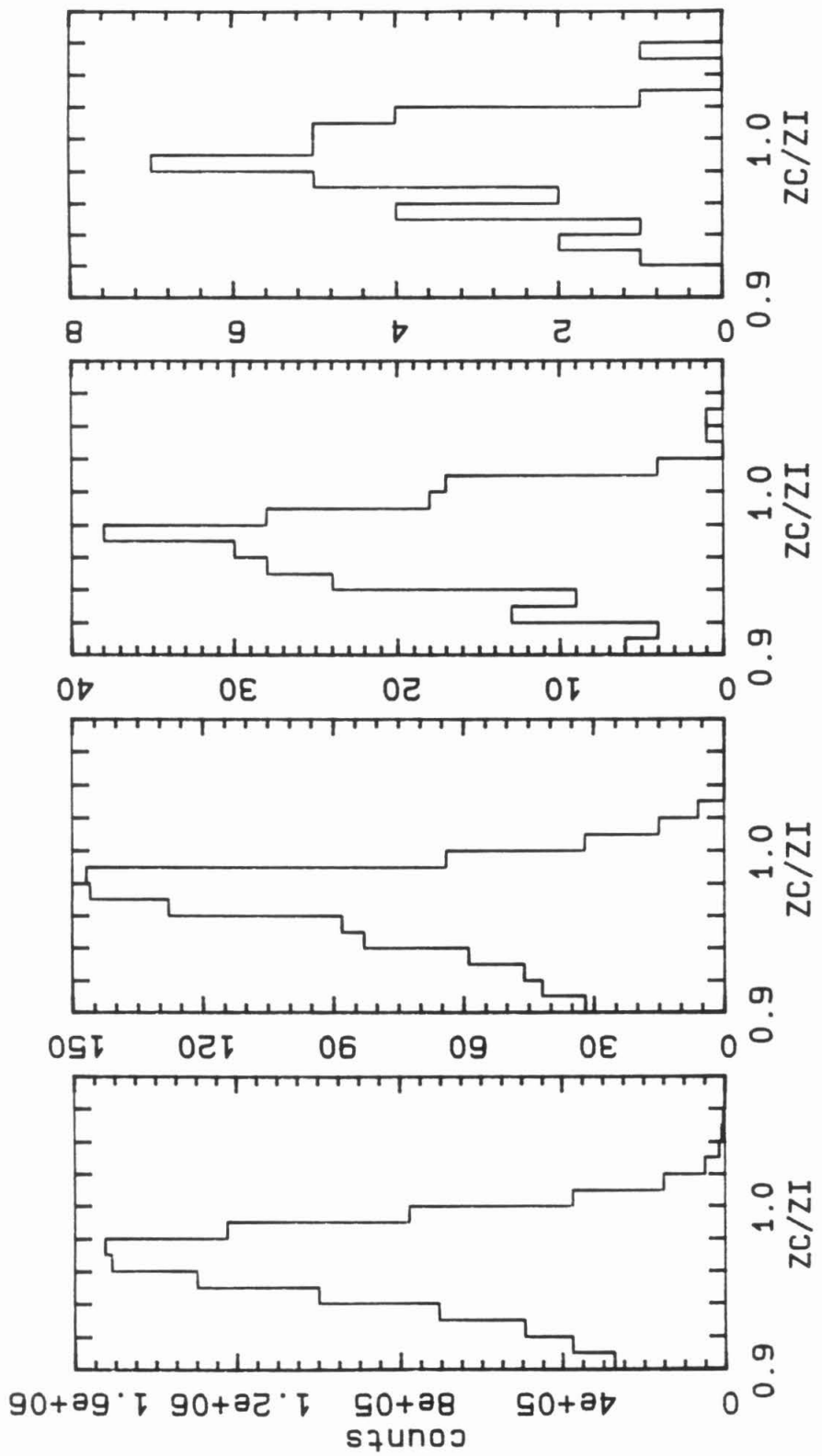

Figure 3.2 Z_C/Z_I distributions of particles in various Z_C intervals, from left to right: 23-27, 33-39, 47-61, and Z_C>74.5. Particles were weighted as described in Section 3.2.6.

less useful for studying the energy spectrum than they might otherwise be. The double valued ionization response further complicates such a study, since particles both above and below minimum ionizing lie to the left of the peak. The width of all the distributions in Figure 3.2 is approximately the same; this is a consequence of the energy dependences of Z_C and Z_I and the observation in Chapter 2 that the ion chamber resolution is a constant fraction of the signal, to first order.

Particles were selected to have similar values of Z_C and Z_I, as follows:

1) Particles with $Z_C / Z_I < 0.9$ were eliminated. Most of these particles have kinetic energy $\lesssim 1.5$ GeV/amu. At such low energies the relative values of the Čerenkov signal and the signals from the two ion chamber modules have strong energy, angle, and charge dependences, resulting from the large energy losses in the detector materials. Including these very low energy particles would complicate the analysis. The $Z_C / Z_I \geq 0.9$ requirement also excludes a few particles with kinetic energy $\gtrsim 80$ GeV/amu. 44.1 % of the remaining particles were eliminated by this cut, leaving 339,142.

2) A particle with $Z_C / Z_I > 1.08$ has an anomalously high Čerenkov signal caused by an accidentally coincident particle striking the window of a photomultiplier tube. The Čerenkov light produced in the window is observed by the other tubes as well, increasing the effect. This cut eliminates 13.0 % of the remaining particles, leaving 295,170.

3.2.3. The Hodoscope Cut

Many events have hodoscope patterns in which more wires were triggered than expected from geometry. The hodoscope readouts provide trigger information for patterns up to 16 wires wide, together with an overflow bit. In order to eliminate particles whose trajectory may be grossly incorrect, a pattern width selection was made. A given hodoscope plane is considered to be "good" if the pattern is no more than eight wires wide in each coordinate, and in order to be accepted for analysis, a particle must have at least two good

planes. Although this cut is loose, the selected events with wide patterns show good charge resolution, and the distribution of Z_C is insensitive to variations in the allowed pattern widths. This cut eliminates 0.8 % of the remaining particles, leaving 292,936.

3.2.4. Ion Chamber Consistency Cuts

An individual ion chamber may have an anomalously high signal because of an accidental coincidence with a second particle crossing the chamber at a large angle to the instrument axis. To eliminate these events, we define the quantities dz123 and dz456:

$$dz123 = 1+100\times\left[\frac{1}{2}\left(\frac{I_1-I_2}{I_{123}}\right)^2+\frac{1}{2}\left(\frac{I_2-I_3}{I_{123}}\right)^2\right]^{1/2} \qquad (3.1)$$

where I_{123} is the mean of the three ion chamber signals I_1, I_2, and I_3 in one module, and dz456 is similarly defined for the other module. If one of the three signals is unusually large then the value of dz123 will be correspondingly large. For those particles with only two good ion chambers in a module, only one term was used in (3.1), and dz123 was set to 1 for particles with only one good chamber.

Figure 3.3 shows the distribution of dz123 observed in flight. This distribution has a long tail resulting from accidental coincidences and fragmentations within the gas and the electrodes. The main peak lies at a value of 3.5, thus implying an rms width of ~11% for each chamber individually. The distribution of dz456 is similar. Most contaminated events were eliminated by requiring the values of dz123 and dz456 to be less than 16. This cut was chosen at the transition from the near-gaussian peak to the non-gaussian tail. The dz123 and dz456 cuts remove 4.9 % of the remaining particles, leaving 278,671.

To remove events in which a fragmentation interaction occurred within the Čerenkov detector, we can define the quantity dzfa = $Z_{I,123}$ - $Z_{I,456}$, where $Z_{I,123}$ is the value of Z_I calculated for the 123 module only. The first Bevalac calibration showed that to a good approximation the ion chamber resolution is

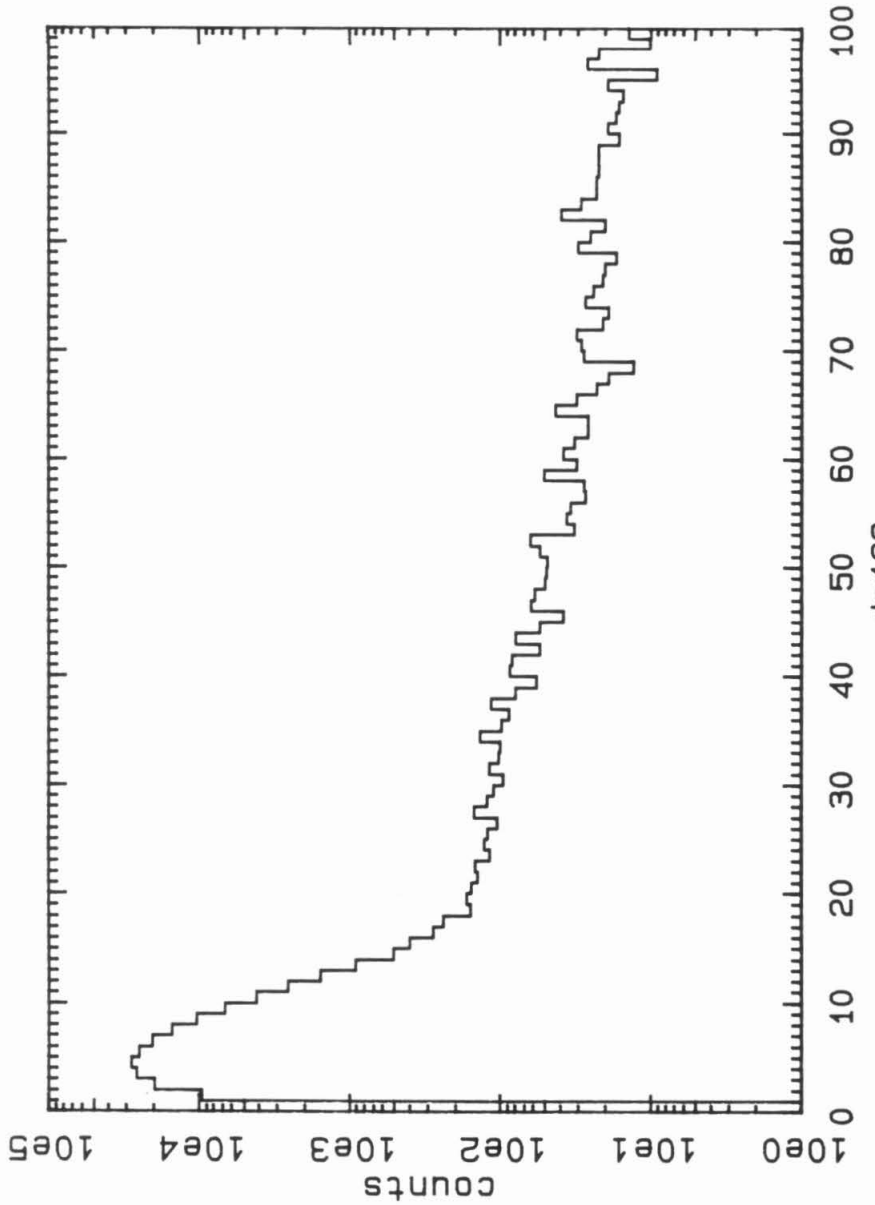

Figure 3.3 The distribution of the ion chamber consistency parameter dz123, defined in the text. Particles were required to have dz123 less than 16.

a constant fraction of the signal and independent of Z, hence dzfa/Z_I should have a distribution independent of Z. Figure 3.4 shows the values of dzfa/Z_I with cuts at ± 0.1 being sufficient to eliminate the long tails from interactions. These cuts eliminated 7.7% of the remaining particles, leaving 257,088.

3.2.5. The Čerenkov Consistency Cut

If all particles passed through the detector at normal incidence, then the total Čerenkov light would split between the eight tubes in fractions which depend only on the trajectory position (x,z) in the plane of the radiators. In order to check the light distribution, we have used the parameter relct, defined as follows (Garrard, 1984):

$$\text{relct} = 1+100\times\left\{\left[\frac{(C_2+C_6)/(C_3+C_7)}{\text{ratiomap}(x,z)}-1\right]^2+\left[\frac{(C_1+C_5)/(C_4+C_8)}{\text{ratiomap}(x,z)}-1\right]^2\right\}^{\frac{1}{2}} \quad (3.2)$$

where C_i and C_{i+4} are the signals from a pair of tubes in a particular corner, the ratios are to the pair in the diagonally opposite corner, and ratiomap(x,z) is the average value of these ratios. Thus relct is a measure of the deviations of these ratios from their expected values.

Because the ratio maps were made using particles arriving near normal incidence, the distribution of relct is angle dependent. To investigate the angle dependence, the data were binned by angle of incidence and the relct distributions compared. The value of relct at the half maximum point was found to vary smoothly from 12 to 19 as the angle increased fom 0° to 70°, so the raw value of relct was corrected by the factors shown in Table 3.1. Figure 3.5 shows the distribution of the corrected value of relct. This distribution shows a narrow peak at low values and a flat tail at high values.

The relct cut was chosen so that particles were rejected if their corrected value of relct was greater than 14. To see how such a value might arise, consider a particle passing through the center of the Čerenkov plane, where the signals from the eight tubes should be approximately equal. Now suppose that the signal from one tube is raised by an amount Δ from its expected value. From (3.2), we have

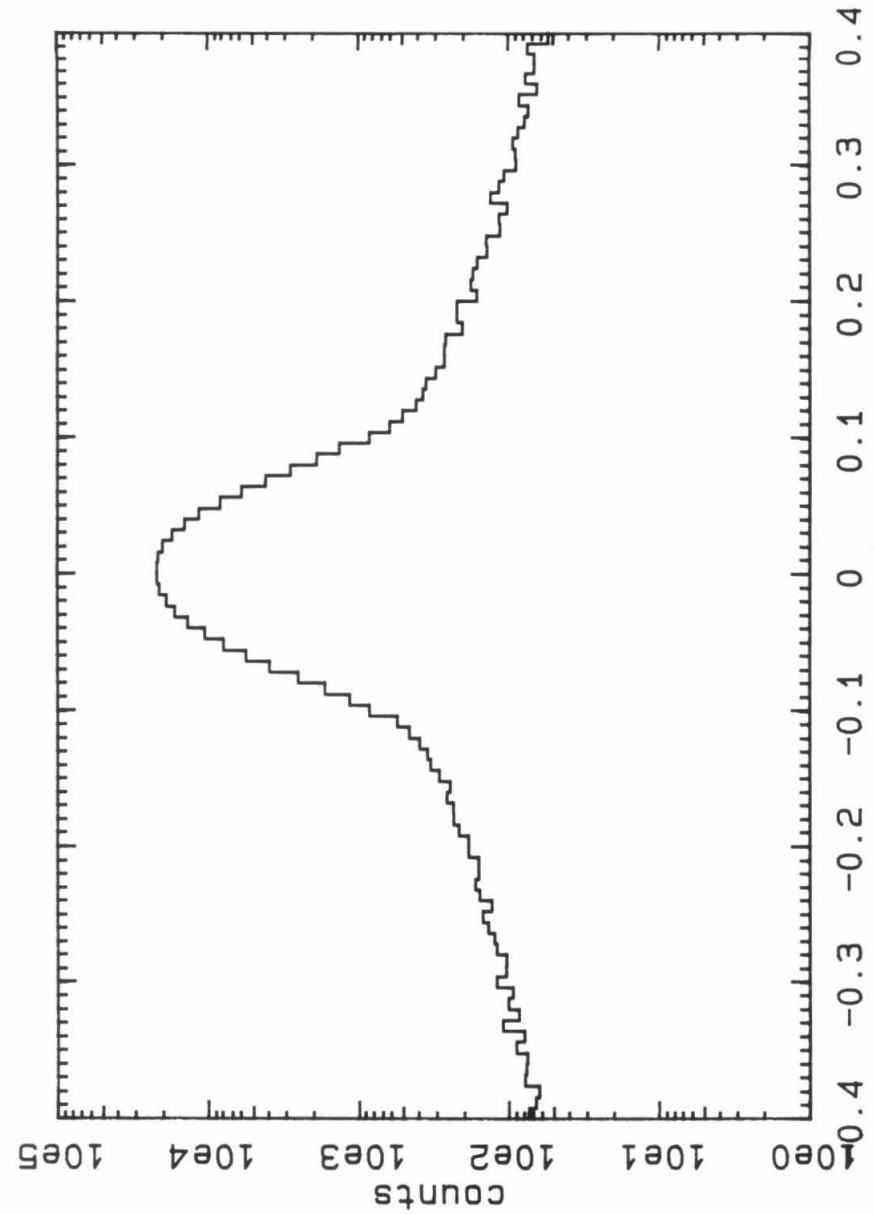

Figure 3.4 The distribution of $dzfa/Z_I$, defined in the text. Particles were required to have $-0.1<dzfa/Z_I<0.1$.

Table 3.1	
angle	correction factor
0° - 20°	1.000
20° - 40°	0.923
40° - 50°	0.857
50° - 60°	0.750
over 60°	0.632

Table 3.1 Factors applied to relct to correct for the variation of the distribution width with angle of incidence.

$$relct \approx 1+50\frac{\Delta}{C} \tag{3.3}$$

where C is the signal from one tube. Then a relct of 14 implies that $\Delta/C = 0.26$, and the fractional increase in the total Čerenkov signal is $\Delta/8C = 0.033$. At Z = 50, this corresponds to a maximimum error of 0.8 charge units in Z_C, about twice the intrinsic resolution. Thus the inclusion of particles with values of relct as high as 14 does not severely compromise the charge resolution. The relct cut eliminated 5.0 % of the remaining particles, leaving 244,221. These are the particles used for the abundance analysis to be given in Section 3.4.

3.2.6. Livetime Weighting

Each major frame of the data stream from the experiment contains up to 128 events and represents 40.96 seconds of exposure. Events were recorded with either normal or priority status depending on the ion chamber pulse heights and the presence of a Čerenkov discriminator signal. The signal levels required were such that any particle with Z > 33 and a Čerenkov signal above threshold was given priority status while most Fe nuclei were classed as normal. A priority event was able to overwrite a normal event in the data buffer,

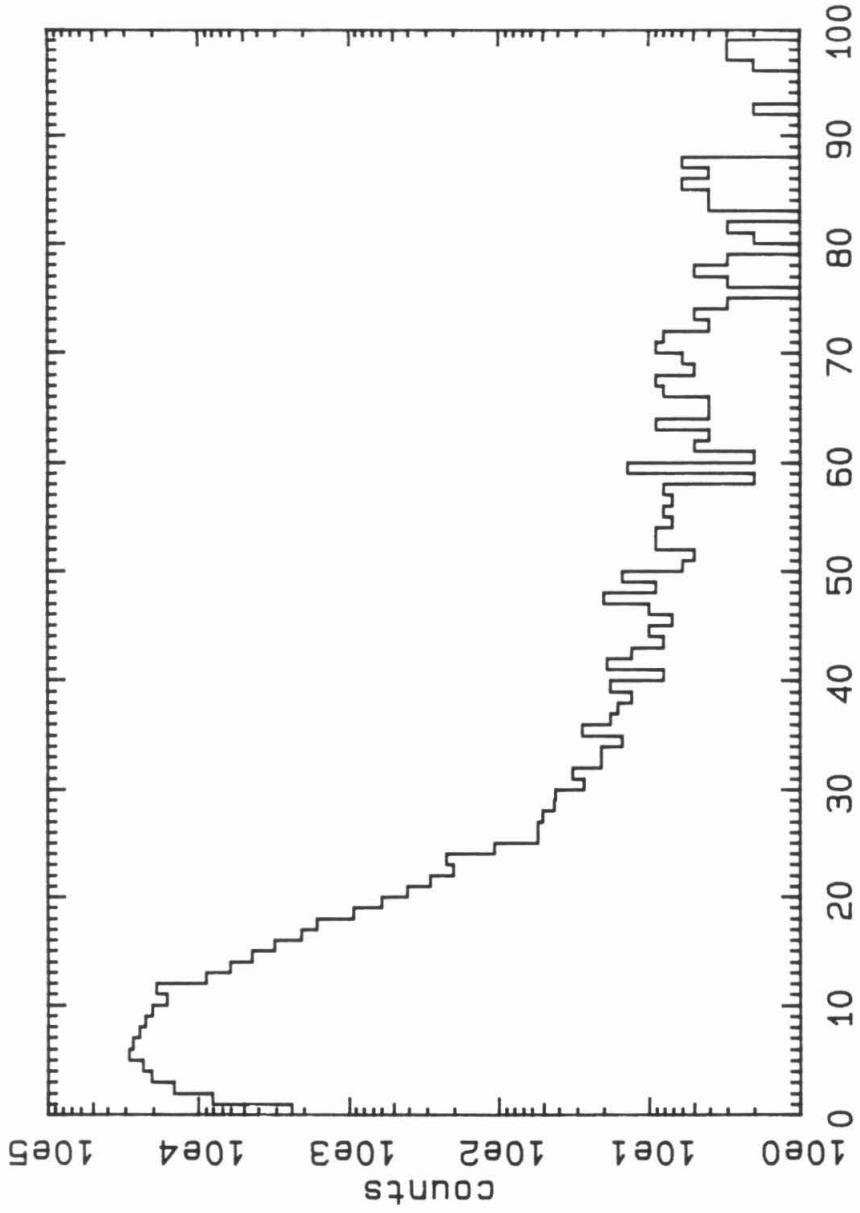

Figure 3.5 The distribution of the Čerenkov consistency parameter relct, after the angle correction described in the text. Particles with relct > 14 were rejected.

thus giving different livetimes for the two types of events during periods of high event rates. A more complete discussion of the event control logic and data readout systems is given in Binns et al., (1981).

Each normal event is assigned a statistical weight equal to the number of normal events triggering the instrument within its major frame, divided by the number of normal events actually recorded in that major frame, and thus correcting for the recording inefficiency of normal events relative to priority events. The livetime weight of priority events is 1. The total weight of the selected data set is 401914.3, implying a mean livetime weight per particle of 1.65.

The weights of those particles which were lucky but not high Z were further increased by a factor of 40 to compensate for their selection bias. With this factor applied the total weight of the selected data set is 13,911,805. This is the estimated number of particles which traversed the instrument and would have met the selection criteria if all events had been recorded at the same efficiency as priority events.

3.3. The Rigidity Spectrum

Chapter 1 describes the various rigidity dependent processes thought to occur between the cosmic ray source and a detector placed in Earth orbit. The relative abundances of primary and secondary elements depend on the particular rigidity at which propagation occurred and these effects must be properly accounted for when comparing the observed abundances with those predicted by propagation models. Here we derive the rigidity spectrum of particles arriving at the detector after the exclusion of many low rigidity particles by the geomagnetic field. Because the HNE detector provided no direct indication of particle rigidity, an indirect method was required.

During the first pass analysis, particles were assigned cutoff rigidities for each of the two possible directions, as described in Section 3.1.1. These cutoffs are the lowest possible rigidities for particles from those directions. Using the same selections as before, but without the lower Z_C/Z_I limit, a

histogram of cutoffs was generated as follows:

1) Particles with zenith angle less than 35° are known to have come from above the horizon and the appropriate cutoff was used.

2) For the remaining particles the direction ambiguity cannot be resolved, however it is more likely that they came from the direction of the lower cutoff. By assuming a particular interplanetary spectrum we can weight the two cutoffs by their probabilities. If N(R) is the flux of particles of rigidity R or more in interplanetary space, then the probability that the higher of the two cutoffs is correct is

$$f = \frac{N(R_{max})}{N(R_{min})+N(R_{max})} \tag{3.4}$$

where R_{min} and R_{max} are the two cutoffs. The interplanetary spectrum N(R) was approximated by a piecewise power law, using values tabulated at Washington University (S.D. Barthelmy and M.D. Jones, private communication), which in turn were derived from the compilation of iron spectra presented by Webber (1982). The piecewise power law is given by:

$$N(R) = \begin{cases} R^{-1.7} & \text{if } R>300 \text{ GV} \\ 0.56229\, R^{-1.587} - 4.3792\times10^{-6} & \text{if } 27 \text{ GV} <R\leq 300 \text{ GV} \\ 0.13376\, R^{-1.016} - 1.6953\times10^{-3} & \text{if } 8.3 \text{ GV} <R\leq 27 \text{ GV} \\ 0.10017\, R^{-0.710} - 8.4102\times10^{-3} & \text{if } R\leq 8.3 \text{ GV} \end{cases} \tag{3.5}$$

This approximation was chosen to fit the lowest observed fluxes at the lower rigidities, since the HNE was operating during solar maximum, when the solar modulation is greatest.

The higher cutoff was weighted by f, and the lower by (1-f); the resulting histogram is shown in Figure 3.6. Each bin in Figure 3.6 contains particles with rigidity greater than or equal to the lowest cutoff in that bin. If n_i is the number of particles in a particular bin of Figure 3.6, and R_i is the mean cutoff in that bin, then the number of particles in that bin whose actual rigidities lies between R_1 and R_2, with $R_i<R_1<R_2$, is given by

$$m_i(R_1,R_2) = \frac{N(R_1)-N(R_2)}{N(R_i)}\, n_i \,. \tag{3.6}$$

The total number of particles in the rigidity interval $[R_1,R_2]$ is then given by $\sum m_i$, where the sum is over all of the bins having $R_1<R_2$ in Figure 3.6. Figure 3.7 shows the result of this deconvolution, using the same interplanetary spectrum as before. The lower energy limit of the particles selected for abundance analysis is ~1.5 GeV/amu, which corresponds to a rigidity of order 5 GV.

The propagations to be discussed in Chapter 4 use ten rigidity intervals, chosen so that each interval contains an equal number of particles in a differential rigidity spectrum proportional to R^{-2}. Table 3.2 lists these rigidity intervals, together with the fraction of particles observed in each interval at the detector. The Z_C/Z_I cut at 0.9 imposes an upper rigidity limit of about 170 GV on the data. however only about 1 % of the particles are eliminated by this cut. The resulting error is small compared to the uncertainties in the propagations.

3.4. Elemental Abundance Analysis

3.4.1. Overview

In the following analysis, Z_C has been used as the charge estimator for all particles. This is because the ion chamber resolution has been observed to be an approximately constant fraction of the signal, as discussed in Chapter 2. From Table 2.1, the signals from each ion chamber module have a full width at half maximum of ~11%. Approximating the resolution function by a gaussian leads to rms widths in Z_I of 0.43 charge units at Fe and 1.36 charge units at Pb, which is insufficient to distinguish adjacent elements. The Čerenkov resolution at Fe is ~0.34 charge units and is nearly constant with Z, as will be shown in a later section.

Figure 3.8 is a histogram of the distribution of Z_C, in bins of 0.25 charge units, and covering the entire range from Z_C = 20 to Z_C = 90. Each particle was livetime weighted as described above, and as expected this plot shows the large fall in abundances from iron to the elements in the mid-30's: from $_{26}$Fe to $_{34}$Se the abundances fall more than four orders of magnitude, with a futher

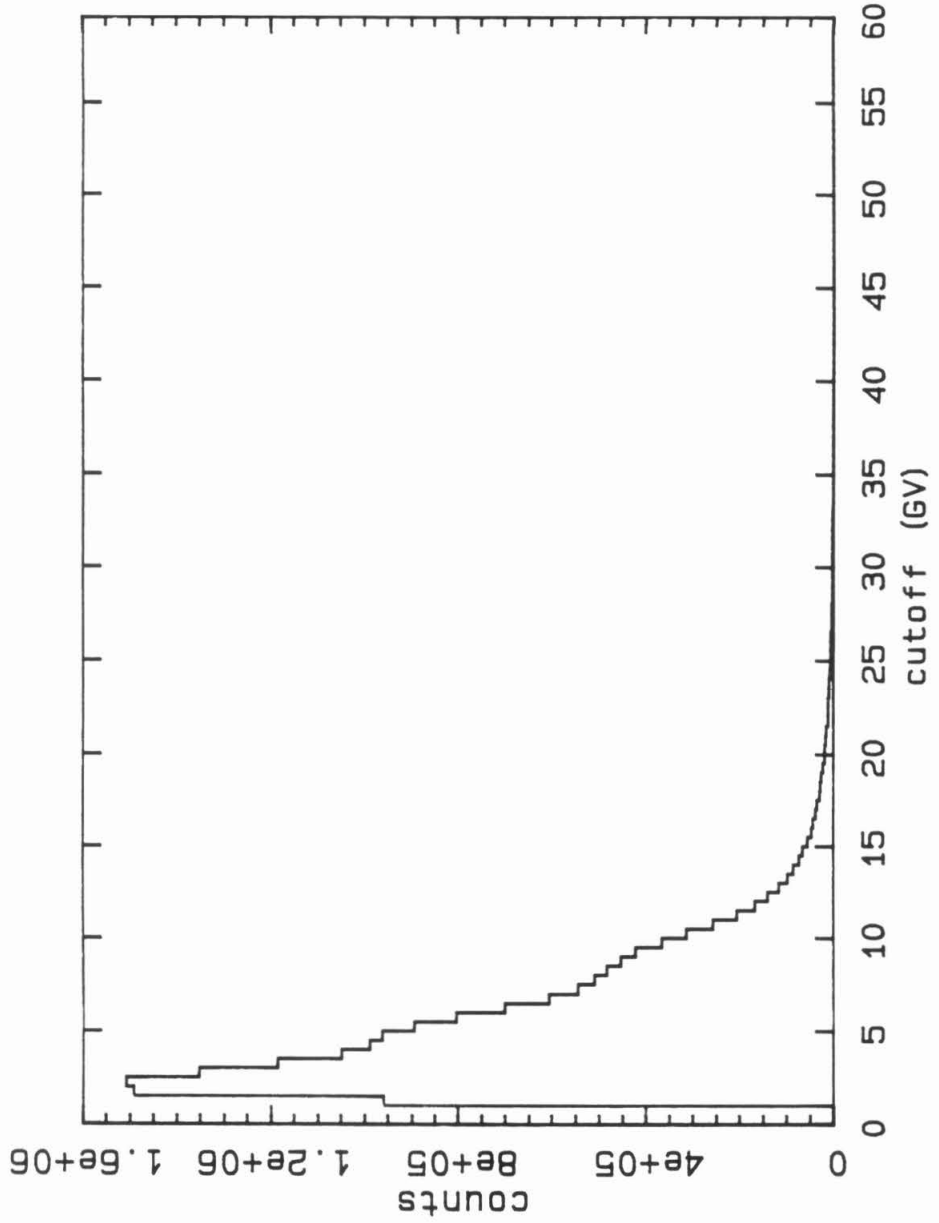

Figure 3.6 The distribution of geomagnetic cutoffs assigned to each particle, with weight factors as described in the text.

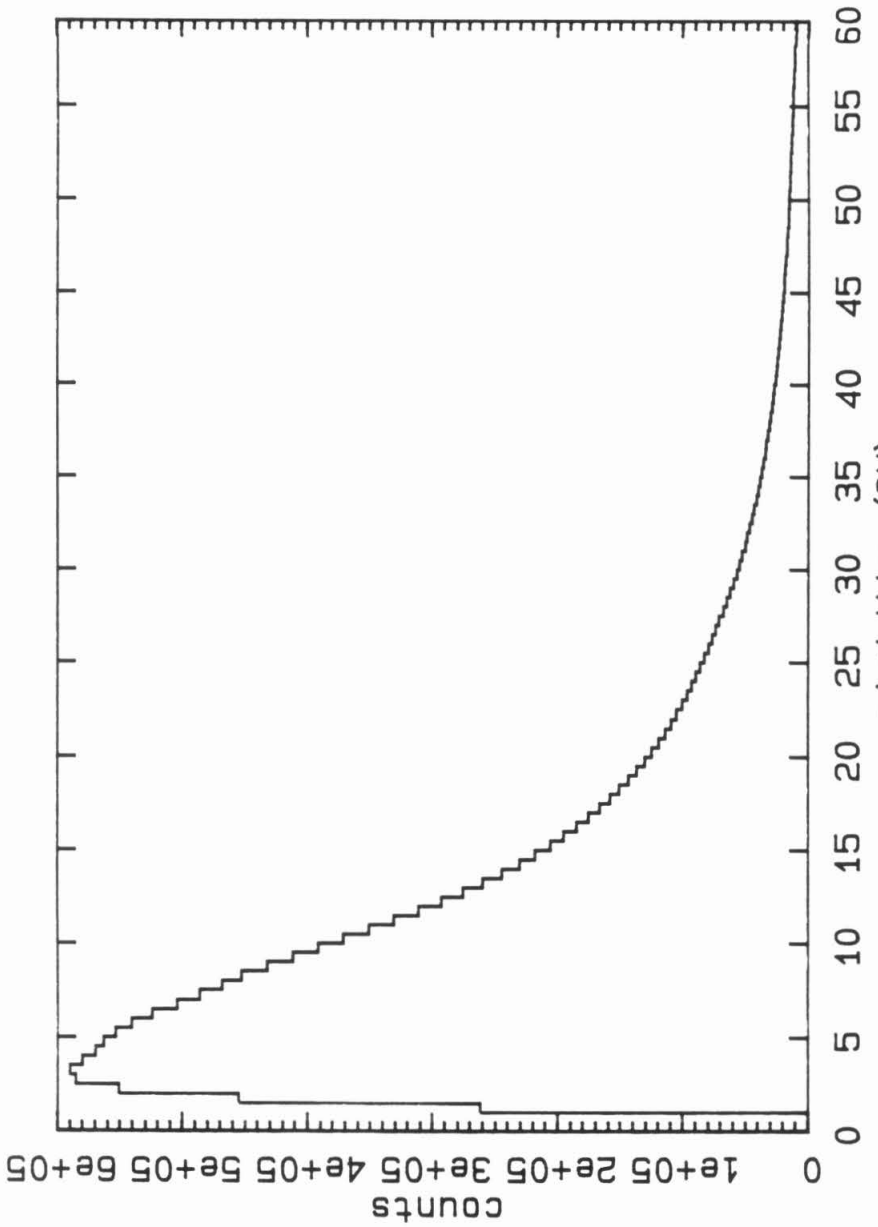

Figure 3.7 The rigidity spectrum of particles arriving at the detector, inferred from the cutoff distribution as described in the text.

Table 3.2		
Interval	Limits (GV)	fraction of total
1	5.000-5.556	0.0493
2	5.556-6.250	0.0568
3	6.250-7.143	0.0705
4	7.143-8.333	0.0857
5	8.333-10.00	0.1064
6	10.00-12.50	0.1271
7	12.50-16.67	0.1436
8	16.67-25.00	0.1538
9	25.00-50.00	0.1379
10	50.00-∞	0.0688

Table 3.2 The rigidity distribution of the observed particles, in bins having equal widths in an R^{-2} spectrum.

factor of 5 drop into the charge 40-60 region and beyond. Figure 3.8 also shows many individual element peaks, which will be examined in greater detail in the following sections.

3.4.2. Abundance Fitting

Elemental abundances may be obtained from the histogram of Figure 3.8 by using the Maximum Likelihood fitting technique, with Poisson statistics for the count in each bin. This technique is preferred over the more common Least Squares technique (i.e., Maximum Likelihood with Gaussian statistics) because it correctly treats the bins with low counts and generally preserves the area under the fitted distribution (Baker and Cousins, 1984).

For a Poisson distribution,

$$l(\mu|n) = \frac{\mu^n e^{-\mu}}{n!} \qquad (3.7)$$

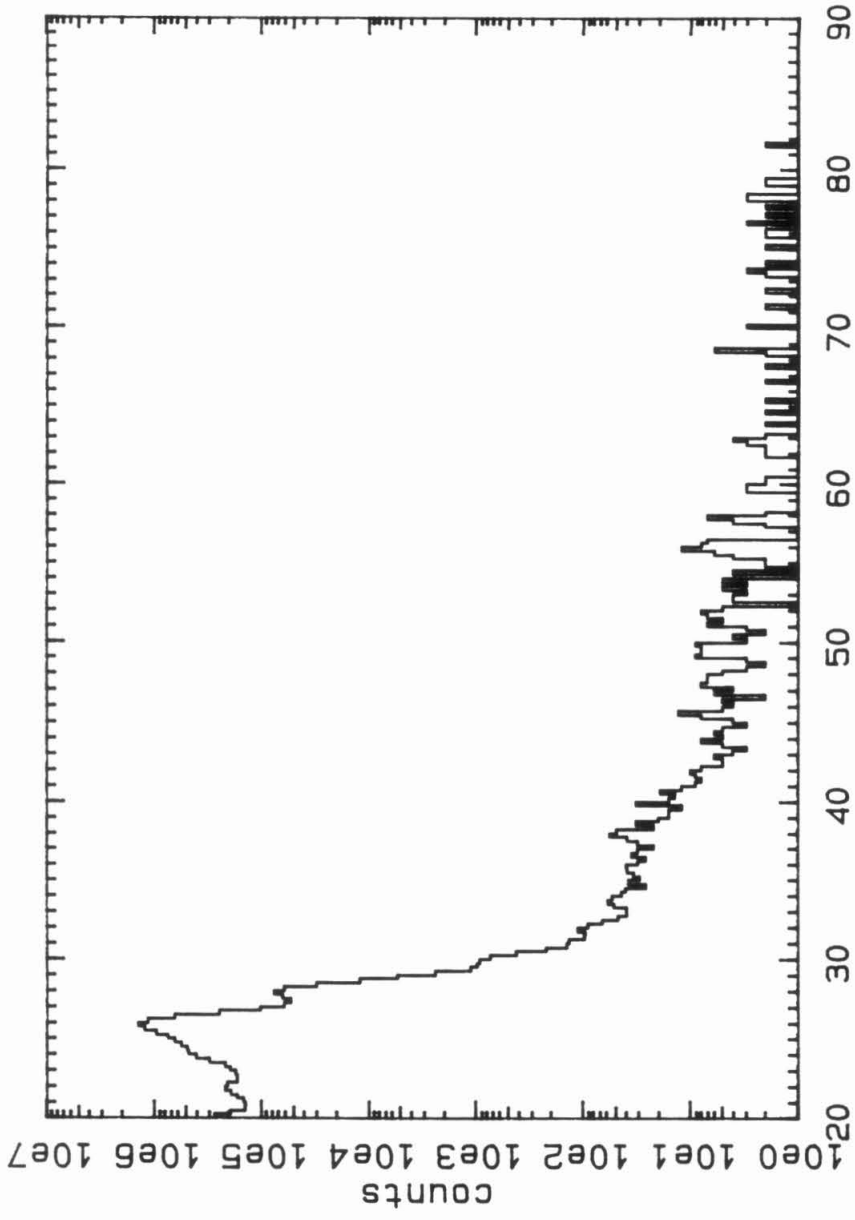

Figure 3.8 The distribution of Z_C of the selected particles, from Z_C=20 to 90. The weighting procedure of Section 3.2.6 has been applied to each particle in order to show the true abundance distribution. There were no selected particles with Z_C greater than 84.

is the likelihood of μ being the mean of the parent distribution where n is the observed count. For a histogram with N bins, the likelihood function is given by

$$L = \prod_{i=0}^{N} l_i(\mu_i | n_i) \tag{3.8}$$

where μ_i is the expected number of particles in a bin. The parameters controlling the values of the μ_i may then be adjusted to maximize the value of L. For ease of computation, the logarithm of the likelihood may be maximized, rather than the function itself.

Assuming that the resolution function is gaussian, the μ_i are given in general by

$$\mu_i = \int_{Z_{C,i}}^{Z_{C,i+1}} dZ_C \int_{Z_C'(E_{min})}^{Z_C'(E_{max})} dZ_C' \sum_Z \frac{dN_Z}{dE}(E(Z_C')) \frac{1}{\sqrt{2\pi}\sigma} \exp\left[-\frac{1}{2}\left[\frac{Z_C - Z_C'}{\sigma}\right]^2\right] \tag{3.9}$$

where $Z_{C,i}$ and $Z_{C,i+1}$ are the bin edges, E_{min} and E_{max} are the minimum and maximum energies corresponding to the selected data, dN_Z/dE is the number of particles of charge Z per unit energy interval (i.e., the differential energy spectrum), and $\sigma(Z_C')$ is the rms resolution of the Čerenkov detector. In (3.9), the energy integral should really be somewhat more complicated than written, since the maximum and minimum energies depend on the ratio Z_C/Z_I, which in turn depends on the resolution of both the ion chambers and the Čerenkov detector. However, there are relatively few particles close to the $Z_C/Z_I = 0.9$ boundary, and any effects should be unimportant.

3.4.3. The Iron and Sub-iron Region

Figure 3.9 is a histogram of particles with Z_C in the range 20-30, using bins of 0.125 charge units. This histogram shows peaks at the even elements $_{20}$Ca, $_{22}$Ti, $_{26}$Fe, and $_{28}$Ni, as well as an indication of a peak at $_{23}$V. The Fe peak is severely skewed towards the low side owing to the presence of many low energy particles, for which the Čerenkov signal is not saturated. In order to obtain the total number of iron nuclei in the data set, this distribution fitted

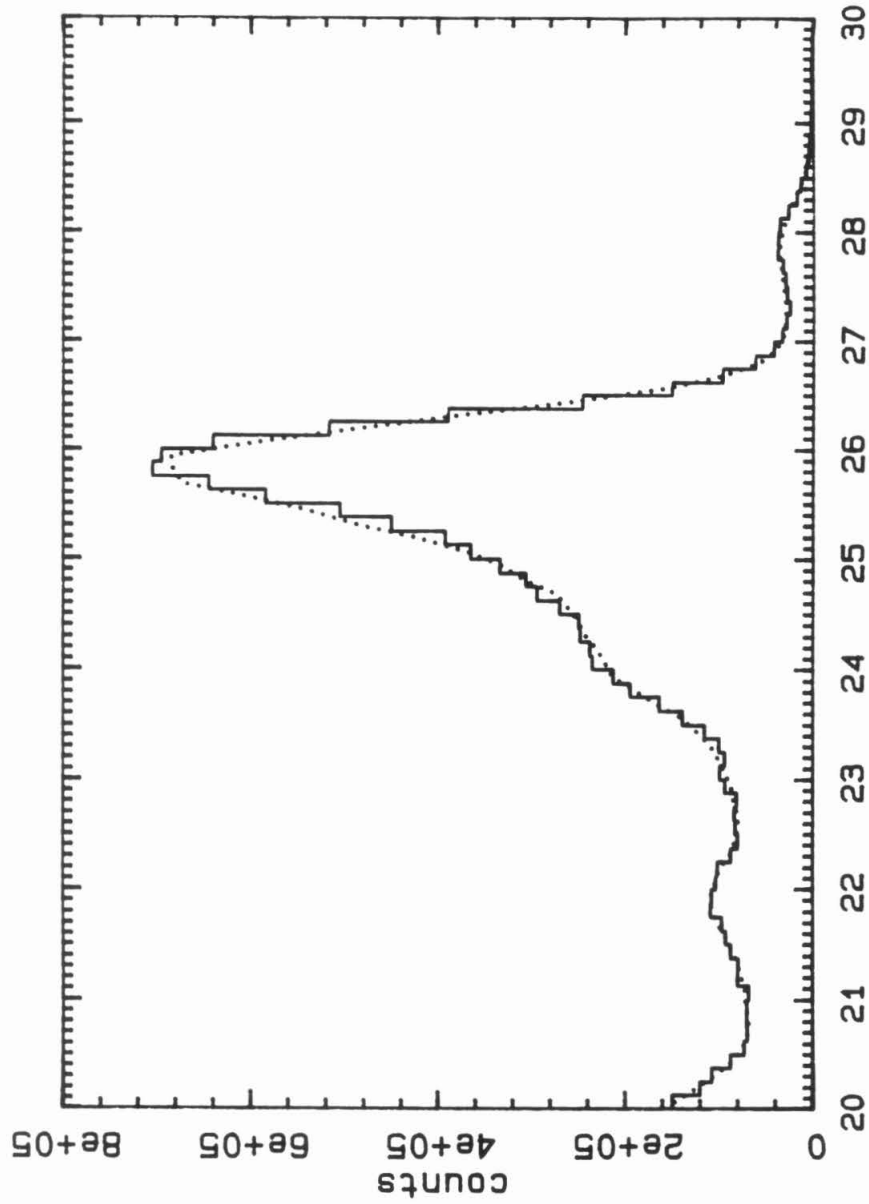

Figure 3.9 The weighted distribution of particles in the Z_C=20 to 30 region. The dotted curve shows the fitted distribution using the spectrum of Figure 3.7 and the Čerenkov response model described in the text.

with a set of model distributions for each element, based on the following assumptions:

1) Each element has the rigidity spectrum given in Figure 3.5, but with a lower limit of 5 GV (i.e., 1.57 GeV/amu for a ^{56}Fe nucleus at the top of the detector). This limit corresponds approximately to the lower energy limit of the data. The assumption that each element has the same energy spectrum is not strictly correct because the sub-iron elements have been shown to have generally steeper spectra than iron (Engelmann et al. 1983, Jones 1985, and Jones et al. 1985), however the effect on the derived Fe abundance is small.

2) The Čerenkov signal is assumed to be given by (2.6), with an additional term proportional to Z^2/β^2 to account for scintillation, and a further term calculated by Krombel (1980) in the manner of Lezniak (1976) to account for the light resulting from knockon electrons. The relative size of the knockon term is given by the model with no adjustable The knockon term is also proportional to Z^2, and accounts for 11% of the calculated light at $\beta = 1$. Its relative size is given by the model with no adjustable parameters. The size of the scintillation term was allowed to vary, and the best fit was obtained with a contribution of 3% of the total light at $\beta = 1$. The effective value of the refractive index was assumed to be 1.528, as given by Garrard (1982). The form of the scintillation term used here was found to fit the data better than the term proportional to dE/dx used in section 2.1.

3) The Čerenkov resolution function was assumed to be a gaussian with a fixed value of σ, independent of Z and β. σ is expected to be constant if the resolution is dominated by photoelectron statistics. The value of σ was varied to obtain the best fit, and a value of 0.338 charge units obtained. This figure corresponds to 2.2 photoelectrons per singly charged particle at $\beta = 1$, and is a factor 1.27 better than the ion chamber resolution at iron.

The model distribution for each element was obtained by randomly sampling 100,000 particles from the inferred rigidity spectrum at the detector, Figure 3.7, using only rigidities above 5 GV to approximate the lower energy limit of 1.5 GeV/amu. For each particle, the energy at the midplane of the Čerenkov detector was calculated after allowing for energy loss in the detector materials. The particles were all assumed to have angles of incidence of 20°; the results are not sensitive to angle in the iron region. Next, Z_C was calculated using the model outlined above and a random sample of the gaussian response function. The reference distribution is obtained by binning according to Z_C. In each iteration of the fit the elemental reference distributions were multiplied by the current value of the abundance and then summed to yield the μ_i of (3.9).

Because the mean weight per particle in Figure 3.9 is of order 50, the fluctuations in each bin are much larger than Poisson statistics would indicate. To compensate for this effect, the fit was made to the unweighted histogram corresponding to Figure 3.9, with the value of the likelihood function at each iteration being calculated after dividing each of the μ_i by the mean weight per particle in its corresponding bin. The relative abundances of each element were adjusted for the best fit, and the procedure repeated for various choices of the other parameters. As shown in Figure 3.9, the fit is a reasonable match to the observed distribution, although it appears that the true iron distribution has fewer particles on the low side of the peak than the model assumes. In turn, this suggests that the derived iron spectrum has too many particles at low rigidities. The weighted number of iron nuclei obtained with this fit is 8.00 ± 0.24 million (statistical uncertainty only).

Particles can be selected to have high geomagnetic cutoff rigidities, so that the Čerenkov signal is almost saturated and the shape of the peak dominated by the intrinsic resolution. An example of this is shown in Figure 3.10, in which a minimum cutoff of 10 GV was required, corresponding to a minimum energy of 3.8 GeV/amu. The Fe peak in Figure 3.10 is nearly symmetric, however the total number of particles selected with this cut is only 32,497, a reduction of 86.7 % from the previous data set. Rigidity cuts ranging from 5 to

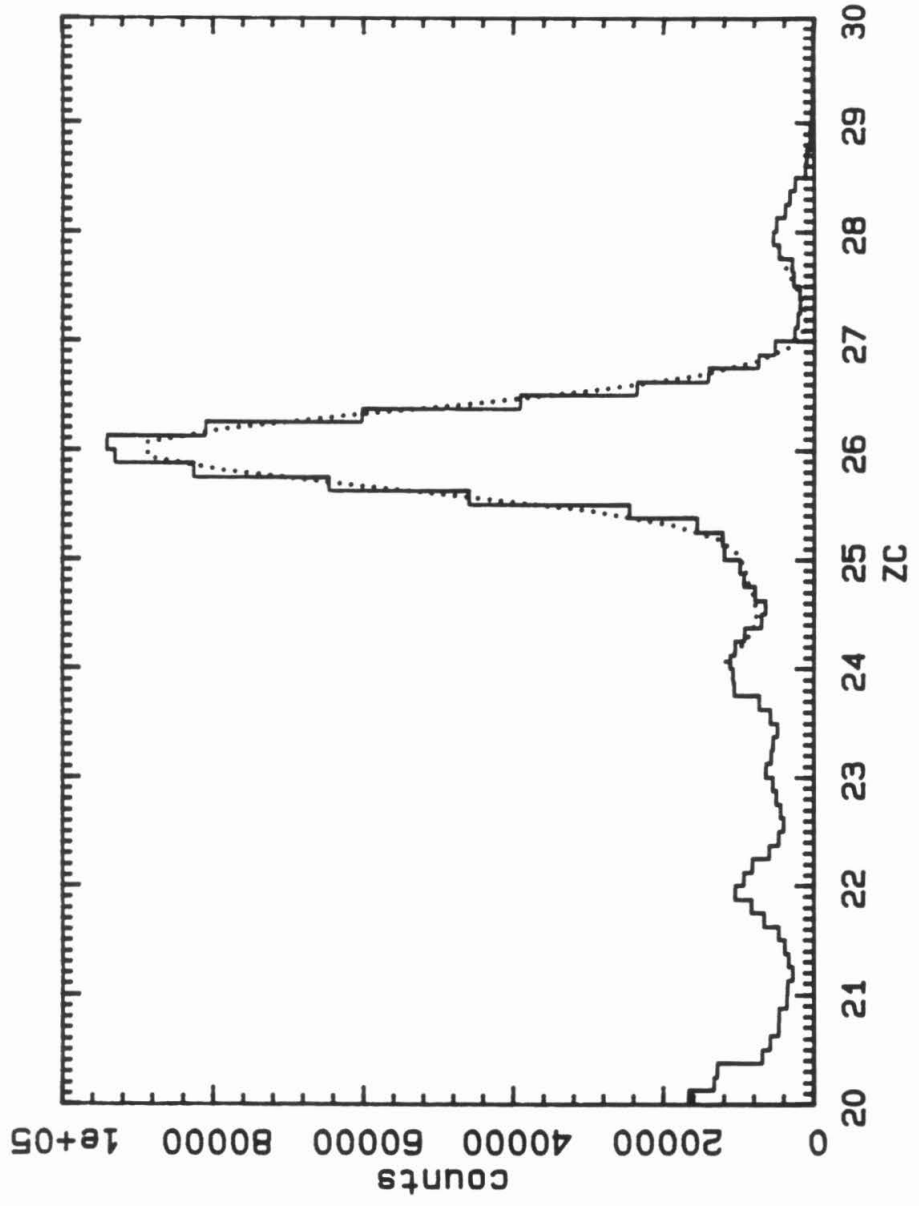

Figure 3.10 The weighted distribution of particles in the Z_C=20 to 30 region, after selection for 8 GV minimum geomagnetic cutoff. The dotted curve represents the best fit assuming gaussian peaks.

8 GV have been used in all earlier analyses of the HNE data, with the exception of the actinide analysis (Binns et al., 1982). In Figure 3.10, the fwhm of the iron peak is approximately 0.75 charge units, implying an rms resolution of 0.34 charge units, which is consistent with the value obtained above.

The dotted curve in Figure 3.10 represents a fit to the data over the range $Z_C = 24$ to $Z_C = 28$, assuming that the particles followed gaussian distributions for each element, and letting the resolution σ be a parameter, again assumed to be the same for each element. The best fit value of σ was 0.362, slightly larger than the value implied by the fwhm because the fit attempted to accommodate the asymmetry on the high side of the peak.

3.4.4. The $_{27}$Co to $_{33}$As Region

Figure 3.11 shows this region, in which the dominant feature is the rapid fall in the abundances by four orders of magnitude. Superimposed on this are peaks at the even elements $_{28}$Ni, $_{30}$Zn, and $_{32}$Ge, together with an indication of a peak at $_{31}$Ga. The elements from Z = 29 to Z = 33 inclusive are not well resolved in this data set, and fitted abundances depend critically on the form of the fitting function used. Because of this, no attempt to determine reliable abundances has been made here, although the abundance of $_{32}$Ge has been previously determined in a more restricted data set (Binns et al., 1983a). The resolution of the $_{28}$Ni peak is better than it appears in Figure 3.11 because of the logarithmic scale used.

3.4.5. The $_{34}$Se to $_{40}$Zr Region

This region is shown in Figure 3.12, where the data are now binned in 0.25 charge unit intervals. The even elements $_{34}$Se, $_{36}$Kr, $_{38}$Sr, and $_{40}$Zr appear to be resolved in this histogram, together with $_{37}$Rb. However, there is an overlap resulting from the many low energy particles present in the data set.

The upper dotted curve in Figure 3.12 represents the best fit to these data, based on the same set of assumptions that were used to fit the iron region in Figure 3.9, i.e., assuming that the Čerenkov signal scales as Z^2, that

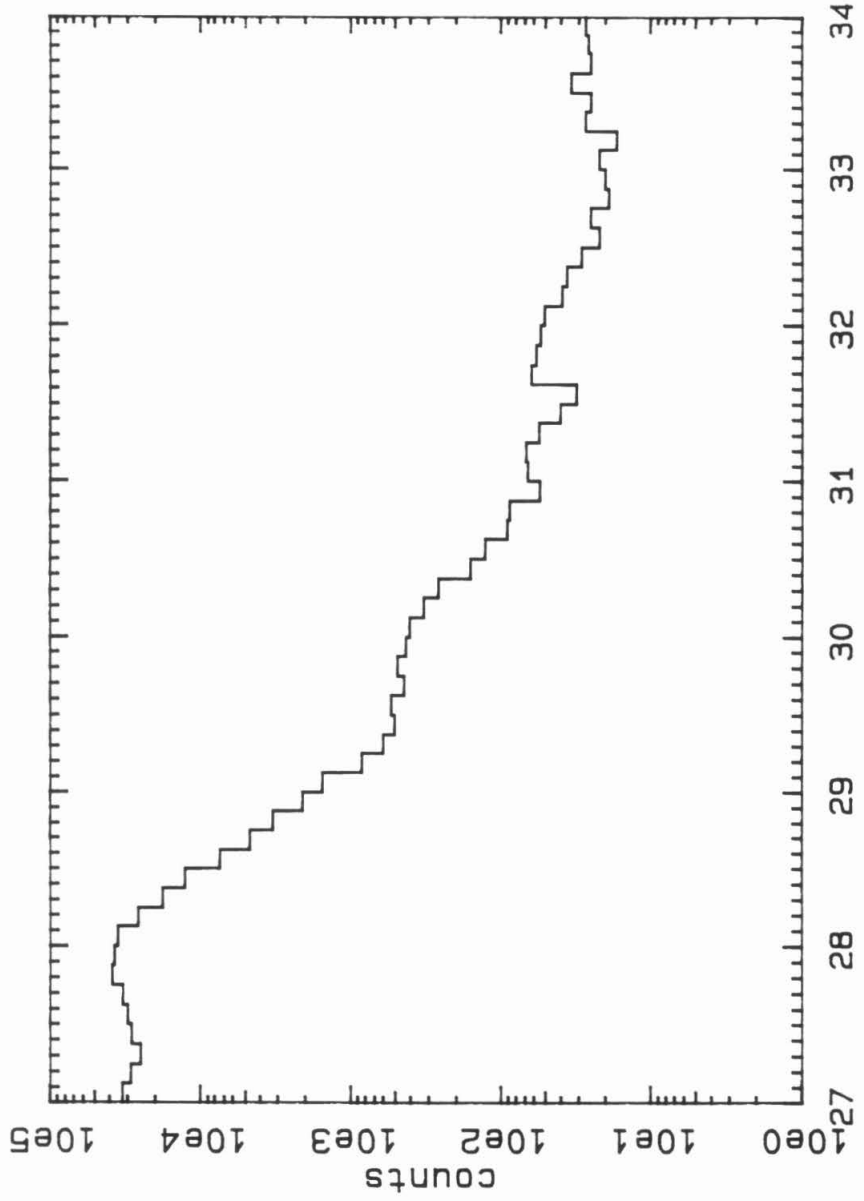

Figure 3.11 The weighted distribution of particles in the Z_C=27 to 34 region. Note that the vertical scale is logarithmic.

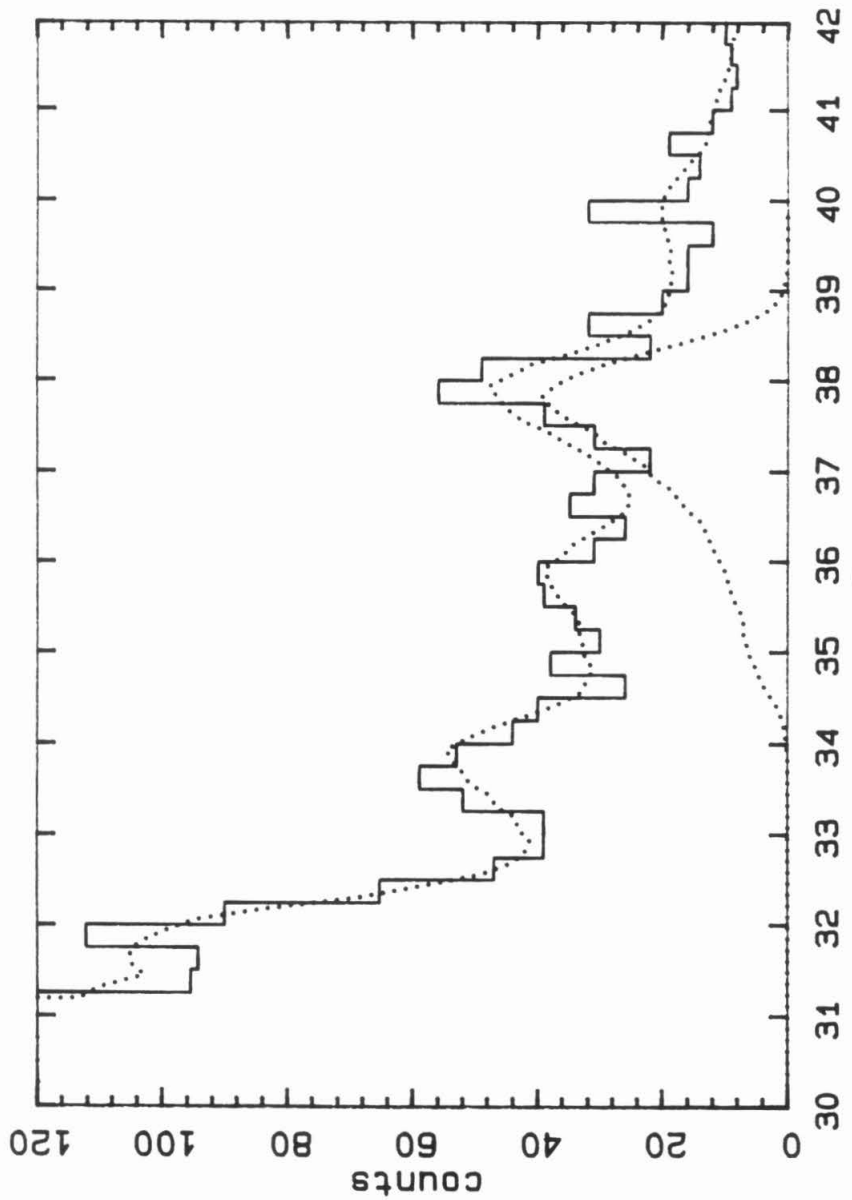

Figure 3.12 The distribution of particles in the Z_C range 31-42. The upper dotted curve represents the best fit using the iron spectrum, assuming Z^2 scaling and a constant resolution. The lower dotted curve shows the fitted contribution of $_{38}$Sr.

all elements have the same rigidity spectrum as iron, and that the resolution is independent of the signal size. The lower dotted curve represents the contribution of $_{38}$Sr to the fit function. The calculated distribution has small fluctuations resulting from the Monte Carlo method used to generate it.

In order to determine the goodness of fit, a χ^2 test may be used. For Poisson distributed data, the χ^2 test is strictly valid only as the predicted count in each bin becomes large, however, a predicted count of 5 or more is usually considered large enough (Eadie et al., 1971), and this criterion is met in Figure 3.12. Letting $Q^2 = \sum(n_i-\mu_i)^2/\mu_i$, we obtain a value of Q^2 of 38.27 for 26 degrees of freedom (36 bins less 10 fitted abundances), using only the data from Z_C = 33 to 42. From the χ^2 distribution, the probability of Q^2 being this large or larger by chance is only 7.7%. This low probability reflects the fact that the shape of the peaks does not follow the fitting function very well; in particular the $_{38}$Sr and $_{40}$Zr peaks appear to be significantly sharper than the model allows. The abundances from Z = 33 to Z = 38 resulting from this fit are given in Table 3.3. An alternative approach to fitting these data will be described in Section 3.4.8.

Table 3.3

Z	element	fitted count
33	As	86
34	Se	302
35	Br	79
36	Kr	197
37	Rb	5
38	Sr	298

Table 3.3 Fitted abundances of elements with charge 33 to 38 inclusive, obtained using the iron energy spectrum. Note that the odd elements are not resolved; see Table 3.8.

3.4.6. The $_{42}$Mo to $_{60}$Nd Region

Figure 3.13 shows this region, again using 0.25 charge unit bins. This plot shows clear peaks at every even element from $_{42}$Mo to $_{60}$Nd, with the possible exception of $_{54}$Xe. This resolution was entirely unexpected given the large spread of pulse heights resulting from the expected energy spread of the particles, as shown by the lower dotted curve, which represents the expected distribution of the $_{50}$Sn nuclei if their spectrum was the same as iron. The upper dotted curve represents the fit resulting from this model, and it is clearly unable to reproduce the shape of the distribution. Using the data from Z_C = 42 to 62 (so as to avoid the overlap with the previous histogram) and the fitted abundances of elements 42 to 62, the value of Q^2 is 22.36, with 7 degrees of freedom. The probability of obtaining a value of Q^2 this high or higher by chance is 0.2 %, confirming that the data are poorly fit by the model.

Inspection of Figure 3.13 shows that the data have a much greater peak to valley ratio than predicted by the model. The absence of a strong peak to valley ratio in the model results from the large number of low energy particles, for which the Čerenkov signal is unsaturated. Thus a possible explanation for the sharp peaks in the data is that in this charge range there are fewer low energy particles present, compared to iron. An alternative explanation is that the energy dependence of the Čerenkov signal is very different to that assumed, at least above 1.5 GeV/amu. However, below 1.0 GeV/amu the calibration described in Section 2.4 suggests that the response agrees well with the simple model. In addition, a Z dependent change in the shape of the Čerenkov response would also be expected to result in a non-Z^2 scaling law. From the locations of the peaks in Figure 3.13 there is no evidence for a systematic deviation from Z^2 scaling, although some of the peaks in Figure 3.13 do appear to be shifted from their nominal positions, as will be discussed in Section 3.4.8. Thus the most likely explanation for the sharp peaks is that the spectra of these elements are different to those at iron.

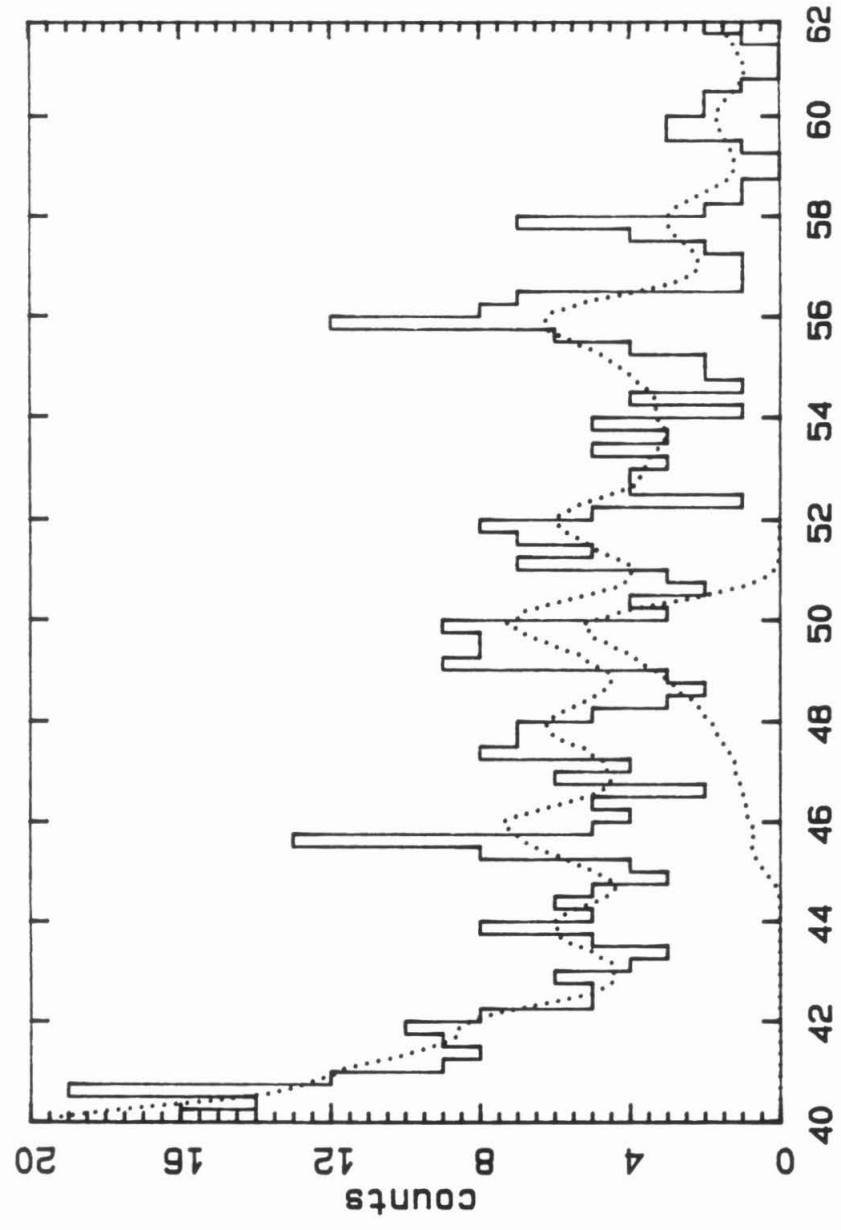

Figure 3.13 The distribution of particles from Z_C=40 to 62. The upper dotted curve is a continuation of the fit using the iron spectrum, and the lower dotted curve shows the fitted contribution of $_{50}$Sn.

3.4.7. The Z > 60 Region

Figure 3.14 shows the heaviest nuclei observed in this data set, now using bins of 0.5 charge units. The most noticeable feature of this plot is the absence of well resolved peaks. This effect may have several causes, such as a worsening resolution, a larger fraction of odd charged nuclei, or a greater number of low energy nuclei than in the 40-60 region, and these problems are compounded by the small number of particles. The data show a dip in the abundances in the $_{70}$Yb-$_{72}$Hf region, a broad peak at $_{76}$Os-$_{77}$Ir-$_{78}$Pt, and a peak at $_{82}$Pb. The width of the latter peak is ~2 charge units, suggesting that either the resolution has worsened compared to the charge 50-60 region, or that there are a larger number of low energy particles present. Additional peaks appear at $_{62}$Eu and $_{68}$Er. If these peaks are real, rather than statistical fluctuations, then they imply an upwards shift in the charge scale of ~0.5 charge units, which is not inconsistent with the position of the Pb peak.

Because of the poor statistics and absence of well defined peaks, no attempt was made to fit this region. Instead, we count the number of particles in broad charge groups, chosen for consistency with the previous study of this region by Binns et al. (1985). These groups and their counts are shown in Table 3.4.

Table 3.4

group	Z_C range	count	relative to 10^6 Fe
Light Secondary (LS)	61.5 - 69.5	48	6.00 ± 0.87
Heavy Secondary (HS)	69.5 - 73.5	15	$1.88^{+0.62}_{-0.48}$
Platinum (Pt)	73.5 - 80.5	36	4.50 ± 0.75
Lead (Pb)	80.5 - 86.5	8	$1.00^{+0.49}_{-0.35}$

Table 3.4 Numbers of particles in various charge groups, as taken from Figure 3.14.

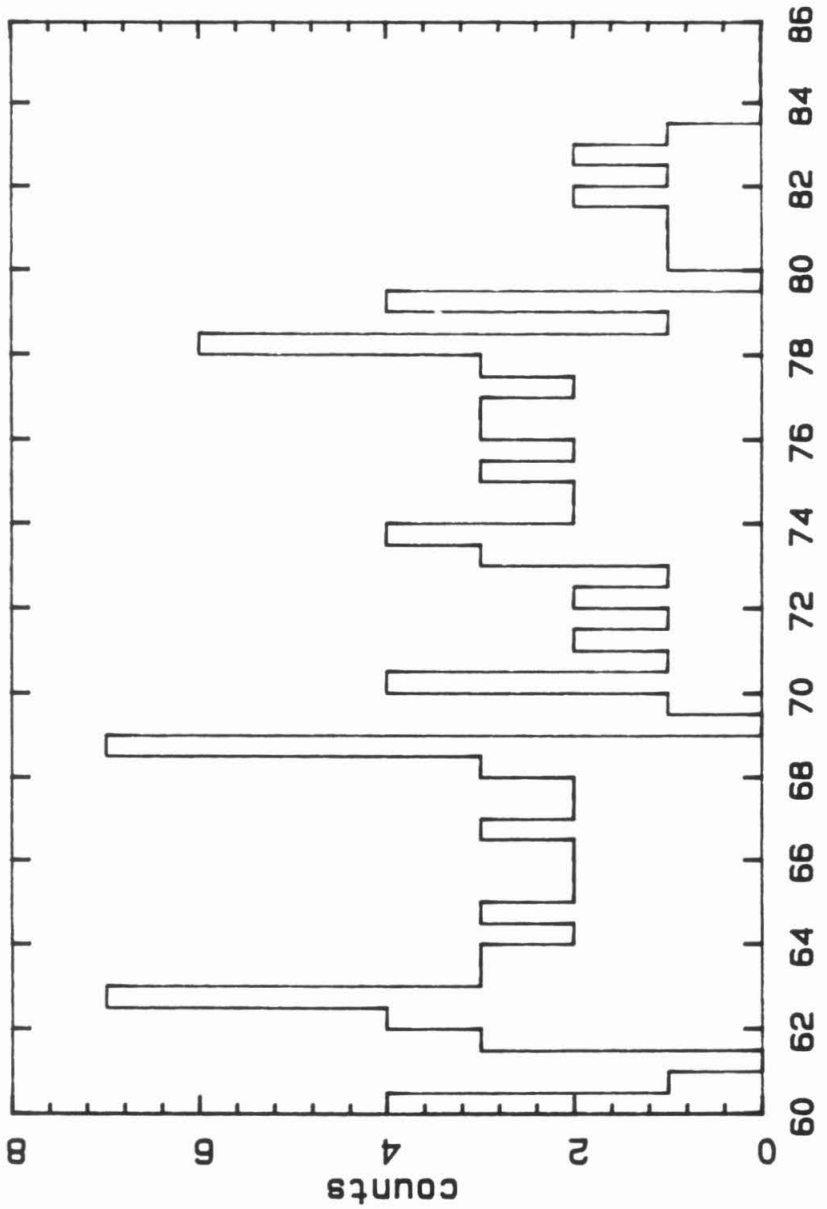

Figure 3.14 The distribution of particles in the range Z_C=60 to 86. There were no selected particles of higher charge.

3.4.8. Gaussian Peak Fitting

Returning to Figures 3.9, 3.12, and 3.13, there appears to be a smooth change in the shape of the peaks as Z increases, with the most likely explanation being a relative absence of lower energy particles at the heavier elements. Moreover, many peaks in the Z = 34 to 60 region are well approximated by gaussian distributions. This section describes the use of gaussian distributions to determine the abundances.

These fits use a histogram of particles from Z_C = 31 to 62 in 0.25 charge unit bins, with the abundances of the elements from 30 to 62 adjusted to obtain the best value of the likelihood. In those cases where the best fit value of a particular abundance would be less than zero, the fitting program constrained the value at zero. This occurs with the elements $_{49}$In, $_{57}$La, and $_{59}$Pr, and is primarily caused by low statistics. The effective constraint of these abundances is ignored for the purposes of calculating the number of degrees of freedom.

Each element was modelled by a distribution of variance σ_Z^2 and mean $Z - \Delta_Z$. The Δ_Z terms allow the peaks to be offset from their nominal positions, as might happen if the energy spectra were different for different elements. Adjustment of all the σ_Z and Δ_Z gives a result with too many free parameters, so some constraints were used.

Two fits were tried, with the results of the first fit being used to guide the second. In the first fit, the values of σ_Z were set to a single value, σ, which was allowed to vary. The best fit value of σ was 0.383, 15% higher than the value obtained for the non-gaussian fit to the iron distribution (Figure 3.9). Since they are expected to have softer spectra, and hence lower median energies, the values of Δ_Z of the odd elements were all fixed at -0.3, while those for the even elements were allowed to vary.

Inspection of Figures 3.12 and 3.13 suggests that there is a correlation between the offset of a peak and whether an element is mostly primary or mostly secondary: $_{38}$Sr and $_{56}$Ba are mostly primary and have small offsets, while most of the other elements have substantial secondary contributions

and do appear to have significant offsets. To investigate this apparent correlation, the best fit values of Δ_Z were plotted as a function of the primary fraction at earth, as given by a particular propagation calculation. This calculation, of the type described in Brewster et al. (1985) and in more detail by Brewster (1984), was performed at the University of Minnesota (M. Kertzmann, private communication). It assumes a source composition identical to the solar system composition given by Anders and Ebihara (1982), with the step function FIP fractionation given in (1.2). The pathlength distribution was assumed to be the exponential of (1.4), with the escape length chosen to be 7 gcm^{-2} of pure hydrogen. The resulting primary fractions of the elements from Z=30 to 61 are given in Table 3.5.

The open circles in Figure 3.15 plot the fitted offsets of the even elements as a function of their primary fraction. The uncertainties in the fitted values of the Δ_Z are not shown in this figure, although they are quite large, ranging from a minimum of ± 0.04 charge units for $_{34}$Se to a maximum of ± 0.15 at $_{54}$Xe, comparable to the scatter in the values.

Despite the large amount of scatter, the data in Figure 3.15 do appear to be correlated. The rank correlation coefficient has a value of 0.4549, which is significant at the 90% level (two tailed t-test, 12 degrees of freedom). In order to test the model dependence of this correlation, the calculation was repeated for propagation calculations assuming no FIP dependence, and for a calculation which assumed the exponential FIP dependence given in Brewster et al. (1985). The values of the rank correlation coefficients in these cases were 0.2264 and 0.3670 respectively, with significance levels of 56 and 80%. Thus the correlation depends on the assumption of a FIP dependence.

The straight line in Figure 3.15 represents an unweighted least squares fit to the open circles. This line was used to fix the values of Δ_Z for the odd elements in the final fit, according to their primary fractions. In this fit, the value of σ_Z was no longer assumed to be independent of charge, but rather have the form given by

$$\sigma_Z^2 = \sigma_1^2 + \sigma_2^2 Z^2 \qquad (3.10)$$

Table 3.5

Z	element	fraction	Z	element	fraction
30	Zn	0.943	46	Pd	0.234
31	Ga	0.685	47	Ag	0.346
32	Ge	0.826	48	Cd	0.253
33	As	0.319	49	In	0.161
34	Se	0.635	50	Sn	0.488
35	Br	0.318	51	Sb	0.221
36	Kr	0.330	52	Te	0.606
37	Rb	0.667	53	I	0.215
38	Sr	0.799	54	Xe	0.336
39	Y	0.751	55	Cs	0.562
40	Zr	0.805	56	Ba	0.762
41	Nb	0.322	57	La	0.627
42	Mo	0.477	58	Ce	0.620
43	Tc	0.0	59	Pr	0.455
44	Ru	0.370	60	Nd	0.585
45	Rh	0.194	61	Pm	0.0

Table 3.5 The primary fractions of each element from Z=30 to 61, after propagation through 7 gcm^{-2} of pure hydrogen. This calculation assumes a solar system source composition and the step function FIP fractionation given in (1.2).

where σ_1 represents the resolution due to photoelectron statistics and σ_2 allows for mapping uncertainties. Some rearrangement leads to

$$\sigma_Z^2 = \sigma_{Fe}^2 + \sigma_2^2(Z^2-26^2) \qquad (3.11)$$

The value of σ_{Fe} was fixed at 0.338, obtained in the earlier fit to the iron data with no rigidity cutoff. The values of Δ_Z for the even elements and the value of

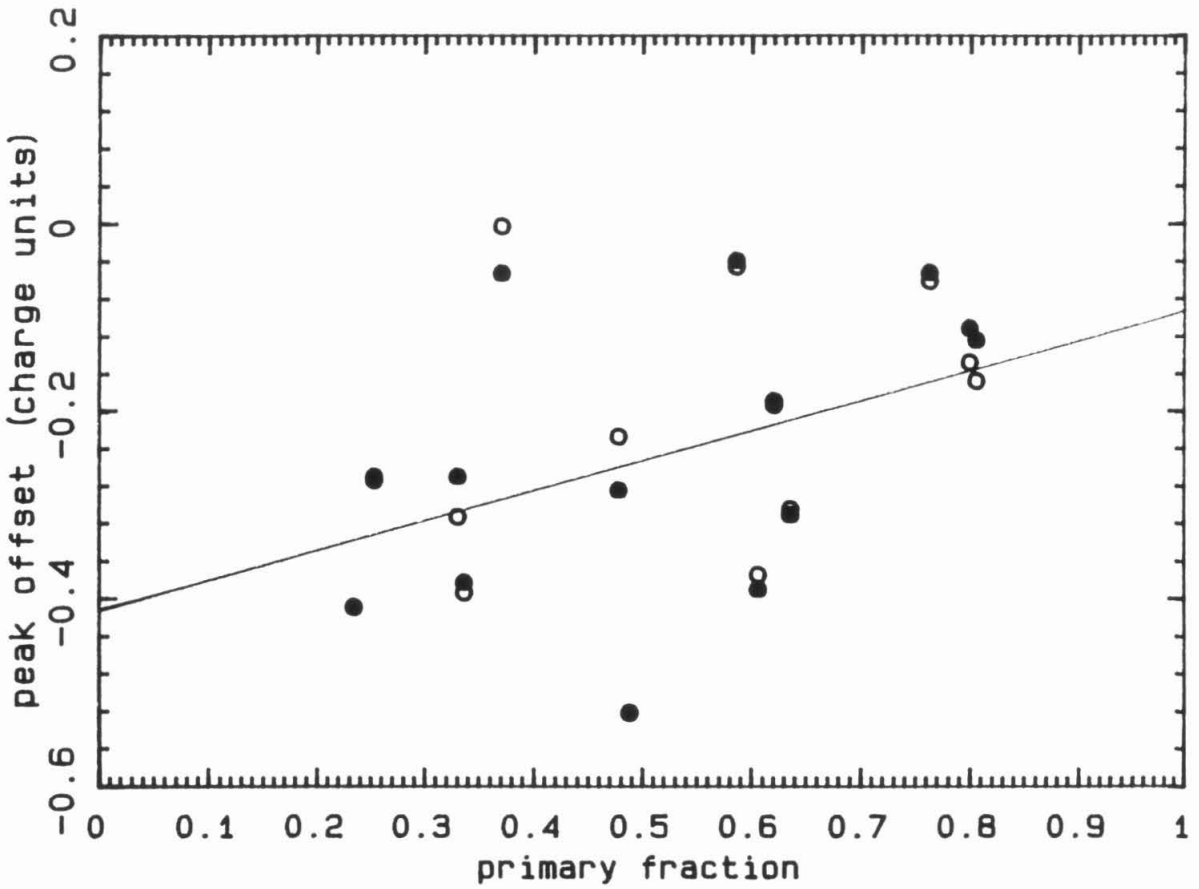

Figure 3.15 Fitted peak offsets of even elements from Z=34 to 60 inclusive, plotted as a function of their primary fraction. The open circles represent the results obtained in the first fit, where the odd element offsets were set to -0.3. The straight line represents an unweighted least squares fit to the open circles, which was used to fix the odd offsets in the final fit. The solid circles show the fitted even offsets resulting from the final fit. See text for discussion.

σ_2 were allowed to vary.

The offsets of the even elements 34-60 obtained with this fit are more correlated with the primary fraction than after the initial fit. The values of the rank correlation coefficients in the no FIP, exponential FIP, and step FIP cases are 0.3011, 0.5780, and 0.4110 repectively, with significance levels of 70, 97, and 86%. The best fit value of σ_Z was 0.0044, implying an rms resolution of 0.351 charge units at Z = 34, increasing to 0.413 charge units at Z = 60. The solid circles in Figure 3.15 show the final offsets as a function of the primary fraction in the case of a step FIP dependence.

We now consider the meaning of the peak offsets. If we assume that the nominal peak position (i.e., at Z_C = Z) corresponds to particles at β=1, we can calculate the values of β and the corresponding energies for various offsets of the peak at charge 50. This is equivalent to supposing that the particles of each element have a well defined modal energy. These energies were calculated assuming that the Čerenkov response is completely given by (2.6), and are shown in Table 3.6. The value of the refractive index was assumed to be 1.528.

Table 3.6

offset in c.u.	β	E (GeV/amu)
-0.1	0.9973	11.9
-0.2	0.9947	8.1
-0.3	0.9921	6.5
-0.4	0.9895	5.5

Table 3.6 Peak offsets at charge 50 for monoenergetic particles at various energies.

From Table 3.4, we see that quite large shifts in the peak position can arise from relatively modest changes in the modal energy. This is because these

shifts are rather small fractions of the total signal at these high charges. As mentioned in Chapter 1, secondary elements at lower Z have been found to be less abundant at higher energies relative to their primaries, and hence have lower modal energies. Thus it is at least plausible that there might be some correlation between the peak position and the primary fraction, as we found above.

Figures 3.16a and 3.16b show the final fit to the data using the gaussian distributions. The data appear to be well fit by the gaussian distributions, with the peak to valley ratios in the Z = 40-50 region being much better reproduced than when the iron distribution was used. Again applying the χ^2 test with adjacent bins grouped to obtain $\mu_i > 5$, the value of Q^2 was 35.77. With 37 degrees of freedom, the probability that χ^2 is this high or higher is 52.6%, implying an excellent fit. The corresponding probability for the initial fit was 65.2%. The reason that Q^2 is larger in the final fit is because the form (3.11) forces a larger value of σ than is strictly necessary in the 50s as a result of compensating for the non-gaussian shapes of the 30s peaks, while being fixed at iron.

3.4.9. Estimation of Uncertainties

Near the maximum in $\log L(\vec{A})$ we may transform variables to a new space $u_Z(A_Z)$, in which logL is parabolic in each variable, i.e., $L(\vec{u})$ is a multivariate gaussian in this new space. Furthermore, if L_0 is the maximum value of L, then

$$L(u_Z) = L_0 \exp\left[- \frac{(u_Z - u_{0Z})^2}{2\sigma_Z^2} \right] \tag{3.12}$$

where σ_Z^2 is the variance of L in the variable u_Z. Then the probability that the true value of u_Z lies in the interval $[u_{0Z}-\sigma_Z , u_{0Z}+\sigma_Z]$ is 68.3 %, provided the other components of $\vec{u}$ remain fixed at their most likely values. The value of logL at the limits of this confidence interval is given by

$$\log L(u_{0Z} \pm \sigma_Z) = \log L_0 - \tfrac{1}{2} \tag{3.13}$$

Thus, without knowing the specific transformation between $\vec{A}$ and $\vec{u}$, we can

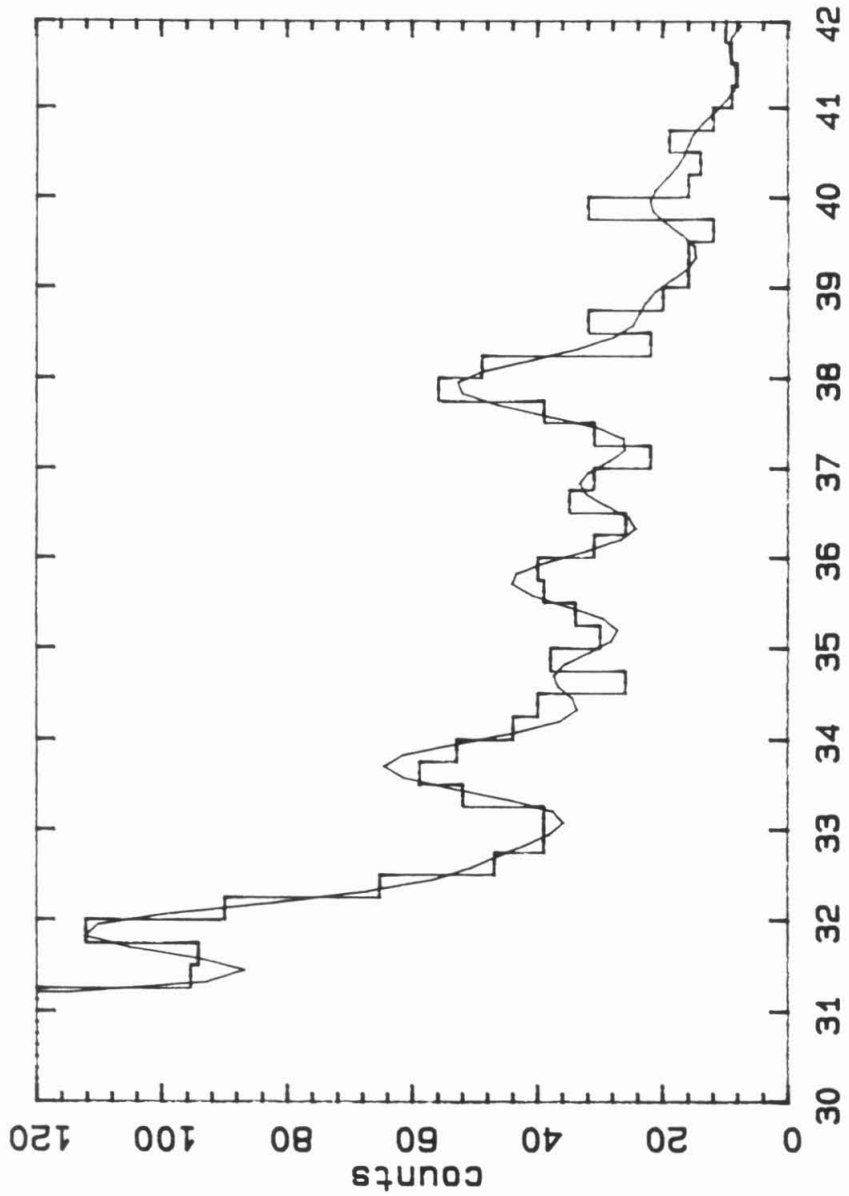

Figure 3.16(a) The distribution of particles from Z_C=31 to 42, superimposed on the curve resulting from the final gaussian fit.

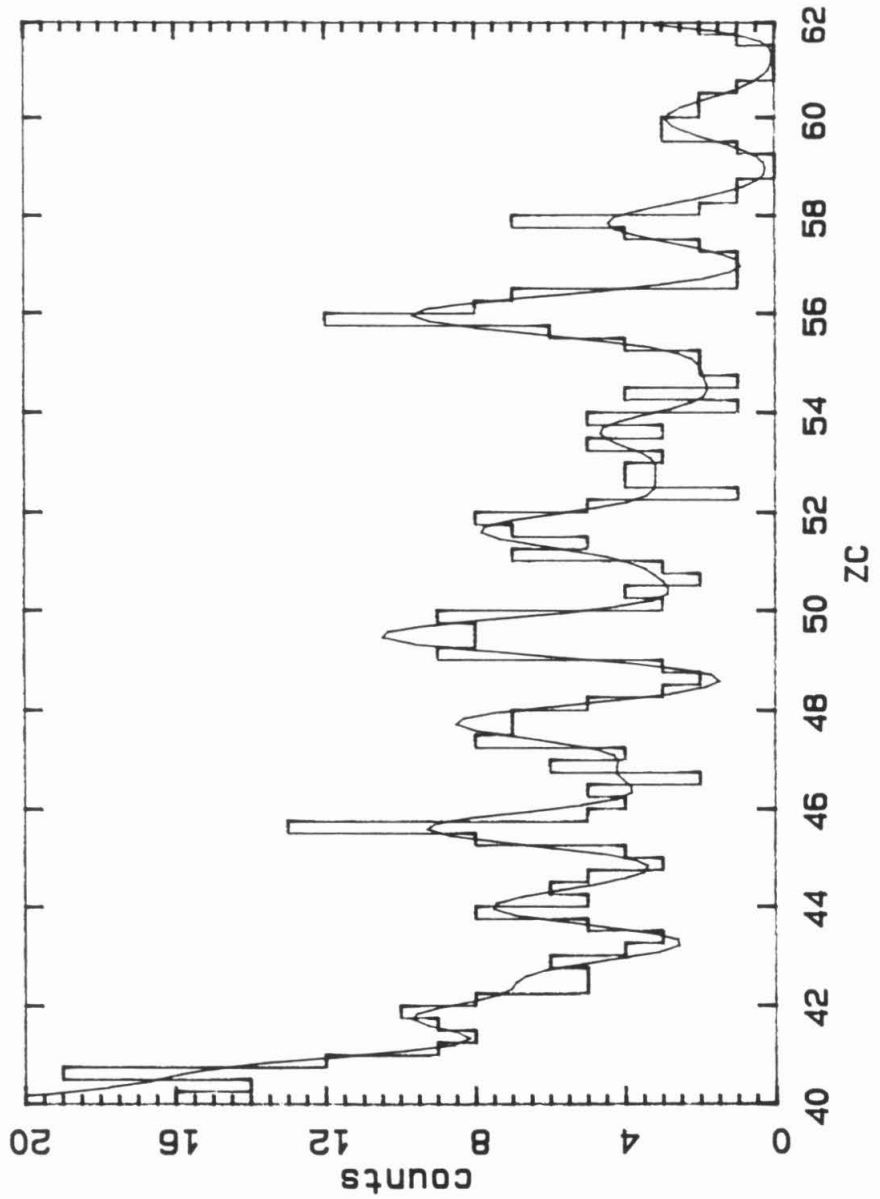

Figure 3.16(b) The distribution of particles from Z_C=40 to 62, superimposed on the curve resulting from the final gaussian fit.

find a 68.3 % confidence interval for A_Z by the numerical solution of

$$\log L(A_{Z\pm}) = \log L_0 - \tfrac{1}{2} \tag{3.14}$$

where A_{Z+} corresponds to $u_{0Z}+\sigma_Z$ and A_{Z-} to $u_{0Z}-\sigma_Z$.

For some elements the lower confidence limit from (3.14) is negative. Since negative abundances are unphysical, the abundances of such elements are unresolved and we can only determine an upper limit, using a more general confidence interval. Given the likelihood function $L(\vec{A})$, we can define a one dimensional confidence interval [a,b] for a particular A_Z by

$$\frac{\int_a^b L(\vec{A})\,dA_Z}{\int_0^\infty L(\vec{A})\,dA_Z} = \beta \tag{3.15}$$

where β is the probability that the true value of A_Z lies within [a,b]. Setting $\beta = 0.683$ and requiring L(a)=L(b) reproduces the same limits as (3.14). In the case of upper limits, we require the interval $[0\ ,\ A'_Z]$ such that $\beta = 0.841$, so that the probability that the true value of A_Z lies above the stated interval is 15.9 % for both resolved and unresolved elements. Table 3.7 gives the abundances of the elements from Z = 33 to Z = 60 using the gaussian fit, together with their confidence intervals from (3.14). In those cases where the abundance is unresolved, the fitted value of the abundance is given in square brackets, together with the upper limit calculated using (3.15). It should be noted that this approach to obtaining one dimensional confidence intervals results in the enclosed volume containing a fraction $\sim\beta^M$ of the total probability, where M is the number of elements being fitted. This is only a small fraction of the total probability if M is large.

If the uncertainties in the observed abundances were normally distributed then the χ^2 distribution could be used to draw conclusions about the nature of the cosmic ray source, by comparing the observed abundances to those predicted by various models. Although the abundances in Table 3.7 are not normally distributed, for most elements the deviation from normality is

Table 3.7

Z	element	fitted count	Z	element	fitted count
33	As	139^{+16}_{-15}	47	Ag	$14.8^{+5.2}_{-4.4}$
34	Se	224^{+16}_{-17}	48	Cd	$32.5^{+6.5}_{-5.7}$
35	Br	127^{+14}_{-13}	49	In	[0] < 7.9
36	Kr	156^{+14}_{-14}	50	Sn	$41.0^{+7.2}_{-6.0}$
37	Rb	117^{+13}_{-12}	51	Sb	$10.4^{+4.4}_{-4.3}$
38	Sr	189^{+16}_{-14}	52	Te	$30.2^{+6.0}_{-5.9}$
39	Y	75^{+11}_{-10}	53	I	$10.8^{+4.5}_{-4.0}$
40	Zr	75^{+10}_{-10}	54	Xe	$18.0^{+4.8}_{-4.7}$
41	Nb	$48.5^{+8.5}_{-8.4}$	55	Cs	$7.1^{+3.8}_{-3.1}$
42	Mo	$33.6^{+6.4}_{-7.2}$	56	Ba	$39.2^{6.9}_{-5.8}$
43	Tc	$22.5^{+5.4}_{-5.7}$	57	La	[0] < 5.0
44	Ru	$27.0^{+6.1}_{-5.5}$	58	Ce	$18.3^{+4.5}_{-4.0}$
45	Rh	$7.4^{+6.8}_{-3.8}$	59	Pr	[0] < 3.4
46	Pd	$34.9^{+6.8}_{-5.9}$	60	Nd	$12.0^{+3.7}_{-3.2}$

Table 3.7 Fitted number of particles of each element, assuming that Z_C has a gaussian distribution. Confidence intervals were obtained using (3.14) and (3.15). Numbers in square brackets refer to the fitted number of particles where the confidence interval includes zero. The abundances of odd elements in this table are unreliable and must be combined with those of the even elements: see text and Table 3.8.

not great. There also are correlations between the abundances of adjacent elements, which must be considered when combining abundances or taking ratios.

Comparison of the results in Table 3.7 with those of Table 3.3 shows that in the charge range Z = 33-38 the odd element abundances are very sensitive to the fitting assumptions, with the even element abundances less so. In this region, the distributions are probably in transition from the iron shape to the nearly gaussian shape in the 50s. Thus the correct representation of these distributions should have more particles on the low side of the peak, and if these particles are absent from the fitting distribution, then the derived abundances of the odd elements include a contribution from the next higher even. The agreement between the two sets of abundances improves if the elements are grouped in pairs: each odd with the even above it. Because the gaussian assumption is a better fit to the data, we choose to adopt the abundances resulting from it after pairing adjacent elements. This procedure works well for all elements below charge 61, with the exception of the 41-42 pair. As shown in Figure 3.16a, the large fitted abundance of $_{41}$Nb is due to the unexpected peak in the bin beginning at Z_C = 40.5. This peak is almost certainly a statistical fluctuation, and is more likely to result from Z = 40 particles than either 41 or 42. Thus the pairing procedure was modified by grouping elements 39, 40, and 41 together and leaving 42 ungrouped.

The difficulty with grouping adjacent elements is that the uncertainty in a group abundance can be easily calculated only by assuming that the data in each bin are normally distributed, rather than Poisson. We now make this assumption to derive the uncertainties in the group abundances below charge 61. Let

$$H_{Z,Z'} = - \frac{\partial^2 \log L}{\partial A_Z \partial A_{Z'}} \tag{3.16}$$

Then H is known as the information matrix and is equal to the inverse of the covariance matrix V (Eadie et al., 1971):

$$V_{Z,Z'} = (H^{-1})_{Z,Z'} \tag{3.17}$$

The uncertainty in the quantity $f(\vec{A})$ is then given by

$$\sigma^2_{f(\vec{A})} = \sum_Z \sum_{Z'} V_{Z,Z'} \frac{\partial f}{\partial A_Z} \frac{\partial f}{\partial A_{Z'}} \tag{3.18}$$

Elements whose best fit abundances were zero were excluded from the calculation of the covariance matrix, and in those cases the uncertainty in the group is assumed to be that of the even element alone. The grouped abundances are listed in Table 3.8, together with their uncertainties calculated using (3.16), (3.17), and (3.18).

The uncertainty in each of the abundances of the 33-34, 35-36, and 37-38 groups has been increased by adding in quadrature the difference between the abundance shown in Table 3.8 and that derived from the fit using the iron spectrum, given in Table 3.3. Thus these uncertainties include estimates of the systematic uncertainties resulting from approximating the actual Z_C distributions with gaussian distribrutions. The Z>60 groups are also shown in this table, and were obtained from Table 3.4, together with their uncertainties due to counting statistics. The normalization to iron is also shown in this table, using the fitted count of 8.00±0.24 million obtained in Section 3.4.3, and ignoring the possible spectral differences between iron and the heavier elements.

Table 3.8		
Z	number of particles	abundance (Fe≡10^6)
33-34	363±33	45.4±4.1
35-36	283±19	35.4±2.4
37-38	306±19	38.3±2.4
39-40-41	199±15	24.8±1.9
42	33.6±7.2	4.20±0.90
43-44	49.5±8.6	6.2±1.1
45-46	42.3±7.4	5.29±0.93
47-48	47.3±7.2	5.91±0.90
49-50	41.1±6.7	5.14±0.84
51-52	40.6±6.9	5.08±0.86
53-54	28.8±5.9	3.60±0.74
55-56	46.3±7.0	5.79±0.88
57-58	18.3±4.3	2.29±0.54
59-60	12.1±3.5	1.51±0.44
62-69	$48.0^{+0.69}_{-0.69}$	$6.00^{+0.87}_{-0.87}$
70-73	$15.0^{+5.0}_{-3.8}$	$1.88^{+0.62}_{-0.48}$
74-80	$36.0^{+6.0}_{-6.0}$	$4.50^{+0.75}_{-0.75}$
80-83	$8.0^{+3.9}_{-2.8}$	$1.00^{+0.49}_{-0.35}$

Table 3.8 Abundances of charge groups, with uncertainties calculated from the information matrix for Z≤60. For Z>60, the groups of Table 3.4 are given, with uncertainties obtained using counting statistics.

Chapter 4

Discussion

4.1. Comparisons With Other Data

Previous results from the HNE have been given for the Z = 32 to 42 region (Binns et al., 1983a), the 50 to 58 region (Krombel 1983, Binns et al., 1983b, and Stone et al. 1983), the 62 to 83 region (Binns et al., 1985), and for the actinides (Binns et al., 1982). The only other experiment with comparable resolution and statistics is that on the U.K. spacecraft Ariel VI, which has obtained abundances for all elements with $33 \leq Z \leq 48$, and even charge elements for $Z \geq 48$ (Fowler et al., 1985a and 1985b). Table 4.1 lists the weighted numbers of iron nuclei in these various data sets.

Table 4.1

Charge Range Z	Number of Iron (million)	Reference
32 - 42	2.4	Binns et al., 1983a
50 - 58	6.9	Stone et al., 1983
62 - 82	9.6	Binns et al., 1985
$Z \geq 90$	~30	Binns et al., 1982
33 - 48	3.46	Fowler et al., 1985a
48 - 82	8.68	Fowler et al., 1985b
34 - 82	8.00	This work

Table 4.1 Equivalent numbers of iron nuclei in various data sets.

4.1.1. Comparison With Previous HNE Data

Table 4.2 compares the charge group abundances obtained in Chapter 3 with the results of previous studies of the HNE data, and for Z≤60 these data are plotted in Figure 4.1. In the charge 33-42 region, Binns et al. (1983a) fitted a one dimensional histogram of data selected for good resolution and obtained finite abundances for both even and odd elements although the odd abundances were sufficiently uncertain that they were presented as upper limits. In this comparison adjacent elements have been grouped, and the uncertainties have been assumed to be the same as those quoted for the even elements alone.

In the 33-42 region the agreement is very good except at $_{42}$Mo, where the new result is nearly a factor of two below the previous value. Some of this discrepancy may have resulted from adding the Z = 41 abundance to the 39-40 group. If some low energy charge 42 particles were counted as 41s then the apparent abundance of 42 would be lower than the true value. Since the actual abundance of charge 41 is expected to be ~0.4 times that of 42, such a misassignment would account for only a small part of the discrepancy. The Binns et al. (1983a) data set consisted of two subsets of roughly equal sizes, one of which was composed of particles chosen for high rigidity (geomagnetic cutoff greater than 8 GV), while the other subset was chosen for low energy (less than ~900 MeV/amu) by requiring Z_C/Z_I to be less than 0.8. The charges of the particles in the low energy set were estimated using an algorithm which considered both Z_C and Z_I as well as the energy loss within the instrument (Krombel 1980, 1981). Because these charge estimates relied on Z_I, and hence on the relatively poor ion chamber resolution, the possibility of spillover from $_{38}$Sr and $_{40}$Zr into $_{42}$Mo must be considered. However, the ratios $(41.0<Z_C<43.0)/(37.0<Z_C<39.0)$ for the two subsets individually are 0.21±0.07 and 0.22±0.06, and thus the low energy subset does not appear to be affected by spillover any more than the high rigidity subset. The new value for the $_{42}$Mo abundance does agree well with the propagation model which best fits the other elements; this will be discussed in Section 4.2.1.

Table 4.2

Charge pair	This work	Previous HNE
26	1.00×10^{6}	1.00×10^{6}
33-34	45.4±4.1	52^{+9}_{-6}
35-36	35.4±2.4	30^{+8}_{-5}
37-38	38.3±2.4	43^{+10}_{-6}
39-40-41	24.8±1.9	21^{+5}_{-4}
42	4.20±0.90	8^{+2}_{-2}
43-44	6.2±1.1	
45-46	5.29±0.93	
47-48	5.91±0.90	
49-50	5.14±0.84	5.7±1.3
51-52	5.08±0.86	3.4±1.0
53-54	3.60±0.74	3.5±0.9
55-56	5.79±0.88	6.2±1.0
57-58	2.29±0.54	2.8±0.9
59-60	1.51±0.44	
62-69	$6.00^{+0.87}_{-0.87}$	$3.54^{+0.83}_{-0.83}$
70-73	$1.88^{+0.62}_{-0.48}$	$1.04^{+0.45}_{-0.33}$
74-80	$4.50^{+0.75}_{-0.75}$	$4.38^{+0.71}_{-0.71}$
81-83	$1.00^{+0.49}_{-0.35}$	$1.04^{+0.45}_{-0.33}$

Table 4.2 New abundances of element pairs, compared to previously published HNE data. Both sets are normalized to 10^{6} Fe nuclei inside the detector. Previous abundances in the 33-42 region are from Binns et al. (1983a), with the fitted odd abundances added to the evens, and the uncertainty interval of the even element used for the group. Previous abundances in the charge 50-58 region are from Stone et al. (1983), and those above charge 60 are from Binns et al. (1985).

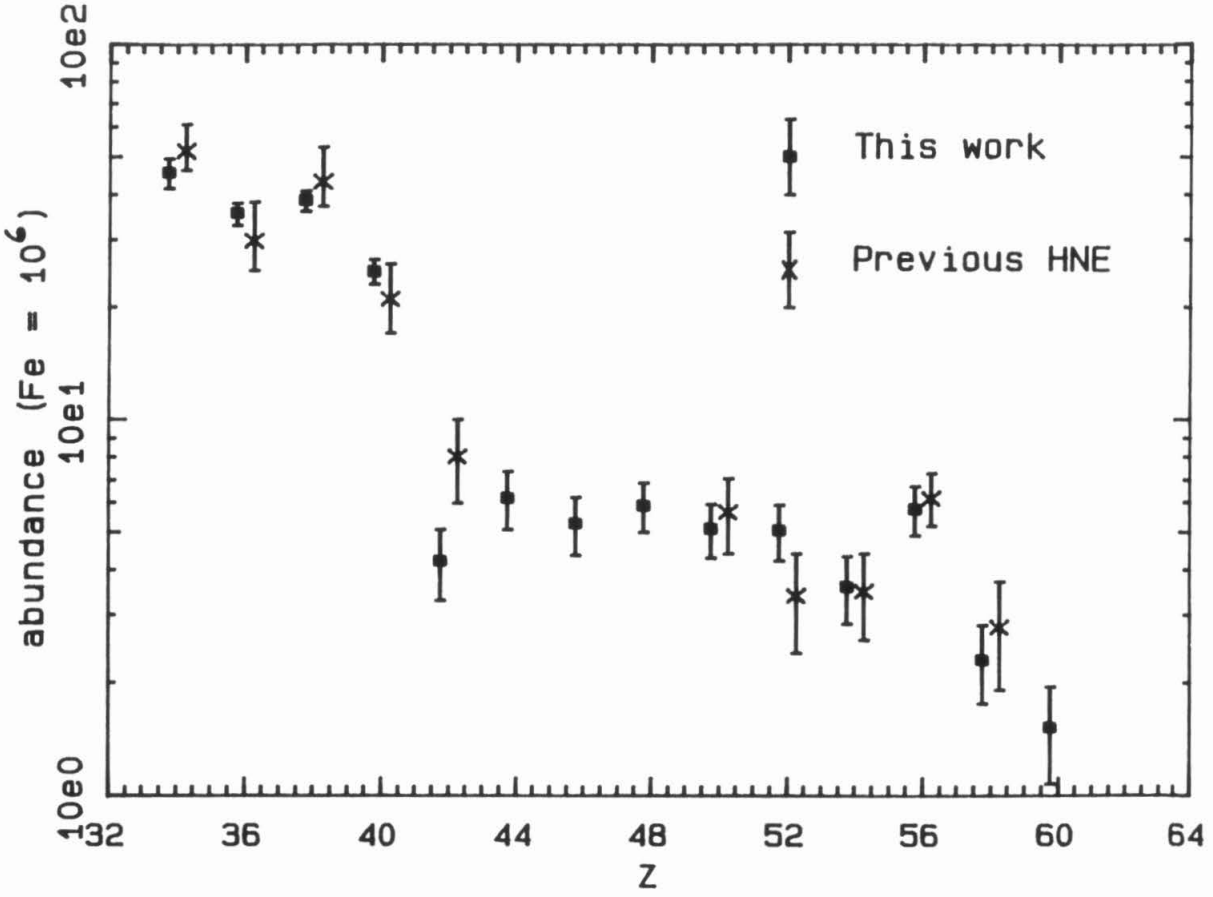

Figure 4.1 The group abundances of Table 3.8, compared with those previously published for this experiment, in the range $33 \leq Z \leq 60$. Previous results are from Binns et al. (1983a) for Z = 34-42, and from Stone et al. (1983) for Z = 50-58.

In the charge 50-58 region, the even element abundances from Stone et al. (1983) are used in Table 4.2, normalized to their stated number of iron nuclei inside the detector. The principal difference between the two sets of abundances is in the amount of $_{52}$Te present: the new value is a factor 1.5 times that found previously. The data set used by Stone et al. (1983) is described in detail in Krombel (1983), and contained four subsets, none of which showed good charge resolution on its own. In the Stone et al data set, 42% of the particles with Z_C>35.0 came from a subset of particles with minimum cutoffs less than 8 GV, but which were chosen to be "high energy" by requiring Z_C/Z_I to be greater than 0.964. Reference to Figure 3.2 shows that this cut lies almost at the peak of the distributions and thus the apparent relative abundances of adjacent elements could be affected by spectral differences, or by statistical fluctuations in the distributions of individual elements. Inspection of the histogram in Krombel (1983) corresponding to this subset shows that it contains very little Te relative to $_{50}$Sn and $_{56}$Ba, presumably because most of the Te lies just outside the Z_C/Z_I cut. This observation probably results from a statistical fluctuation rather than different spectra since although Te has a greater secondary component than Ba, and hence a softer spectrum, Sn has an even greater secondary component and hence an even softer spectrum, and would be even more supressed than the Te if its Z_C/Z_I distribution were appreciably different.

Using the same data set that was used to determine the 50-58 abundances in Stone et al. (1983), Klarmann et al. (1983) found the secondary to primary ratio (44-48)/(50-56) to be 0.70±0.10 inside the detector. Using the results of Table 3.7 and the covariance matrix, the present value of this ratio is 0.89±0.10, which is somewhat higher. The difference is consistent with a secondary to primary ratio which decreases with energy, since the present data set allows particles to have energies as low as 1.5 GeV/amu while that used by Klarmann et al. had few particles below 2.5 GeV/amu because of its higher Z_C/Z_I cut.

In the Z>60 region, the results of Binns et al. (1985) have been normalized to the stated number of iron nuclei. There is a large difference here in

the abundances of the two secondary groups: the new abundances for the LS (Z = 62-69) and HS (Z = 70-73) groups are ~1.8 times those previously obtained, while the abundances of the Pt and Pb primary groups agree very well. The principal differences between the data set of Binns et al. and the present one are that they imposed a 5 GV minimum cutoff rigidity, and also allowed events with good ion chambers only on one side of the Čerenkov detector (one module events). The inclusion of the one module events would have been expected to increase the number of secondaries since it allows more particles to traverse the sidewalls and the unknown material outside them, as well as reducing the discrimination against fragmentation within the instrument. It thus seems likely that the discrepancy in the HS and LS abundances results from the geomagnetic cutoff selection.

The selection for analysis of those particles whose geomagnetic cutoff is greater than some specified minimum reduces the number of particles of all rigidities, but it reduces the number of lower rigidity particles relatively more than the number of higher rigidity particles. This effect is illustrated in Figure 4.2, which shows two "geomagnetic transmission functions" derived specifically for the HNE orbit at Washington University and given by Olevitch (1985). The upper curve in Figure 4.2 shows the fraction of particles which reach the detector, as function of their rigidity, in the case when no minimum cutoff is imposed in the data analysis. As expected, this curve is quite similar to that obtained when the inferred rigidity spectrum at the detector, Figure 3.7, is divided by the assumed rigidity spectrum in interplanetary space, equation (3.5). The lower curve shows the fraction of particles transmitted when a 5 GV minimum cutoff selection is imposed in the data analysis, and each curve is normalized to 1.0 at rigidities above 60 GV. Many more particles of low rigidity are transmitted when no cutoff selection is applied, and the transmission functions differ by a factor of two even at particle rigidities as high as 7.5 GV (which corresponds to ~2.3 GeV/amu in the Z>60 region).

We conclude that the elements between Z = 62 and Z = 73 have an appreciably larger fraction of their particles in the range 1.5 to 2.5 GeV/amu than does iron or the platinum-lead group. This effect is consistent with the loss of

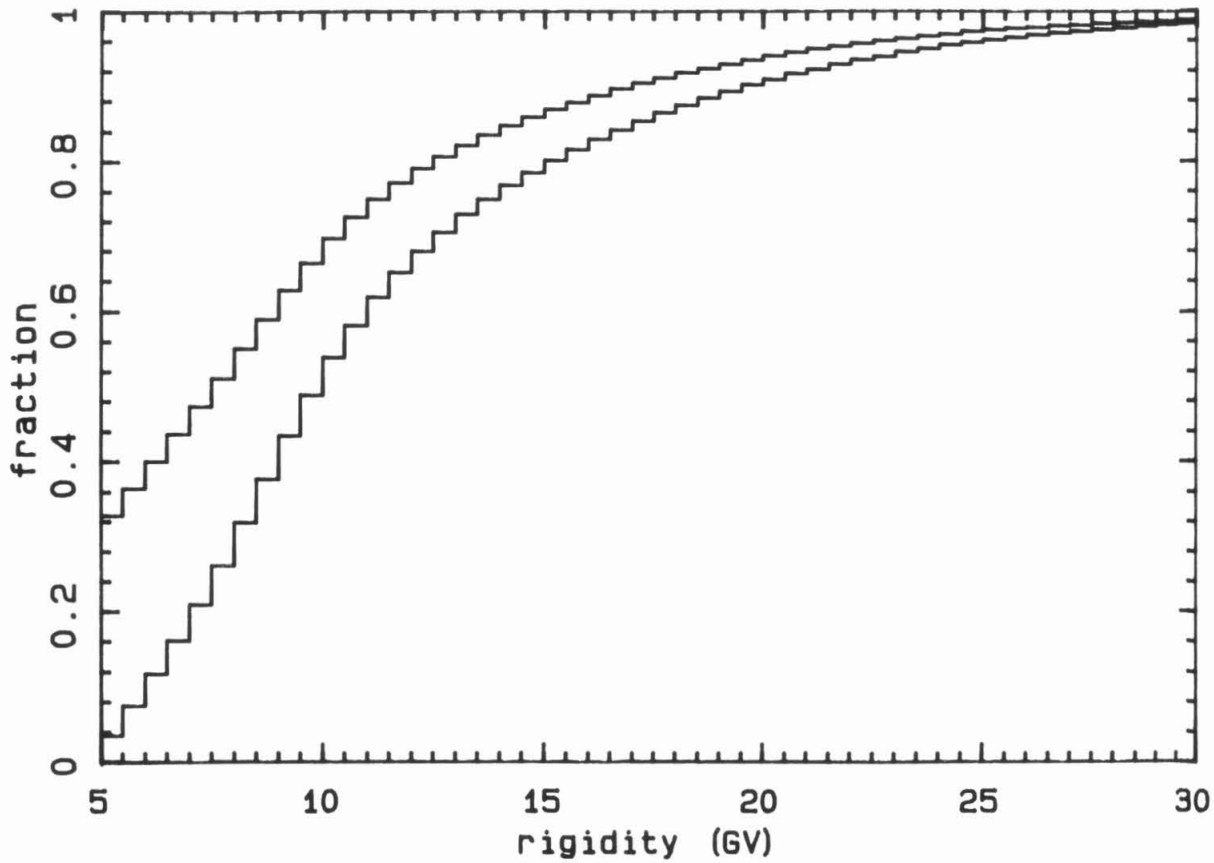

Figure 4.2 Transmission functions which give the fraction of particles which penetrated the geomagnetic field and were observed, as a function of rigidity. The lower curve applies if a selection for 5 GV minimum cutoff is made in the data analysis; the upper curve applies if no such selection is made. Both curves are normalized to one for R>60 GV.

resolution in the Z_C histogram above charge 60, and the observation that secondary elements with Z<26 have softer spectra than the primary nuclei from which they were made. The spectrum of the HS+LS group can be estimated using the transmission functions and their observed abundances relative to iron. If the data are selected to have some minimum cutoff R_C, then the total number of iron in that data set is given by

$$Fe(R_C) = k(R_C) \int_5^\infty \frac{dN_{Fe}}{dR}(R)\, t(R,R_C)\, dR \qquad (4.1)$$

where dN_{Fe}/dR is the differential rigidity spectrum outside the magnetosphere, $t(R,R_C)$ is the transmission function, and $k(R_C)$ is a factor which accounts for the total exposure of the instrument. The lower limit of 5 GV corresponds to the approximate lower energy limit of the selected data. We can write a similar expression for the number of Pt secondaries observed:

$$S(R_C) = k(R_C) \int_5^\infty \frac{dN_S}{dR}(R)\, t(R,R_C)\, dR \qquad (4.2)$$

where $k(R_C)$ is the same factor in both cases. If we let

$$\frac{dN_S}{dR} = f(R)\frac{dN_{Fe}}{dR} \qquad (4.3)$$

then the secondary to iron ratio with a particular cutoff selection is given by

$$\frac{S}{Fe}(R_C) = \frac{\int_5^\infty dN_{Fe}\frac{f(R)}{dR}t(R,R_C)dR}{\int_5^\infty \frac{dN_{Fe}}{dR}t(R,R_C)dR} \qquad (4.4)$$

Using the rigidity spectrum outside the magnetosphere, (3.5), and the transmission functions given in Figure 4.2, the integrals can be evaluated for assumed functions f(R) in the cases of no cutoff selection and a 5 GV cutoff selection, and the ratio

$$\frac{\frac{S}{Fe}(0)}{\frac{S}{Fe}(5)}$$

compared with the observed value of 1.72 for the HS and LS groups combined.

First, we assume that $f(R) = cR^{-\gamma}$. Solving for γ yields the value 2.4±1.0, with the uncertainty calculated from the uncertainties given in Table 4.2, and assuming that the two data sets are uncorrelated, since only ~25% of the particles in the new data set are common to both. Since the spectrum of the Pt-Pb primaries appears to be approximately the same as iron, this this value of γ would require the rigidity dependence of the secondary to primary ratio to be much stronger than is the case for lower charges. For Z<29, the value of γ is 0.7±0.1, and can be explained by using a leaky box model with a rigidity dependent escape length (Ormes and Protheroe, 1983).

Because the rigidity dependence of the secondary to primary ratio is much larger than expected, the possible energy dependence of the fragmentation cross sections must be considered. For example, Kaufman and Steinberg (1980) have measured the formation cross sections of some of the spallation products formed by bombarding $^{197}_{79}$Au nuclei with protons, and find that the cross sections peak between 0.9 and 1.5 GeV/amu for products in the charge range 65-72. As the energy increases, the cross sections fall to about half their peak value by 3 GeV/amu, and then remain constant at higher energies. If the fragmentation cross sections of the other primary nuclei in the platinum group behave similarly then the energy dependence of the cross sections will increase the energy dependence of the secondary to primary ratio. In order to see whether energy dependent cross sections can account for the observed rigidity dependence, we can let

$$f(R) = \begin{cases} \frac{c}{3}(11-R)R^{-\gamma} & \text{if } R<8\text{GV} \\ cR^{-\gamma} & \text{otherwise} \end{cases} \qquad (4.5)$$

This form of f(R) is intended to approximately model the effect of energy dependent cross sections: at 5 GV it is equal to twice the value of $R^{-\gamma}$. Again solving for γ, we obtain the value 1.7±0.8, which is closer to the low Z result. From this we conclude that for Z>60 the enhanced number of secondaries at low energies may result from the combination of a rigidity dependent escape

length with energy dependent cross sections.

4.1.2. Comparison With Ariel Data

The next comparison that may be made is with the Ariel data. The Ariel team has quoted abundances of all charge pairs having Z≥33 (Fowler et al., 1985a,b), however these abundances are quoted after being corrected for fragmentation in the lid of the detector. In order to properly compare the results of the two experiments, the data of Table 3.8 must be corrected for fragmentation within the lid. This calculation is also necessary for any comparison with galactic propagation models.

The fragmentation cross sections of $_{36}$Kr, $_{54}$Xe, $_{67}$Ho, and $_{79}$Au on aluminum were all measured at ~1 GeV/amu during the second Bevalac calibration described in Chapter 2. Preliminary work by Kertzman (private communication) has indicated that the fragmentation cross sections of these nuclei are well represented by

$$\sigma_{\Delta Z} = a(\Delta Z)^{-b} \tag{4.6}$$

where $\sigma_{\Delta Z}$ is the partial cross section in millibarns for a charge change ΔZ, and a and b are given by

$$a = 2.15 \times Z + 64.88 \tag{4.7}$$

$$b = 0.00457 \times Z + 0.365 \tag{4.8}$$

with Z the charge of the nucleus being fragmented. For $\Delta Z = 1$ only, the value of a must be multiplied by a factor 1.15 . The total cross section for all charge changing interactions is given by a modified form of the formula due to Westfall et al. (1979):

$$\sigma_T(A) = 10\pi\, r_0^2 \left[A^{1/3} + A_{Al}^{1/3} - 0.209\,(A+A_{Al})^{1/3} \right]^2 \tag{4.9}$$

where A is the mean mass of nuclei with charge Z, $r_0 = 1.35$, $A_{Al} = 27$, and σ_T is in millibarns. These cross sections are assumed to be independent of energy.

Using these cross sections, the individual element abundances in Table 3.7 were propagated backwards through 1.5 gcm^{-2} of aluminum to obtain the abundances outside the detector. They were then regrouped and normalized to iron to yield the corrected abundances shown in Table 4.3. For those elements above charge 60, the groups of Table 3.8 were decomposed by assuming that each element was represented in the same fraction as that resulting from the galactic propagation of a solar system source composition, after fractionation by the step FIP dependence given in (1.2). The group was then recombined after each abundance was corrected for fragmentation within the lid. The uncertainties quoted in this table are assumed to be the same as those on the original groups since the abundance changes were all less than 5% relative to iron.

The final column in Table 4.3 shows the published abundances from the Ariel group, and for $Z \leq 60$ these are shown together with the HNE data in Figure 4.3. Below charge 48, the Ariel abundances are subject to a downwards correction for electron showers. However, none of the abundances is changed by more than 10% (P.H. Fowler, private communication). Even with these corrections applied, the Ariel abundances are significantly higher than the HEAO abundances for $Z \leq 42$, with the exception of $_{38}Sr$. Inspection of the Ariel histogram in Fowler et al. (1985a) shows that Z = 38 is the only peak which is clearly resolved in their data. Thus it is tempting to suggest that the higher Ariel abundances are due to spillover from the much more abundant lower elements.

Alternatively, the energy spectra of these elements may be rather different to that of iron, with an enhancement of particles at ~1-3 GeV/amu in the 30s relative to iron. Because its orbit was inclined at 55° rather than the 43.6° of the HEAO orbit, the Ariel experiment observed a greater fraction of low energy particles. However, the Ariel group obtained their $Z \leq 48$ abundances from a data set restricted to particles observed in spacecraft locations where the vertical cutoff was greater than 3.4 GV. For the HEAO orbit, the minimum vertical cutoff was approximately 2.8 GV, and thus the HEAO data with no cutoff selection applied should have more, rather than fewer low

Table 4.3		
Charge Group	This work	Ariel
26	1.00×10^6	1.00×10^6
33-34	44.9±4.1	72±5
35-36	35.1±2.4	43±4
37-38	38.1±2.4	38±4
39-40-41	24.7±1.9	35±4
42	4.16±0.90	9±6
43-44	6.1±1.1	3±2
45-46	5.19±0.93	6±2
47-48	5.85±0.90	5.7±1.3
49-50	5.07±0.84	5.5±1.0
51-52	5.05±0.86	7.5±1.0
53-54	3.56±0.74	4.4±1.1
55-56	5.82±0.88	8.0±1.2
57-58	2.26±0.54	1.9±1.0
59-60	1.46±0.44	2.4±0.8
LS	$6.01^{+0.67}_{-0.67}$	7.4±0.9
HS	$1.87^{+0.62}_{-0.48}$	1.9±0.5
Pt	$4.60^{+0.75}_{-0.75}$	5.7±0.8
Pb	$1.04^{+0.49}_{-0.35}$	2.0±0.6

Table 4.3 The abundances of the charge groups of Table 3.8, after correction for fragmentation within the lid of the instrument, compared to those for the Ariel 6 experiment as taken from Fowler et al. (1985a,b). The uncertainties in the Ariel group abundances above charge 60 have been estimated using counting statistics.

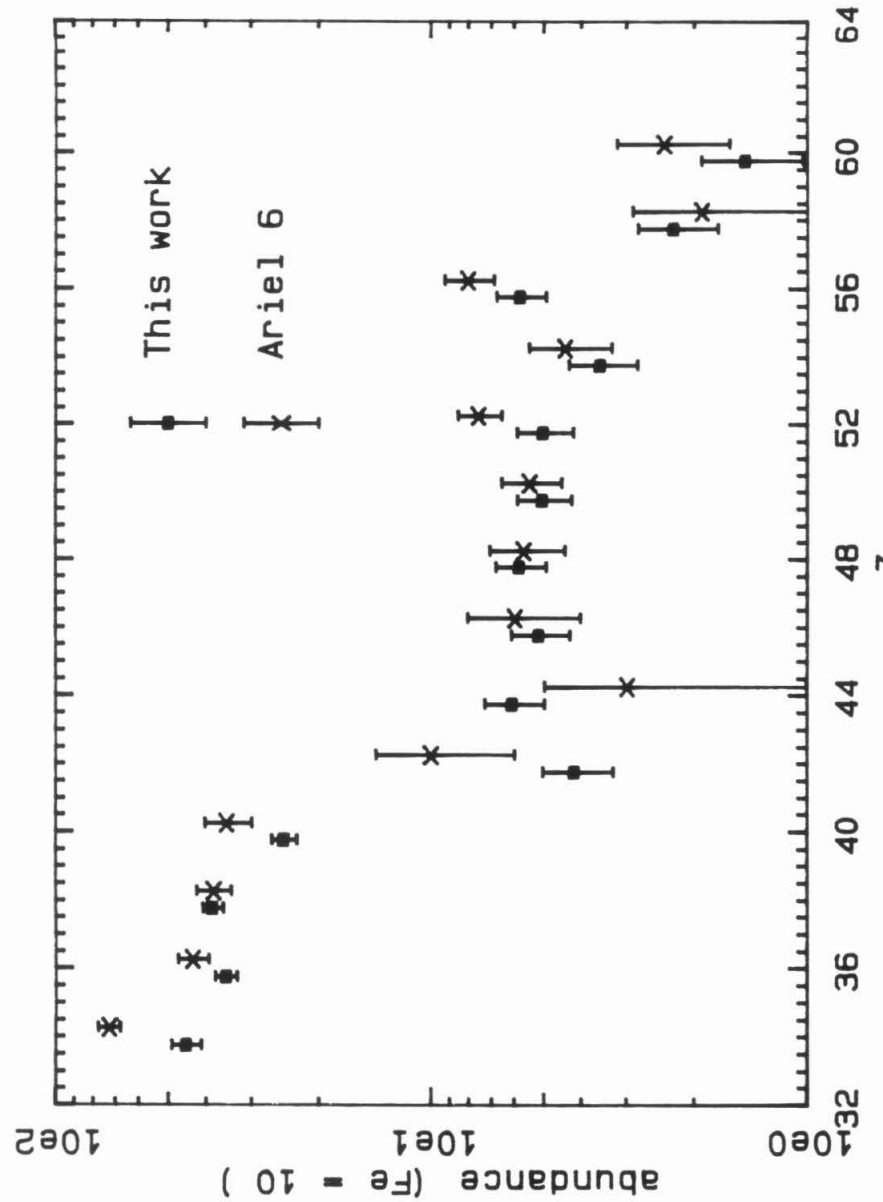

Figure 4.3 The group abundances outside the detector, given in Table 4.3, compared with those from the Ariel VI experiment, as given by Fowler et al. (1985a,b), for $33 \leq Z \leq 60$. See text for discussion.

energy particles than the Ariel data with the 3.4 GV cut. Thus it is unlikely that the higher Ariel abundances are caused by spectral effects, particularly since the shape of the HNE peaks for Z = 38-60 suggests a considerable deficiency of particles in the 1.5-2.5 GeV/amu range, relative to iron.

For Z≥49, the Ariel abundances are systematically higher than the HNE abundances, by a factor of 1.25±0.11 relative to iron. This ratio does not appear to be charge dependent, and suggests that there is a problem with the overall normalization to iron in one of the experiments.

4.2. Comparison With Propagated Sources

The abundances given in Table 4.3 may be compared with the results of galactic propagation models. The particular model that will be used here follows the scheme outlined in Chapter 1, and is described in Brewster et al. (1983, 1985), and in more detail in Brewster (1984). This model takes a given set of source abundances, which are then fractionated by a specified FIP dependence before being accelerated with an R^{-2} rigidity spectrum. The charge spectra are allowed to propagate in ten rigidity bins, each of which has an equal number of particles in an R^{-2} spectrum. These bins are given in Table 3.2 . The particles then propagate in a leaky box with the rigidity dependent path length distribution of Ormes and Protheroe (1983), before being passed through the geomagnetic transmission function of Table 3.2 to give the abundances at an earth orbiting detector. The calculation uses the semiempirical fragmentation cross sections of Silberberg and Tsao (1973a,b), which are calculated at 2.3 GeV/amu and assumed to be independent of energy. Strictly speaking, the propagations should be carried out an isotope by isotope basis, but this would result in an excessive amount of computation, so the calculations use weighted sums of isotope cross sections in order to obtain elemental cross sections, as described in Brewster et al. (1983). The ionization energy loss in the interstellar medium is assumed to be negligible in this calculation.

4.2.1. Comparison With a Solar System Source

Anders and Ebihara (1982) have provided a recent compilation of the relative abundances of elements in the solar system as a whole. These abundances have been determined from meteorite studies and solar spectroscopy, and for most elements have uncertainties of 20% or less. Here we consider the results of propagating this source composition with three different assumptions about the FIP dependence of the injection process. First, Figure 4.4 shows the ratio of the abundances outside the detector to the propagated charge spectrum with no FIP dependence, for Z = 34 - 60. In this figure, the propagations have been normalized so that the ratio of the observed abundance of iron to the propagated abundance is 1.0. The propagated abundances agree remarkably well with the observations, implying that the cosmic ray source composition is quite similar to the solar system composition. There are some significant differences, however: the observed abundances of $_{34}$Se and $_{36}$Kr are many standard deviations below that predicted, while the abundance of $_{42}$Mo is ~3 standard deviations above that predicted, and the abundance of $_{54}$Xe is over 3 standard deviations below.

If we let

$$Q^2 = \sum_{\text{groups}} \frac{[A_Z(\text{obs}) - A_Z(\text{prop})]^2}{\sigma_Z^2} \qquad (4.10)$$

then Q^2 should be distributed approximately as χ^2, thus providing an estimate of how well the propagation calculation describes the data. This procedure ignores the correlations between the abundances of adjacent groups. However, inspection of the correlation matrix defined by (3.17) shows that the magnitudes of the off diagonal terms linking two adjacent even elements are less than 4% of the diagonal terms for those elements, and hence their effect should be unimportant.

For the solar system source with no FIP dependence, the value of Q^2 is 476.4, with 18 degrees of freedom. Although the probability of a value of χ^2 this high is vanishingly small, we have ignored the uncertainties in the propagation calculation, which might be expected to appreciably lower the value of

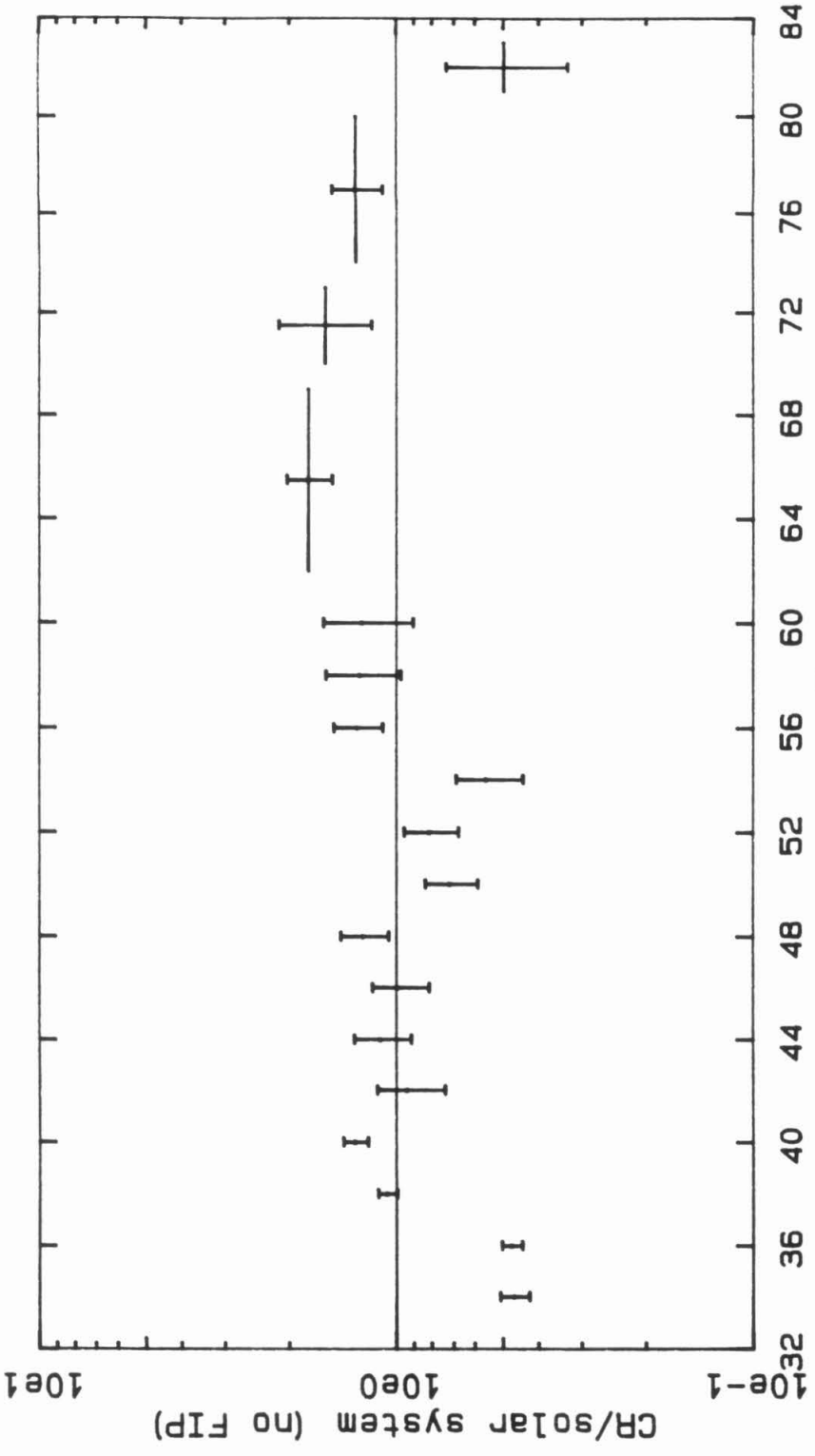

Figure 4.4 The ratios of the group abundances of Table 4.3 to those predicted by a propagation model which assumes a solar system source composition with no FIP fractionation. See text for discussion.

Q^2, and which will be discussed below. The value of Q^2 still enables a relative comparison of the goodness of fit of various propagation calculations.

In previous analyses of the HNE data, the preferred form of the FIP dependence was an exponential:

$$f(\mathrm{FIP}) = 9.31 \exp\left[-0.288\ \mathrm{FIP} \right] \qquad (4.11)$$

This function strongly suppresses the noble gases $_{36}$Kr and $_{54}$Xe, leading to much better agreement with their observed abundances, as shown in Figure 4.5. However, the exponential FIP dependence strongly enhances the accelerated abundances of the low FIP element $_{38}$Sr, destroying the previously good agreement. The agreement is also not as good for the relatively low FIP elements $_{50}$Sn and $_{56}$Ba. The value of Q^2 for this fit is 258.5.

As a third example of FIP dependence, Figure 4.6 shows the comparison of the observed abundances with the results of a propagation calculation using the sloping step function of Letaw et al. (1984), which was given in (1.2). The value of Q^2 for this propagation is 58.98, substantially better than either of the two previous examples, although the χ^2 probability of a value this large or larger is still extremely small: 3×10^{-6}. For $Z\leq60$, the most serious disagreement is in the abundance of $_{34}$Se, and if this element is excluded the value of Q^2 falls to 43.17. The abundances of $_{36}$Kr, $_{40}$Zr, $_{48}$Cd, and $_{50}$Sn all differ by ~2 standard deviations from the value predicted by the propagation.

Above charge 60, the abundances of the two secondary groups and the platinum group are all greater than predicted by the propagation, by a factor whose mean is 1.63. The observed lead abundance contrasts strongly, however, since its value is only $0.44^{+0.21}_{-0.15}$ that predicted by the propagation.

It is important to note that only the errors in the cosmic ray observations have been shown in Figures 4.3, 4.4, and 4.5. Two other important sources of error have been ignored, namely the uncertainties in the source abundances and the uncertainties in the fragmentation cross sections. The uncertainties given in the solar system abundances of Anders and Ebihara (1982) range from 5-10 % of the value for important primary elements. While the inclusion

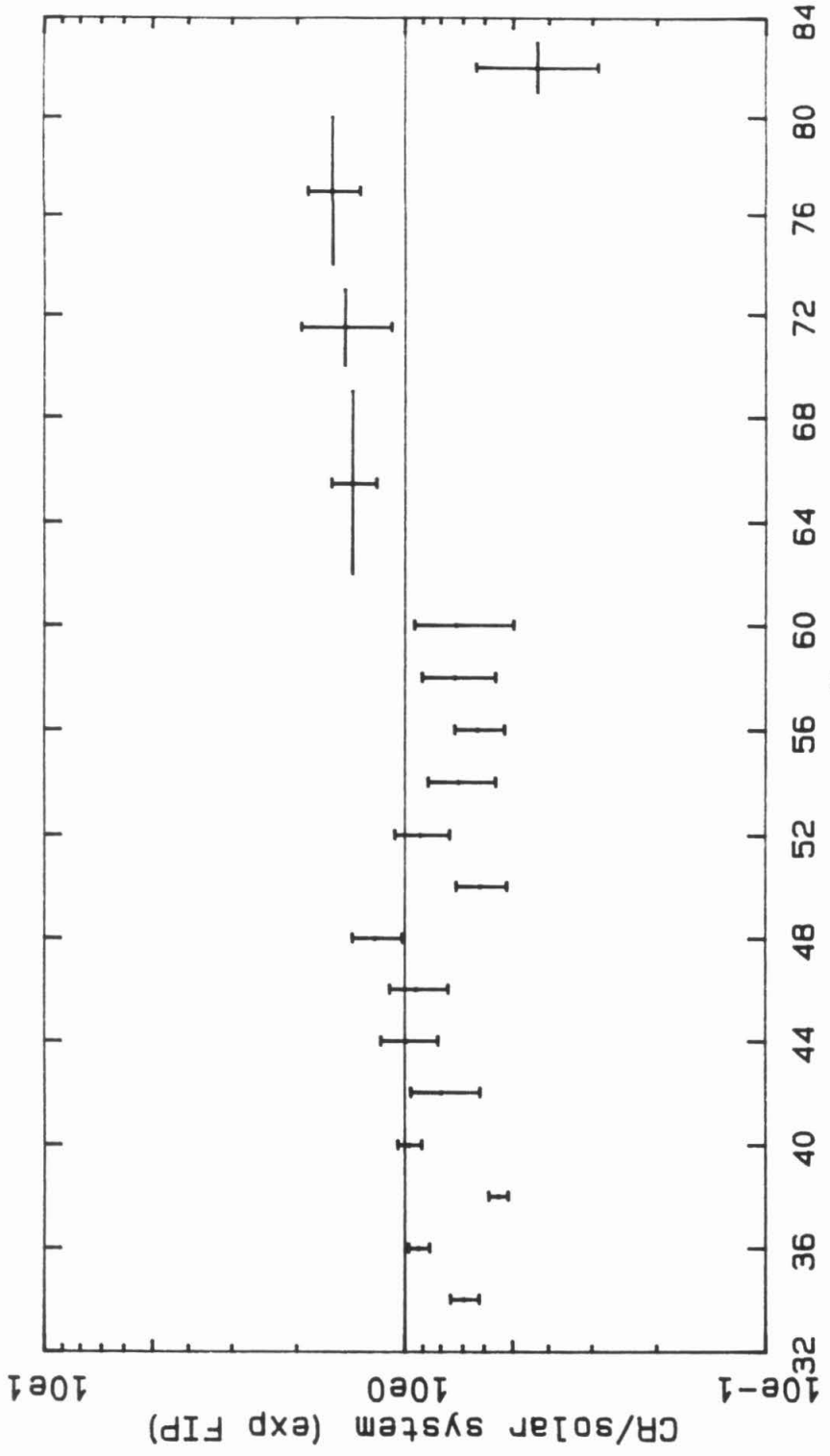

Figure 4.5 The ratios of the group abundances of Table 4.3 to those predicted by a propagation model which assumes a solar system source composition and the exponential FIP fraction of (4.10).

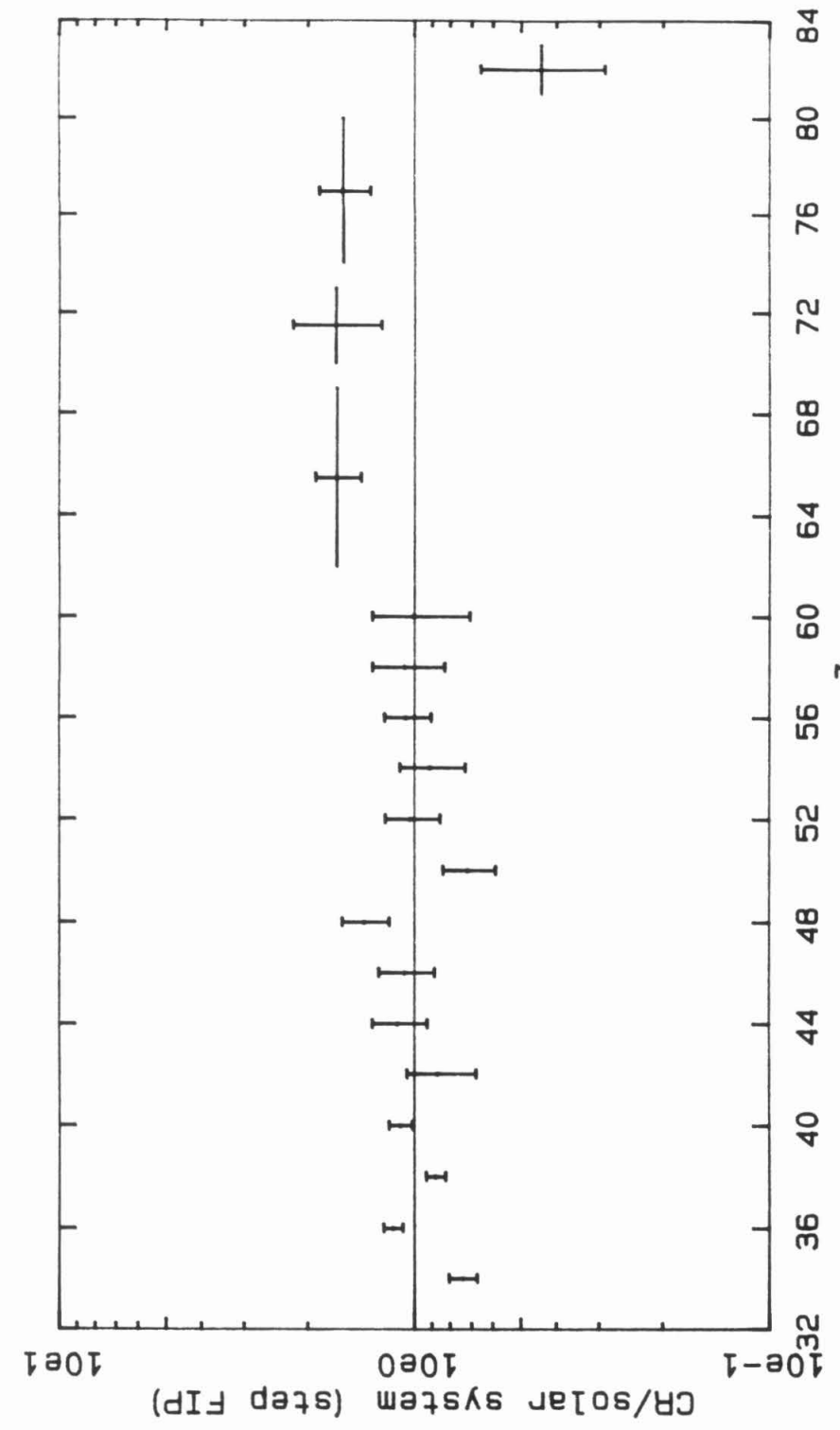

Figure 4.6 The ratios of the group abundances of Table 4.3 to those predicted by a propagation model which assumes a solar system source composition and the step function FIP fractionation of (1.2). This figure should be compared with Figure 4.4 and 4.5.

of these uncertainties would not be sufficient to bring the observed abundance of $_{34}$Se into agreement, it would nonetheless improve the overall fit.

The errors in the cross sections are potentially much larger, with the nominal value being ~35%, although recent work by Letaw et al. (1985) suggests that the errors are rather smaller than this for Z<29. Kertzman et al. (1985) have shown that some of the partial cross sections of $_{54}$Xe at 1.2 GeV/amu are greater than those given by Tsao and Silberberg (1979) by a factor of 1.7, although for small charge changes the discrepancies are less severe, with the observed cross sections about 20% lower than predicted. Although the parameters used in the cross section calculations are being updated as new experimental data become available, the propagation model used here does not incorporate any adjustments made after 1979. It is important to note that the predicted abundances are quite sensitive to the cross section values, particularly for Z>60.

Another possible source of error is in the iron normalization, which has been set to 1.0 in all of these comparisons. If the iron normalization is adjusted in the comparison to the solar system source propagated with a step FIP dependence, Figure 4.6, the lowest value of Q^2 is obtained with all of the propagated abundances lowered by 6.3% relative to iron. With this adjustment there is a small improvement in the fit, with the value of Q^2 falling from 58.98 to 53.73. If $_{34}$Se is excluded from the fit, the value of Q^2 falls further, to 42.71. In this case, the normalization relative to iron falls by only 2.5%.

Because the ultraheavy elements are formed by nucleosynthesis processes which are different to those which produce iron, there is no particular reason why the overall normalization should work out so well, over an abundance range of six orders of magnitude. Furthermore, the elements in the charge range Z = 38-60 appear to be deficient in particles in the energy range 1.5-2.5 GeV/amu, relative to iron. This deficiency introduces a further uncertainty in the iron normalization because it becomes energy dependent. Given all of these uncertainties, the overall agreement shown in Figure 4.6 is quite remarkable.

4.2.2. Comparison With an s-Process Source

In this section the observed abundances of ultraheavy cosmic rays will be compared with the results of propagation calculations which use a pure s-process source. The source composition we will use was obtained by Fixsen, and given in the appendix of Binns et al. (1985). The even element abundances in this source are given in Figure 1.1. Because the parameters used in the calculation were chosen for the best fit to the abundances of the pure s-process nuclei in the solar system, we shall refer to this as the "solar system s-process", to distinguish it from possible variations elsewhere in the galaxy.

Figure 4.7 shows the ratios of the cosmic ray abundances to those predicted by propagating the pure s-process source, with no FIP dependence. We have excluded $_{34}$Se from this plot because it is is not a pure neutron capture element; some is thought to be synthesized in the helium burning phase of stellar evolution. Although iron is not synthesized in neutron capture processes, we have retained the overall normalization so that the source abundance of a pure s-process nuclide is the same, relative to iron, as in the solar system. Because there is no particular reason for constraining the overall normalization in this way, we are free to adjust it to obtain the best fit. This is shown in Figure 4.7, where the horizontal line represents the best fit to the normalization, and indicates that the s-process source abundances should be increased by a factor of 0.856. With this normalization, the value of Q^2 is 87.80, which is not as good as the value of 42.71 which is obtained for the solar system step FIP propagation with both $_{34}$Se deleted and the iron normalization optimized. The value of the normalization factor is largely controlled by the elements $_{36}$Kr, $_{38}$Sr, and $_{40}$Se because the uncertainties on their abundances are much smaller than those of the heavier elements.

Figure 4.8 shows the agreement between the observed abundances and those of the propagated solar system s-process source after fractionation by the step function FIP dependence. The FIP fractionation has destroyed the previous consistency between the three lowest Z groups, and as a result the value of Q^2 is higher at 131.1, including the best fit iron normalization factor

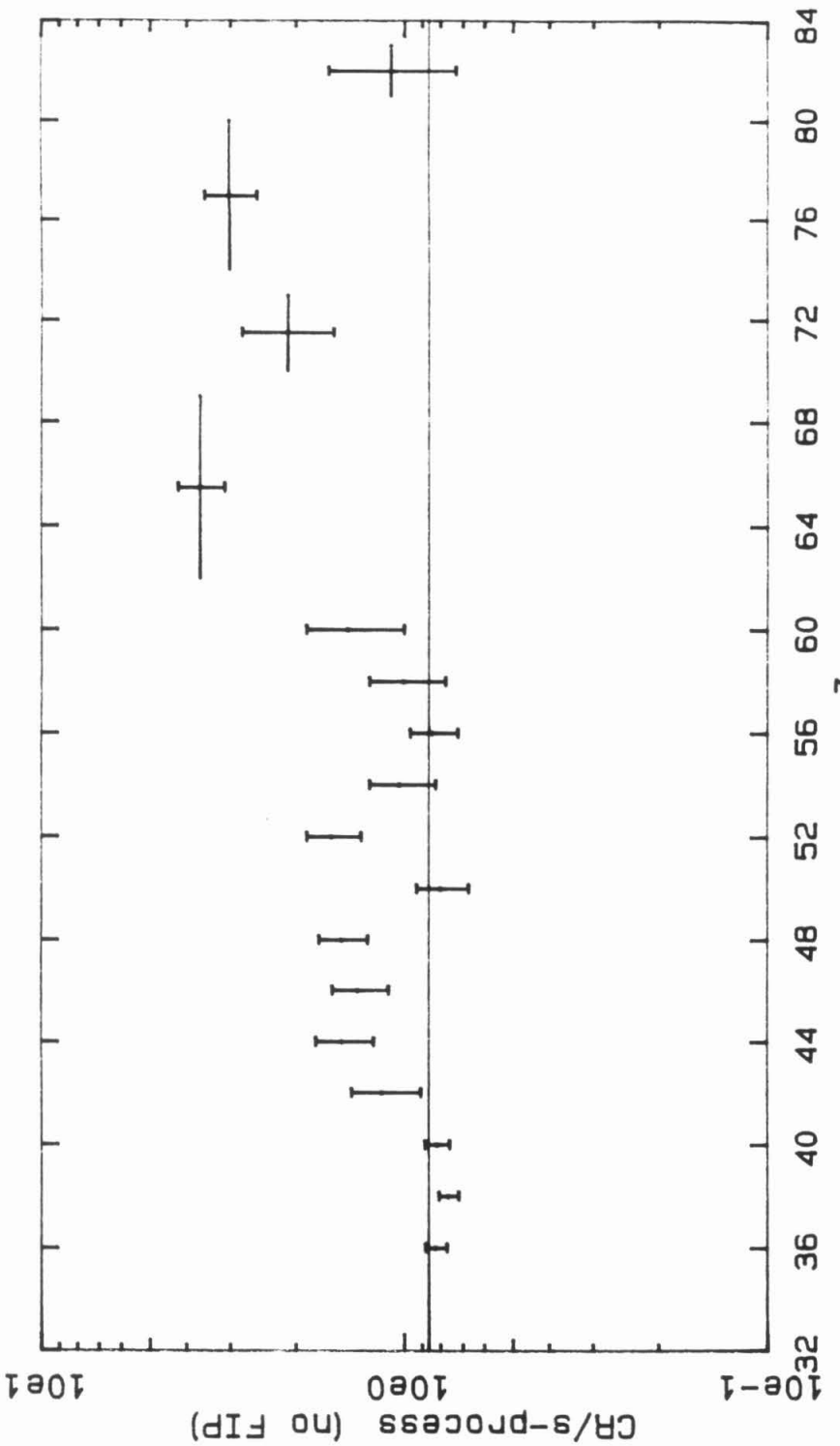

Figure 4.7 The ratios of the group abundances of table 4.3 to those predicted by a propagation using a pure s-process source and having no FIP fractionation. The horizontal line represents the best fit to the normalization relative to iron; see text.

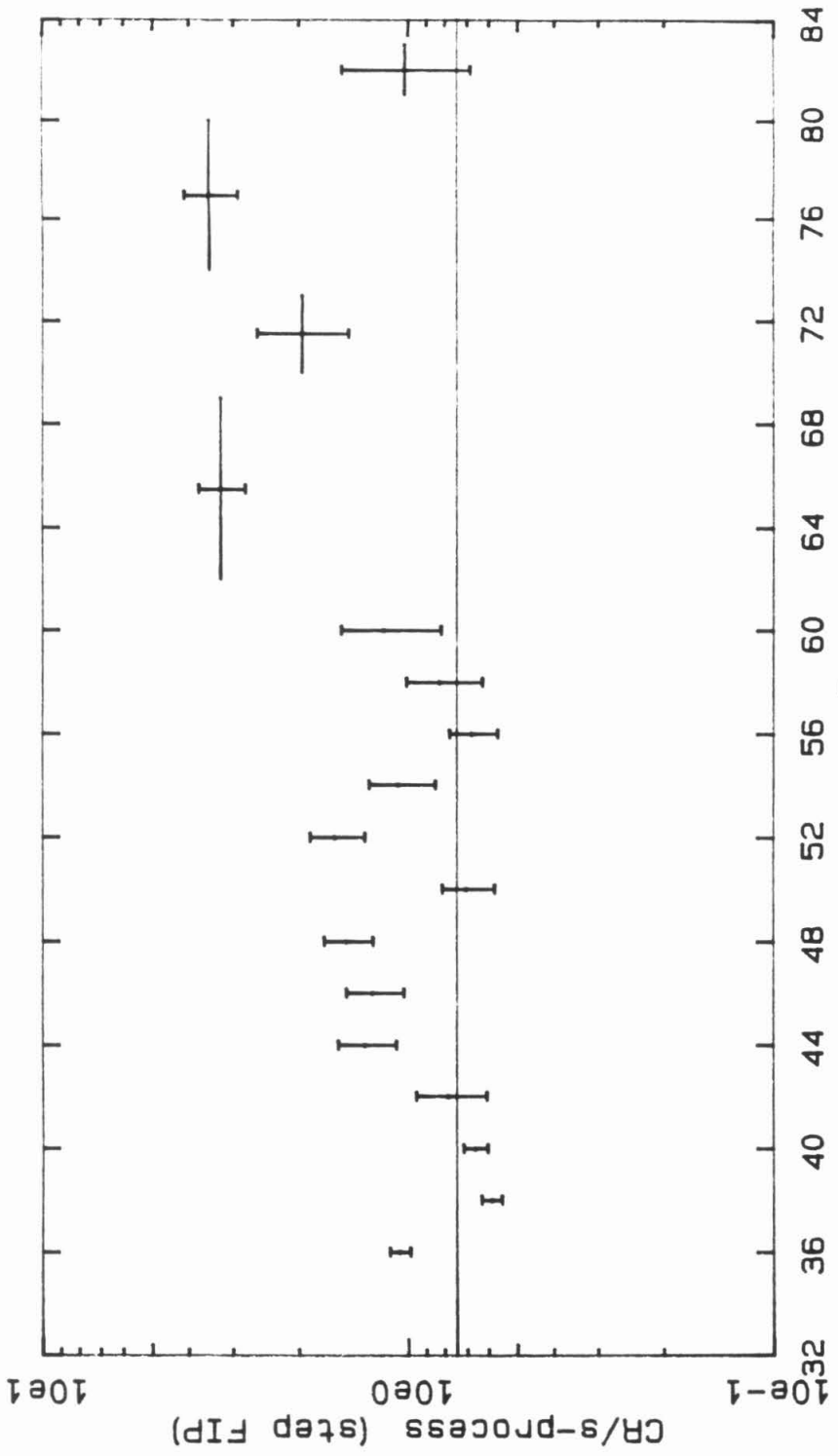

Figure 4.8 The ratios of the group abundances of table 4.3 to those predicted by a propagation model using a pure s-process source and the step function FIP fractionation of (1.2). The horizontal line represents the best fit to the overall normalization relative to iron.

of 0.737. Thus we conclude that if the cosmic ray source is dominated by s-process material, then it is less likely that there is a FIP fractionation of the ultraheavy elements. This conclusion is consistent with that of Binns et al. (1983b), although they used the exponential FIP dependence given in (4.9), rather than the sloping step function used here.

4.2.3. Comparison With an r-Process Source

In this section we compare the observed abundances to those obtained by propagating the solar system r-process, again as given in Binns et al. (1985). These values were obtained by subtracting the s-process abundances from the solar system composition, ignoring the rare p-process nuclei in doing so. Figure 4.9 shows the comparison between the cosmic ray observations and these propagated abundances, again with the r-process to iron normalization fixed at the solar system value. The horizontal line indicates the best fit normalization, which occurs if the r-process is suppressed by a factor 0.433 relative to the solar system. The fit is very poor, with the value of Q^2 being 433.1. This high value is mainly due to the large scatter of the points from Z = 36 to 40.

Figure 4.10 shows the comparison if the source is fractionated by the step function FIP dependence used earlier. With r-process now enhanced by a best fit factor of 1.034 relative to the solar system, the value of Q^2 improves to 167.4, which is still not as good as that obtained for the s-process, with or without a FIP fractionation. It is interesting, however, that the abundances of the Pt group and both of its secondary groups agree very well with the normalization shown. Since the primary nuclei in these groups are mainly produced in the r-process, there does appear to be a modest enhancement of r-process material in the source in this charge range, compared to the solar system.

It is clear that the ultraheavy cosmic ray source material is not dominated by r-process material, as shown by the large overabundances of the primary nuclei $_{38}$Sr, $_{40}$Zr, and $_{56}$Ba in Figures 4.9 and 4.10. These nuclei occur at or close to magic neutron numbers and are thus produced in large amounts

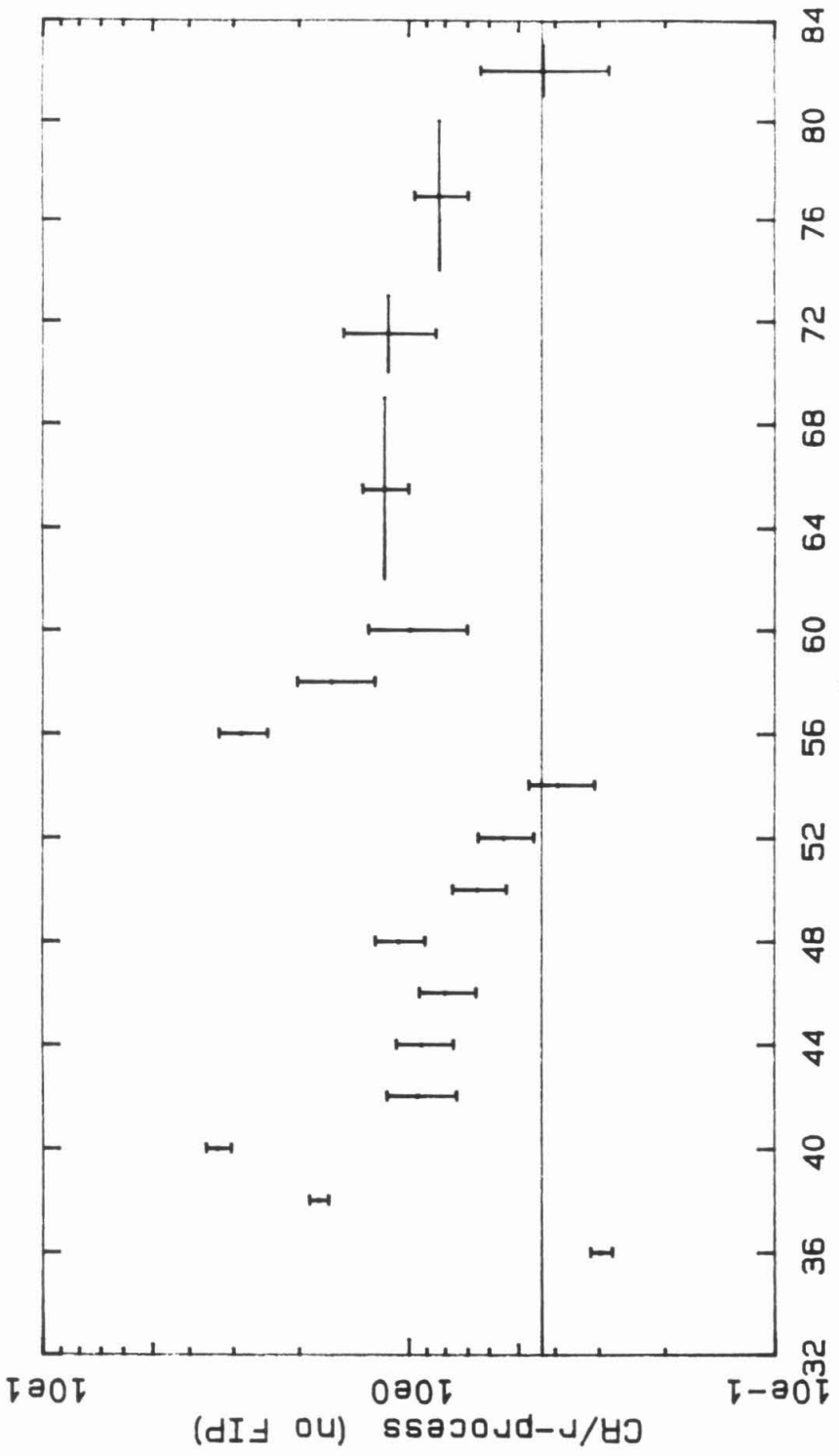

Figure 4.9 The ratios of the group abundances of table 4.3 to those predicted by a propagation model using a pure r-process source and no FIP fractionation. The horizontal line represents the best fit to the iron normalization.

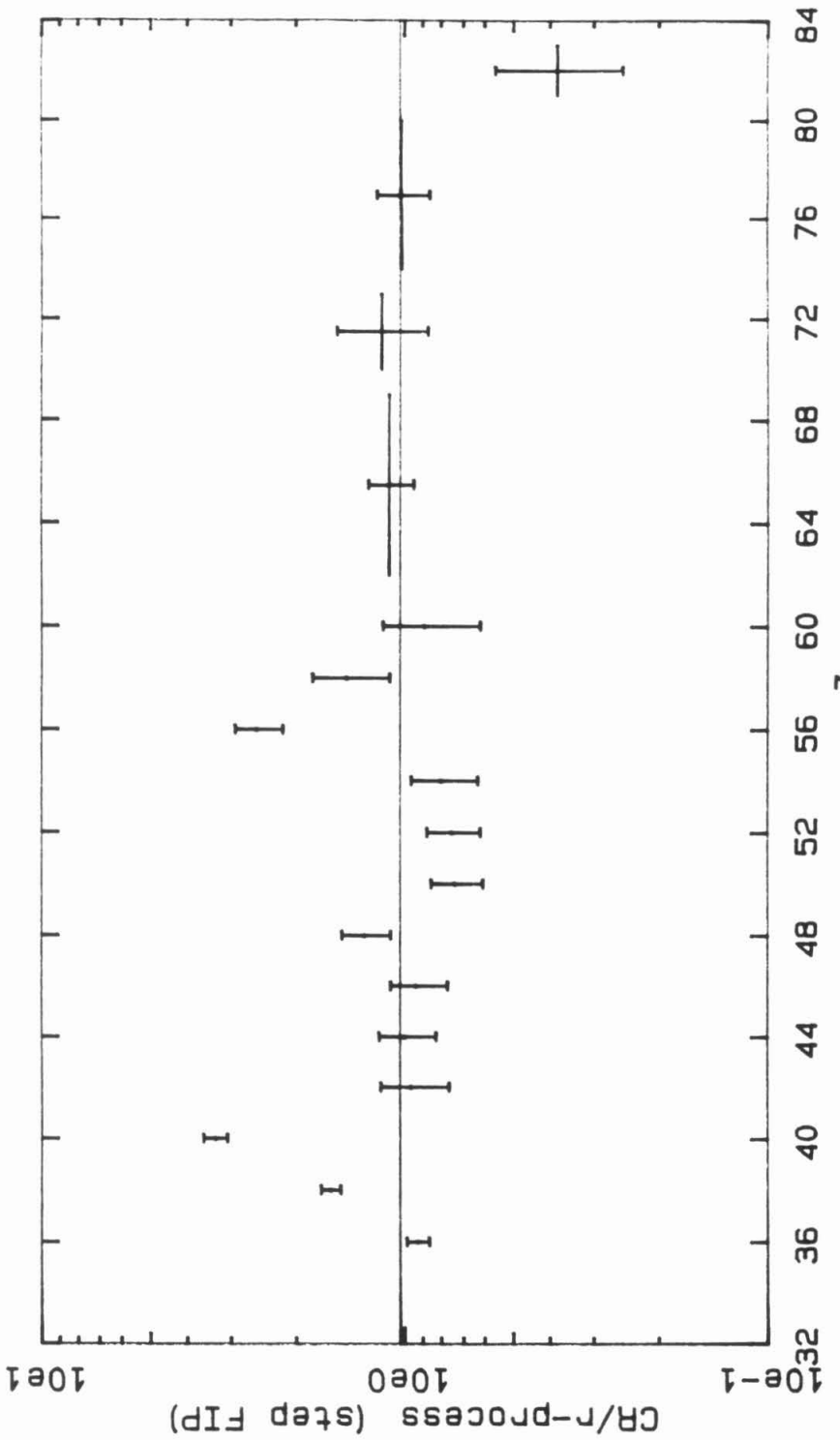

Figure 4.10 The ratios of the group abundances of table 4.3 to those predicted by a propagation model using a pure r-process source, with the step function FIP fractionation given in (1.2). The horizontal line represents the best fit to the iron normalization.

in the s-process.

4.2.4. Comparisons With Mixtures of r- and s-Process Material

In this section, we compare the observed cosmic ray composition with that of linear combinations of propagated r- and s-process sources, in a manner similar to that of Krombel (1983). Such comparisons are permissible because the propagation calculations consist of matrix multiplications, which are inherently linear, and hence a linear combination of the propagation results is equivalent to a linear combination of the sources. Strictly speaking these propagations should be done on an isotope by isotope basis, especially since the r- and s-processes often produce different isotopes of the same element. However, the uncertainty resulting from propagating by elements is thought to be ~5% (Krombel 1983), and thus not important for Z>40.

Following Krombel, we take the linear combination of the r- and s-process abundances:

$$X_i(f) = 2[fS_i + (1-f)R_i] \qquad (4.12)$$

where X is a particular abundance distribution, R and S are the propagated solar system r- and s-process compositions and the mixing parameter f takes values between 0 and 1. If f = 0.5 then X has the same composition as the solar system, including the correct normalization to iron. In this section we will independently normalize each X to obtain the best fit to the data, and thus assume that the r- and s-process contributions to the cosmic ray source are independent of the iron contribution. The quantity

$$\eta = \frac{1-f}{f} \qquad (4.13)$$

gives the ratio of r-process material to s-process material in the source relative to that in the solar system and thus provides a measure of the r-process enhancement; a value of η greater than one indicates that the cosmic rays are enhanced in r-process material, while a value less than one indicates a depletion of r-process material, relative to the solar system.

Figure 4.11 shows the value of Q^2 as a function of f, in the case where there is no FIP fractionation. The minimum value of Q^2 occurs at f = 0.916, implying that the best fit is to a source composed almost entirely of s-process material. The value of Q^2 at the minimum is 80.02, which is approximately twice as large as the value obtained using a solar system source composition and FIP fractionation. If we assume that Q^2 is distributed as χ^2, then the limits of a 68.3% confidence interval for f are given by $Q^2 = Q^2_{min} + 1$. The limits on f obtained in this manner are 0.884 and 0.947; substitution in (4.11) yields

$$\eta(\text{noFIP}) = 0.092^{0.039}_{-0.036}$$

At the best fit value of f, the best overall normalization requires that the abundances of the ultraheavy nuclei be reduced by a factor of 0.844 relative to iron. This normalization is shown as the straight line in Figure 4.12, which plots the ratio of the observed abundances to the propagated source. Inspection of Figure 4.12 confirms that the model does not fit the data very well, with a systematic deviation in the 36-44 region due to not allowing a FIP dependence, and with the Pt group overabundant by a factor of ~2.5 relative to the best fit normalization.

Figure 4.13 shows the variation of Q^2 with f in the case where the step function FIP fractionation is used. The best fit occurs at a value of f of 0.451, implying a small excess of r-process material relative to the solar system. The lowest value of Q^2 is 39.69, somewhat better than the best value obtained with a solar system source. The probability of χ^2 being this high or higher for 16 degrees of freedom is still only 1.0×10^{-3}. The 68.3% confidence limits on f are 0.405 and 0.499, implying that

$$\eta(\text{stepFIP}) = 1.22^{+0.25}_{-0.21}$$

Thus the solar system mix of r- and s-process is only excluded at the 15.9% level. If the uncertainties in the source abundances and propagation were included in this calculation, the observed cosmic ray abundances would be expected to be even more consistent with a solar system mixture of r- and s-process material. The comparison with the data with this propagation is

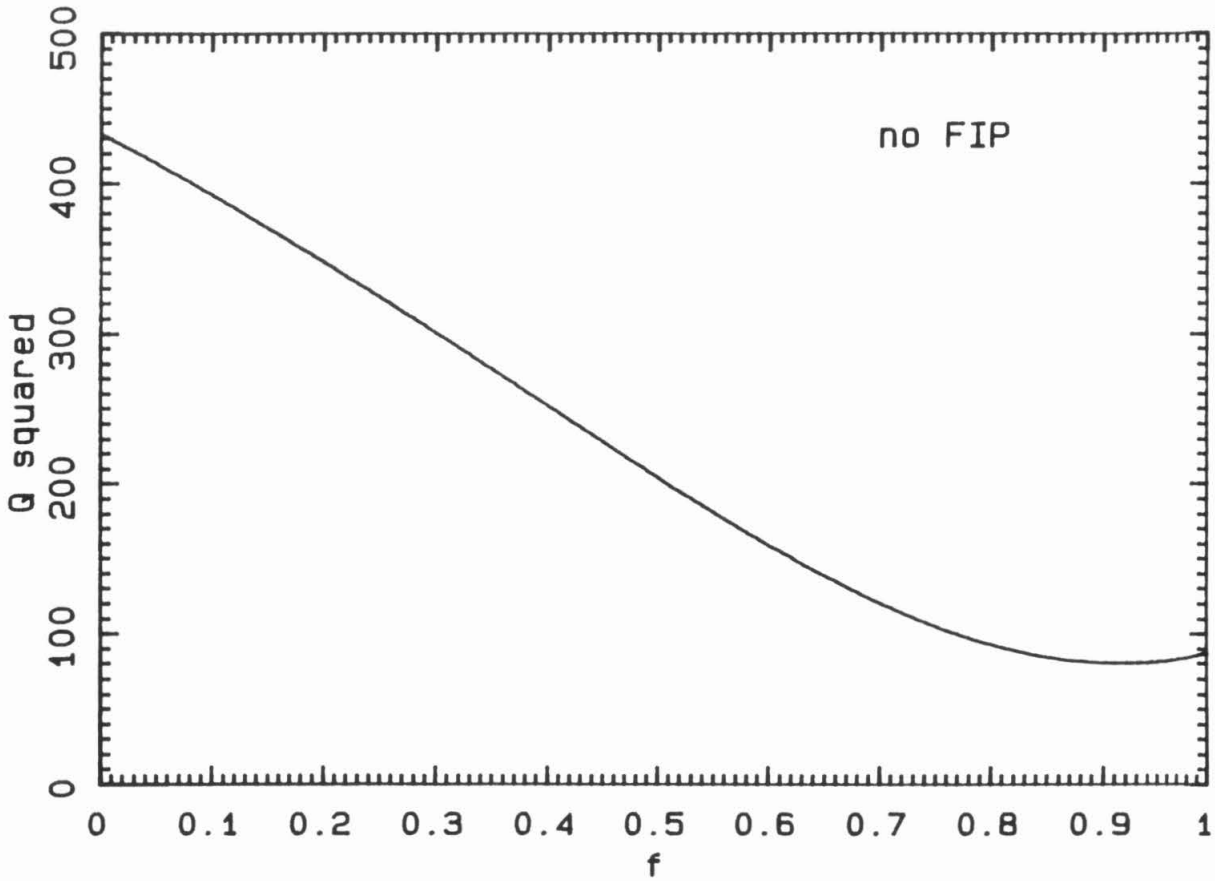

Figure 4.11 The value of Q^2, as defined in the text, as a function of the mixing parameter f. A value of f of 0 corresponds to a pure r-process source, a value of 1 corresponds to a pure s-process source, and f=0.5 corresponds to the solar system source composition. This example is with no FIP fractionation.

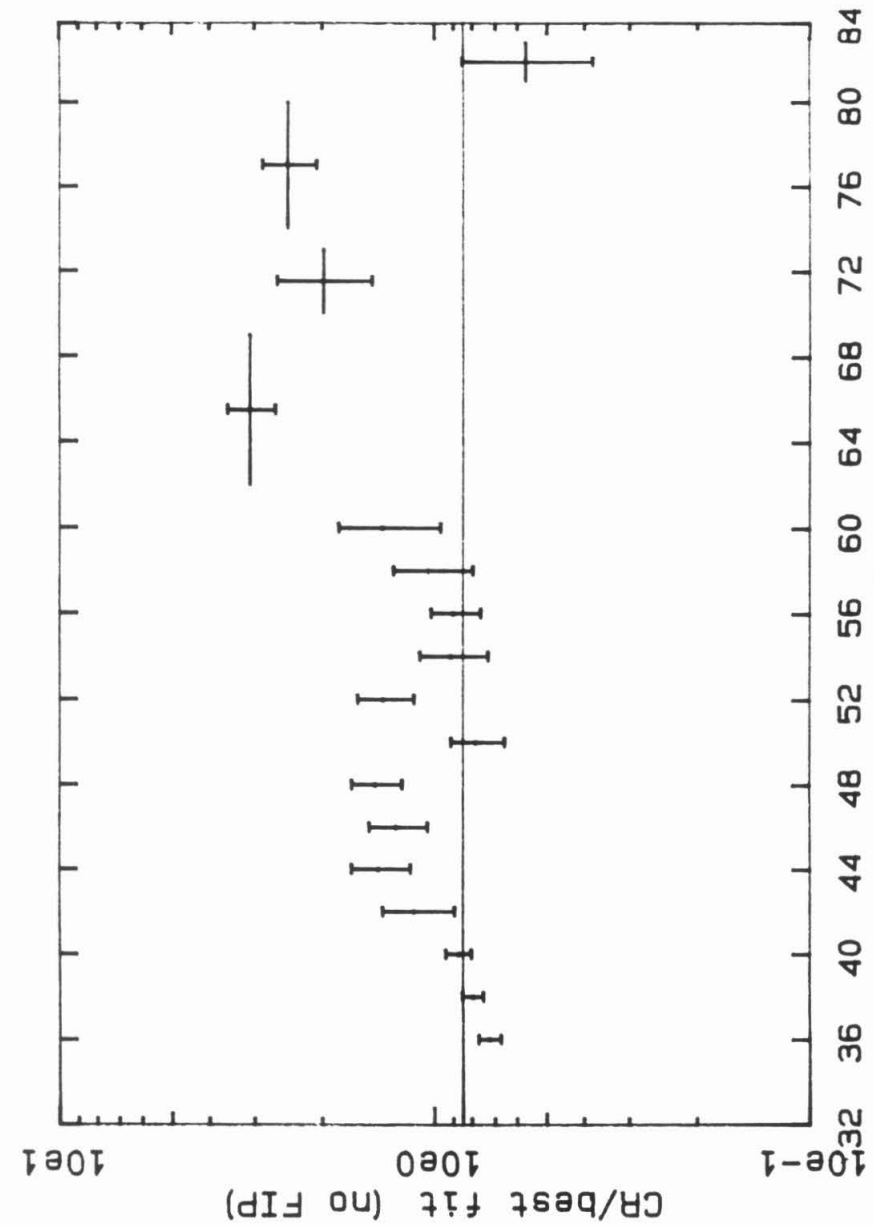

Figure 4.12 The ratios of the group abundances of Table 4.3 to those predicted by the best fit r- and s-process mixture, in the case of no FIP fractionation. This mixture corresponds to f = 0.916.

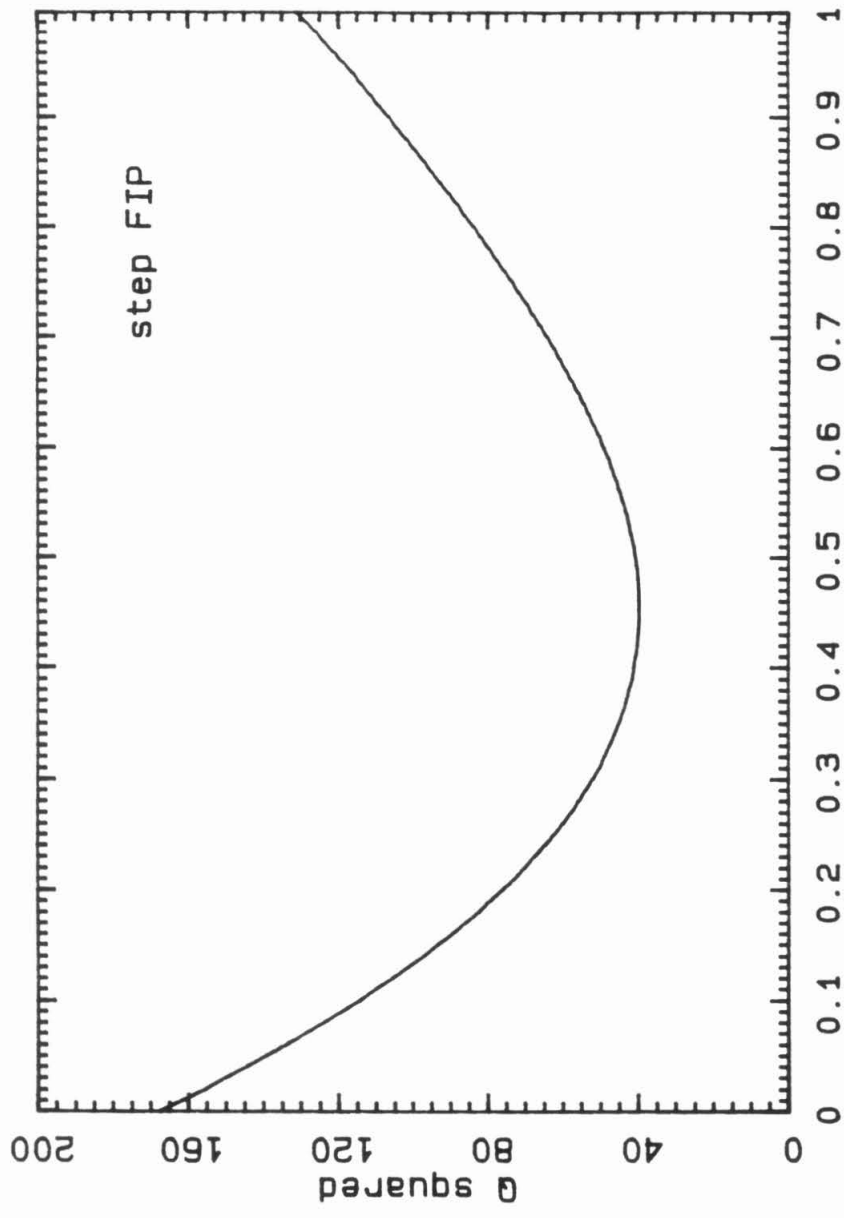

Figure 4.13 The value of Q^2, in the case where the step function FIP fractionation of (1.2) has been applied. Note that the vertical scale is smaller than that of Figure 4.11.

shown in Figure 4.14, which also shows the best fit normalization at 0.980. As expected, this plot is very similar to that of Figure 4.6.

4.3. Conclusions

In this section we interpret the observations within the framework of the standard model of cosmic ray origin and propagation, as outlined in Chapter 1.

4.3.1. The Abundances of Primary Elements

The observed abundances of those elements which are mostly primary show that the cosmic ray source composition is quite similar to that of the solar system, provided that there is a source fractionation based on first ionization potential. This similarity is maintained between elements widely spaced in charge, and also between the ultraheavy elements and iron. The step function FIP fractionation of (1.2) is in better agreement with the observations than the exponential FIP dependence of (4.11).

The cosmic ray source composition is inconsistent with a source whose composition is dominated by either r- or s-process material, regardless of whether a FIP fractionation occurs at the source. A small enhancement of r-process material, relative to the solar system, is the most likely interpretation of the data using current propagation models.

The abundance of $_{34}$Se is lower than that predicted, by a factor of order 0.75 (Figure 4.6), and it is thus possible that the cosmic ray source is depleted in this element. Because selenium can be synthesized in the helium burning process, it was not included in the r- and s-process decompositions.

The abundance of the platinum group is greater than that expected, by a factor of order 1.6. Such an effect would suggest an r-process contribution which increases with charge, relative to the solar system r-process. The abundance of the lead group is lower than that predicted by any model which explains the lower Z data. Because these elements are quite sensitive to cross section uncertainties, it is possible that future propagation calculations will resolve the discrepancy.

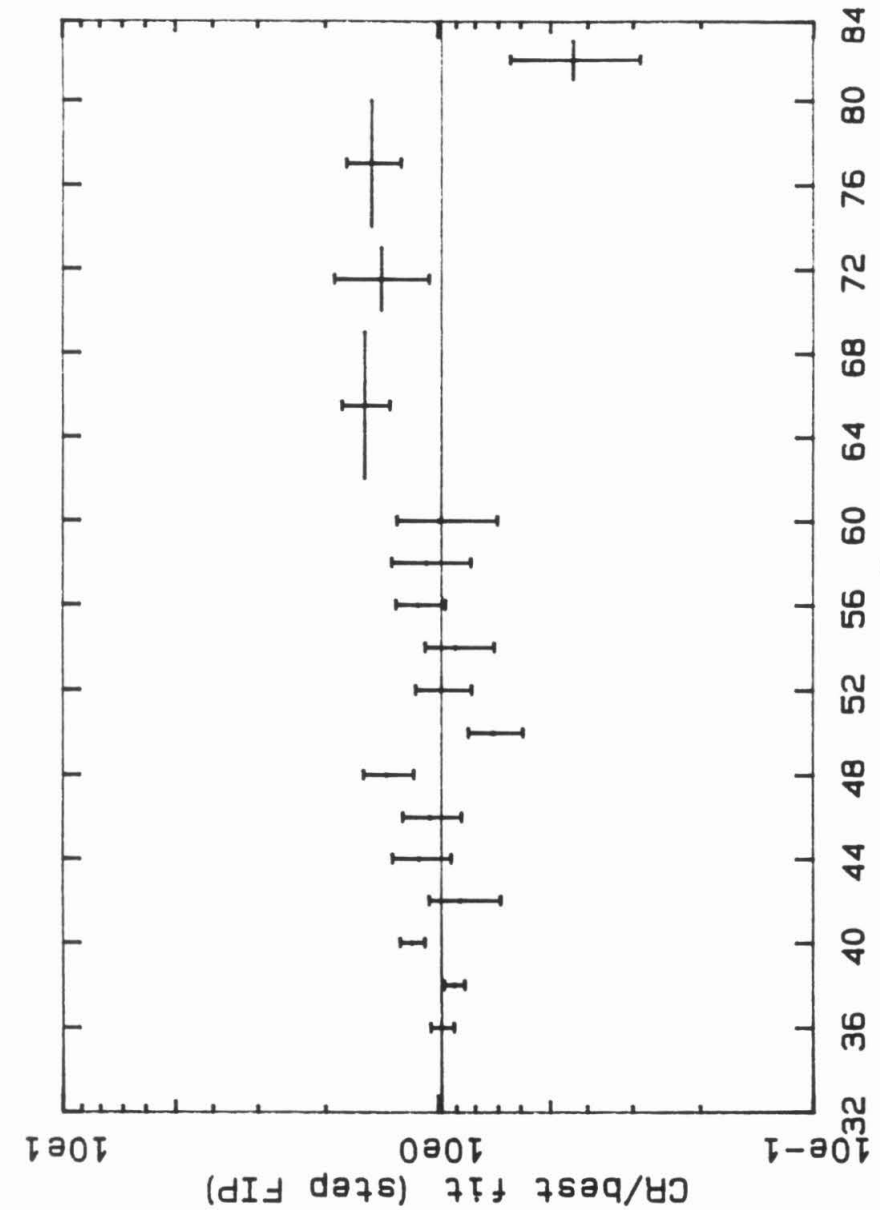

Figure 4.14 The ratios of the group abundances of Table 4.3 to those predicted by a propagation model using the best fit r- and s-process mixture, in the case of a step function FIP fractionation. This plot is quite similar to that of Figure 4.6, which uses a solar system composition.

4.3.2. The Abundances of Secondary Elements

The abundances of the secondary elements are in good agreement with the predictions of the leaky box model using the pathlength distribution which best explains the observations at lower Z. The abundance of $_{50}$Sn is a factor ~0.7 lower than the predicted value, while that of $_{48}$Cd is higher by a factor ~1.4. These discrepancies may be resolved by future improvements in the propagation models.

4.3.3. Energy Spectra

The spectra of the even elements from $_{38}$Sr to $_{60}$Nd inclusive show markedly fewer particles in the energy range 1.5-3 GeV/amu, relative to iron. The evidence for this is the sharp peaks in the histograms of Figures 3.12 and 3.13, especially when compared with the distributions of Z_C expected from the iron spectrum. These peaks were quite unexpected and were not predicted by the propagation models used here. These models ignore ionization energy losses in the interstellar medium. Energy loss can be quite large at modest energies (see Section 1.2.5), and must be included in the propagation models before any conclusions can be drawn regarding the primary spectra. There is no evidence that the spectra of the primary elements in the Pt-Pb group are different to that of iron, within the limited statistics available.

Secondary elements have spectra which fall more rapidly with energy than those of the primary elements, as do the secondary spectra at lower charges. For Z = 38-60 the evidence for softer spectra is the correlation between the peak position and the primary fraction, as shown in Figure 3.15. For the platinum-lead secondaries, the evidence is the rigidity dependent secondary to primary ratio discussed in Section 4.1.1. Such differences are in qualitative agreement with the predictions of the leaky box model with a rigidity dependent pathlength, since particles of lower rigidities traverse more material on the average, and thus have a greater chance of fragmenting before escape. The spectra of secondary elements may also be affected by energy dependent fragmentation cross sections, and it appears that such an

explanation is required to explain the energy dependence of the secondary to primary ratio for Z>60.

4.4. Requirements for Future Experiments

Future experiments to measure the abundances of ultraheavy elements must have a number of features in order to resolve the questions arising from the HNE data analysis. Some of these features are outlined here.

1) Better resolution. Although the ~0.34 charge units resolution achieved by the HNE is adequate to resolve most adjacent elements, a lower figure would enable more reliable abundance measurements at the precipices in the abundance distribution. It would also enable the measurement of the abundances of some odd elements, such as $_{37}$Rb, which is expected to have a large source component, and which is produced almost entirely in the r-process. The use of homogeneous materials is necessary in order to achieve high resolution in detectors of ultraheavy nuclei.

2) Better statistics. Because of the rarity of ultraheavy elements, future experiments must have either a large geometry factor or else be sufficiently reliable that a long exposure time is achieved. If there were 100 times as many particles available, the statistical limits on the abundances would enable the detection of subtle details in the source composition. When combined with better resolution, an increase of this magnitude would enable most of the odd element abundances to be measured, and would also enable a much more precise measurement of the Pt/Pb ratio. Although not discussed in this thesis, the actinide abundance is of particular interest as it provides a measure of the contribution of freshly synthesized r-process material to the cosmic ray source. The HNE discovered only one actinide candidate in ~600 days of data, which was insufficient to distinguish between freshly synthesized and aged r-process material.

3) Energy Measurement. The results presented in this thesis suggest that the energy spectra of the ultraheavy elements differ from the iron spectrum, especially in the Z = 38-60 region. In order to study the spectra, the particle energies must be measured with reasonable accuracy.

4) Direction Sensing. The Heavy Nuclei Experiment was unable to determine the sense of a particle's trajectory. This made the geomagnetic cutoff less useful for the measurement of rigidity spectra than it might otherwise have been.

5) Isotopes...

REFERENCES

Ahlen, S.P., Cartwright, B.G., and Tarlé, G. 1976, "Near Threshold Response of a Wave-shifted Cherenkov Radiator to Heavy Ions", *Nucl. Inst. Meth.*, **136,** 235.

Ahlen, S.P. 1980, "Theoretical and Experimental Aspects of the Energy Loss of Relativistic Heavily Ionizing Particles", *Rev. Mod. Phys*, **52** 121.

Ahlen, S.P. 1982, "Calculation of the Relativistic Bloch Correction to Stopping Power", *Phys. Rev.*, **A 25** ,1856.

Ahlen, S.P. and Tarlé, G. 1983, "Observation of large Deviations from the Bethe-Bloch Formula for Relativistic Uranium Ions", *Phys. Rev. Lett.*, **50,** 1110.

Anders, E. and Ebihara, M. 1982, "Solar System Abundances of the Elements", *Geochim. Cosmochim. Acta*, **46,** 2363.

Baker, S. and Cousins, R.D. 1984, "Clarification of the Use of Chi-Square and Likelihood Functions in Fits to Histograms", *Nucl. Inst. Meth. Phys. Res.*, **221,** 437-442.

Barkas, W.H. and Berger, M.J. 1964, "Tables of Energy Losses and Ranges of Heavy Charged Particles", N.A.S.A. SP-3013.

Binns, W.R., Israel, M.H., Klarmann, J., Scarlett, W.R., Stone, E.C., and Waddington, C.J. 1981, "The UH-Nuclei Cosmic Ray Detector on the Third High Energy Astronomy Observatory", *Nucl. Inst. Meth.*, **185,** 415.

Binns, W.R., Fickle, R.K., Garrard, T.L., Israel, M.H., Klarmann, J., Stone, E.C., and Waddington, C.J. 1982, "The Abundances of The Actinides in the Cosmic Radiation as Measured on HEAO 3", *Ap. J.*, **261,** L117.

Binns, W.R., Grossman, D.P., Israel, M.H., Jones, M.D., Klarmann, J., Garrard, T.L., Stone, E.C., Fickle, R.K., and Waddington, C.J. 1983a, "Cosmic Ray Elemental Abundances for $26 \leq Z \leq 42$ Measured on HEAO-3", *Proc. 18th Int. Cosmic Ray Conf.* (Bangalore), **9,** 106.

Binns, W.R., Fickle, R.K., Garrard, T.L., Israel, M.H., Klarmann, J., Krombel, K.E., Stone, E.C., and Waddington, C.J. 1983b, "Cosmic Ray Abundances of Sn, Te, Xe, and Ba Nuclei Measured on HEAO-3", *Ap. J.*, **267,** L93.

Binns, W.R., Fixsen, D.J., Garrard, T.L., Israel, M.H., Klarmann, J., Stone, E.C., and Waddington, C.J. 1984, "Elemental Abundances of Ultraheavy Cosmic Rays", *Adv. Space Res.*, **4,** 25-34.

Binns, W.R., Brewster, N.R., Fixsen, D.J., Garrard, T.L., Israel, M.H., Klarmann, J., Newport, B.J., Stone, E.C., and Waddington, C.J. 1985, "Lead, Platinum and Other Heavy Elements in the Primary Cosmic Radiation -- HEAO-3 Results", *Ap. J.*, **297,** 111.

Bloch, F. 1933, "Zur Bremsung rasch bewegter Teilchen beim Durchgang durch Materie", *Ann. Phys.* (Leipzig), **16,** 285.

Breneman, H. and Stone, E.C. 1985, "Precision Measurements of Solar Energetic Particle Composition", *Proc. 19th Intl. Cosmic Ray Conf.* (La Jolla), **4,** 213.

Brewster, N.R., Freier, P.S., and Waddington, C.J. 1983, "The Propagation of Ultraheavy Cosmic Ray Nuclei", *Ap. J.* **264,** 324.

Brewster, N.R. 1984, "The Propagation of Ultraheavy Cosmic Rays", Ph.D. Thesis, University of Minnesota.

Brewster, N.R., Freier, P.S., and Waddington, C.J. 1985, "The Propagation of Ultraheavy Cosmic Ray Nuclei Revisited", *Ap. J.*, **294,** 419.

Burbidge, E.M., Burbidge, G.R., Fowler, W.A., and Hoyle, F. 1957, "Synthesis of the Elements in Stars", *Rev. Mod. Phys.*, **29**, 547.

Clayton, D.D. 1968, "Principles of Stellar Evolution and Nucleosynthesis", McGraw-Hill, New York.

Cowsik, R., Pal, Yash, Tandon, S.N., and Verma, R.P. 1967, "Steady State of Cosmic Ray Nuclei - Their Spectral Shape and Pathlength at Low Energies", *Phys. Rev.*, **158**, 1238.

Eadie, W.T, Drijard, D., James, F.E., Roos, M., and Sadoulet, B. 1971, "Statistical Methods of Experimental Physics", North Holland, Amsterdam.

Engelmann, J.J., Goret, P., Juliusson, E., Koch-Miramond, L., Masse, P., Soutoul, A., Byrnak, B., Lund, N., Peters, B., Rasmussen, I.L., Rotenberg, M., and Westergaard, N.J. 1983, "Elemental Composition of Cosmic Rays From Be to Ni as Measured by the French-Danish Instrument on HEAO-3", *Proc. 18th Int. Cosmic Ray Conf. (Bangalore)*, **2**, 17.

Epstein, J.W., Fernandez, J.I., Israel, M.H., Klarmann, J., and Mewaldt, R.A. 1971, "Large Area Pulse Ionization Chamber for Measurement of Extremely Heavy Cosmic Rays", *Nucl. Inst. Meth.*, **95**, 77.

Fermi, E. 1940, "Nuclear Physics", The University of Chicago Press.

Fleischer , R.L., Price, P.B., Walker, R.M., Maurette, M., and Morgan, G. 1967, *J. Geophys. Res.*, **72**, 355.

Fowler, P.H., Masheder, M.R.W., Moses, R.T., Walker, R.N.F., Worley, A., and Gay, A.M. 1985a, "Ariel VI Measurements of Ultra-heavy Cosmic Ray Fluxes in the Region $34 \leq Z \leq 48$", *Proc. 19th Intl. Cosmic Ray Conf.* (La Jolla), **2**, 115.

Fowler, P.H., Masheder, M.R.W., Moses, R.T., Walker, R.N.F., Worley, A., and Gay, A.M. 1985b, "Ariel VI Measurements of Ultra-heavy Cosmic Ray Fluxes in the Region Z≥48", *Proc. 19th Intl. Cosmic Ray Conf.* (La Jolla), **2,** 119.

Garrard, T.L. 1979a, "HNE Library Generator", Space Radiation Laboratory Technical Report 78-3.

Garrard, T.L. 1979b, "Stoermer Cutoff Calculation, Cutoff Algorithm", HEAO-C3 Internal Report TLG-2.

Garrard, T.L. 1982, "Parameters for Scaling Energy Loss", HEAO-C3 Internal Report TLG-17.

Garrard, T.L. 1983, "New 'Gold' and 'Cobalt' Programs", HEAO-C3 Internal Report TLG-22.

Hess 1912, *Physik. Zeitschr.*, **13,** 1804.

Jackson, J.D. and McCarthy, R.L. 1972, "Z^3 Corrections to Energy Loss and Range", *Phys. Rev.*, **B 6,** 4131.

Jones, M.D. 1983, "Ion Chamber Cross Calibration", HEAO-C3 Internal Report MDJ-10.

Jones, M.D. 1985, "Abundances of Heavy Cosmic Rays at Energies up to 1000 GeV/amu", Ph.D. Thesis, Washington University in St. Louis.

Jones, M.D., Klarmann, J., Stone, E.C., Waddington, C.J., Binns, W.R., Garrard, T.L., and Israel, M.H. 1985, "Energy Spectra of Elements With 18≤Z≤28 Between 10 and 300 GeV/amu", *Proc. 19th Int. Cosmic Ray Conf.* (La Jolla), **2,** 28.

Kaufman, S.B. and Steinberg, E.P. 1980, "Cross-section Measurements of

Nuclides Formed by the Reaction of 0.20 - 6.0 GeV Protons with ^{197}Au", *Phys. Rev.*, **C 22,** 167.

Kertzman, M.P., Klarmann, J., Newport, B.J., Stone, E.C., Waddington, C.J., Binns, W.R., Garrard, T.L., and Israel, M.H. 1985, "Interactions of Haevy Nuclei, Kr, Xe and Ho in Light Targets", *Proc. 19th Intl. Cosmic Ray Conf.* (La Jolla), **3,** 95.

Klarmann, J., Binns, W.R., Israel, M.H., Margolis, S.H., Garrard, T.L., Stone, E.C., Brewster, N.R., Fixsen, D.J., Waddington, C.J. 1983, "Abundances of 'Secondary' Elements Among the Ultraheavy Cosmic Rays - Results From HEAO-3", *Proc. 18th Intl. Cosmic Ray Conf.* (Bangalore), **9,** 279.

Klarmann, J., Margolis, S.H., Stone, E.C., Waddington, C.J., Binns, W.R., Garrard, T.L., Israel, M.H., and Kertzman, M.P. 1985, *Proc. 19th Intl. Cosmic Ray Conf.* (La Jolla), **2,** 127

Krombel, K.E. 1980, "Charge Estimation and Energy Loss", HEAO-C3 Internal Report KK-03.

Krombel, K.E. 1981, "Charge Estimate Update", HEAO-C3 Internal Report KK-05.

Krombel, K.E. 1983, "The Relative Abundances of Sn, Te, Xe, Ba, and Ce in the Cosmic Radiation", Ph.D. thesis, California Institute of Technology.

Letaw, J.R., Silberberg, R., and Tsao, C.H. 1984, "On the Abundances of Ultraheavy Cosmic Rays", *Ap. J.*, **279,** 144.

Letaw, J.R., Silberberg, R., and Tsao, C.H. 1985, "Implications of Cross Section Errors for Cosmic Ray Propagation", *Proc. 19th Intl. Cosmic Ray Conf.* (La Jolla), **3,** 46.

Lezniak, J.A. 1976, "Average Added Component of Cherenkov Radiation Due to

Knock-on Electrons", *Nucl. Inst. Meth.*, **136,** 299.

Olevitch, M.A. 1985, "Transmission Functions for cutoff >0, >5, and >8 GV Using the Library Tapes", HEAO-C3 Internal Report MAO-9.

Ormes, J.F. and Protheroe, R.J. 1983, "Implications of HEAO 3 Data for the Acceleration and Propagation of Galactic Cosmic Rays", *Ap. J.*, **272,** 756.

Pierce, T.E. and Blann, M. 1968, "Stopping Powers and Ranges of 5-90 MeV ^{32}S, ^{35}Cl, ^{79}Br, and ^{127}I in H_2, He, N_2, Ar, and Kr", *Phys. Rev.*, **173,** 390.

Salamon, M.H., Ahlen, S.P., and Tarlé, G. 1980, "Experimental Limits on Deviations from Z^2 Dependence of Čerenkov Radiation by Heavy Ions", *Phys. Rev.*, **A 21,** 1506.

Schramm, D.N. 1982, "The R-process and Nucleocosmochronology", *Essays in Nuclear Astrophysics* (ed. Barnes, C.A., Clayton, D.D., and Schramm, D.N.), 325, Cambridge University Press.

Sharpe, J. 1964, "Nuclear Radiation Detectors", Wiley, New York.

Silberberg, R., and Tsao, C.H. 1973a, "Partial Cross Sections in High Energy Nuclaer Reactions, and Astrophysical Applications. I. Targets With Z≤28", *Ap. J. Supp.*, **25,** 315.

Silberberg, R. and Tsao, C.H. 1973b, "Partial Cross SEctions in High Energy Nuclear Reactions, and Astrophysical Applications. II. Targets Heavier than Nickel", *Ap. J. Supp.*, **25,** 335.

Simpson, J.A. 1983, "Elemental and Isotopic Composition of the Galactic Cosmic Rays", *Ann. Rev. Nucl. Part. Sci.* **33,** 323.

Stone, E.C., Garrard, T.L., Krombel, K.E., Binns, W.R., Israel, M.H., Klarmann, J., Brewster, N.R., Fickle, R.K., and Waddington, C.J. 1983, "Cosmic Ray Abundances of the Even Charge Elements From $_{50}$Sn to $_{58}$Ce Measured on HEAO-3", *Proc. 18th Intl. Cosmic Ray Conf.* (Bangalore), **9,** 115.

Truran, J.W. and Iben, I., Jr. 1977, "On s-Process Nucleosynthesis in Thermally Pulsing Stars", *Ap. J.*, **216,** 797.

Tsao, C.H., and Silberberg, R. 1979, "Improved Semiempirical Estimates of Cross Sections", *Proc. 16th Intl. Cosmic Ray Conf.* (Kyoto), **2,** 202.

Waddington C.J., Freier P.S. and Fixsen D.J. 1983, "Stopping of 200-GeV Gold Nuclei in Nuclear Emulsions", *Phys. Rev.* **A28** ,464.

Waddington, C.J., Fixsen, D.J., and Freier, P.S. 1985, "Stopping Relativistic Xe, Ho, Au, and U Nuclei in Nuclear Emulsions", *Proc. 19th Int. Cosmic Ray Conf.* (La Jolla), **6,** 104.

Westfall, G.D., Wilson, L.W., Lindstrom, P.J., Crawford, H.J., Greiner, D.E., and Heckman, H.H. 1979, "Fragmentation of Relativistic ^{56}Fe", *Phys. Rev.*, **C 19,** 1309.

Wiedenbeck, M.E. and Greiner, D.E. 1980, "A Cosmic Ray Age Based on the Abundance of ^{10}Be", *Ap. J.*, **239,** L139.